

UNIVERSITY OF BELGRADE
FACULTY OF MECHANICAL ENGINEERING



MUSTAFA MAKHZOUM MAHJOUB

**THE EFFECT OF BLENDING HYDROGEN INTO
NATURAL GAS ON COMBUSTION**

DOCTORAL DISSERTATION

BELGRADE, 2018

UNIVERZITET U BEOGRADU
MAŠINSKI FAKULTET



MUSTAFA MAKHZOUM MAHJOUR

UTICAJ UVOĐENJA VODONIKA U PRIRODNI GAS
NA PROCES SAGOREVANJA

DOKTORSKA DISERTACIJA

BEOGRAD, 2018

Supervisor of doctoral dissertation

dr Miroljub Adžić, Full Professor
University of Belgrade, Faculty of Mechanical Engineering

Members of the committee for the defense of the doctoral dissertation

dr Dragoslava Stojiljković, Full Professor
University of Belgrade, Faculty of Mechanical Engineering

dr Vasko Fotev, Full Professor
University of Belgrade, Faculty of Mechanical Engineering

dr Marija Živković, Associate Professor
University of Belgrade, Faculty of Mines and Geology

Dr Aleksandar Milivojević, Assistant Professor
University of Belgrade, Faculty of Mechanical Engineering

Date of defense:

*The thesis is dedicated to all of my parents, wife, children,
brothers and sister whose love, Mustafa, sacrifices and
encouragement is boundless*

ACKNOWLEDGEMENTS

I would like to express my sincere gratitude to my advisor Prof. M. Adžić for his consistent guidance, invaluable support, encouragement and inspiration throughout the work. I thank him for his friendship and all the expertise he has shared with me. I could not have imagined having a superb advisor and mentor for my doctoral study.

I would also record my thanks to all people who helped and supported me in any way in this work and whom I feel grateful.

Finally, and most importantly, my warmest appreciation is reserved for my mother, my wife and my sons for all their love and support that they have provided for years during the whole course of this work.

Author

Belgrade, 2018

TABLE OF CONTENTS

Contents

ACKNOWLEDGEMENTS	i
TABLE OF CONTENTS	ii
ABSTRACT	iv
Nomenclature.....	viii
LIST OF FIGURES	xi
LIST OF TABLES	xv
1 Chapter 1	1
1.1 INTRODUCTION	1
1.1.1 World energy and environmental aspects.....	1
2 Chapter2	6
2.1 Introduction.....	6
2.2 Review of previous work	7
3 CHAPTER 3.....	14
3.1 COMBUSTION MODELLING BY CFD	14
3.1.1 Governing equations of fluid dynamics	14
3.1.2 Differential forms of general Transport Equation	17
3.2 Modeling Turbulence.....	18
3.2.1 Classification turbulent flow model in fluent	18
3.3 Combustion modeling.....	27
3.3.1 Combustion models in Ansys Fluent.....	28
3.3.2 Premixed Combustion Medelling.....	33
3.3.3 Partially Premixed Combustion Modeling	35
3.4 NOx modeling.....	36

CHAPTER 4.....	38
4 COMBUSTOR MODELING AND SIMULATION SETUP	38
4.1 COMBUSTOR AND MIXER DESCRIPTION.....	38
4.2 EXPERIMENTAL DESCRIPTION.....	39
4.3 NUMERICAL SETUP AND BOUNDARY CONDITIONS.....	40
4.4 COMBUSTOR MODELING	41
4.4.1 Mixing chamber meshing	42
4.4.2 Combustion chamber meshing	45
4.4.3 Independency of grid Quality for mixer (grid sensitivity solutions).....	46
4.4.4 Independency of grid Quality for combustion.....	51
Chapter 5	54
5 RESULTS.....	54
5.1 Validation of predicted results with experimental data	54
5.2 Conclusion	89

ABSTRACT

Energy is one of the fundamentals of the economics of all countries. Far the most of world energy is produced by combustion of fossil fuels. It is expected that fossil fuels to supply 80 percent of the energy demand in 2040. Because of their availability, price, excellent burning characteristics, low emission potentials, natural gas and liquefied petroleum gases are expected to be main fuels in the next fifty years. The world energy production will be increasingly based on renewables, mainly on wind, solar, hydro and biofuels. Beside advantages of utilization of renewable energy sources, there are drawbacks, such as intermittent variations in wind and solar energy production. As a consequence, the inclusion of wind and solar energy sources to grid can pose serious problems. A solution that utilizes some kind of energy storage appears to be effective and relatively simple. Among the storage methods, such as batteries, capacitors, hydro and others, production and storage of hydrogen appears to be promising. Hydrogen can be blended with natural gas and LPG gases and used in existing motors, gas turbines and other appliances. Hydrogen can be introduced into existing gas pipelines and underground storage facilities, using existing infrastructure. It has been found that blending up to 10% of hydrogen is safe to be used in existing facilities operating on natural and LP gases. The high flame speed, diffusivity and low emissions capabilities, are advantages when burning hydrogen. A lean premixed combustion method in gas turbines has been successfully introduced during last two decades. The lean premixed swirl combustion of fossil fuels blends with hydrogen is still not fully understood. This thesis has investigated a lean premixed swirl turbulent combustion of a fossil gas fuel-hydrogen mixture in two microturbine combustor configurations: with and without a center body, different swirl numbers and equivalence ratios. This investigation is based on numerical analysis supported by experimental results. The realizable k- ϵ turbulence model, which is a variant of the standard k- ϵ turbulence model was used. The finite rate/eddy dissipation model was used to address the turbulence-chemical reaction. Thermal radiation heat transfer from combustion products to the combustor wall was considered as well. The effects of hydrogen addition on reactions rates, velocity, concentration of species, temperature distribution in combustor, and NO_x emissions for different equivalence ratios, $\Phi = 0.6, 0.7, 0.8$ and 0.9 , and swirl numbers $s = 0, 0.45, 0.73$ and 1.13 are given. The base fuel/hydrogen mixture of 90/10% by volume was

assumed. Combustion characteristics such as the radial temperature, axial temperature, and the gas concentrations of species are affected by the swirl number. The flow structure of the flame field, central recirculation zone and wall recirculation zones for tubular and annular combustors were found to change significantly.

The numerical results and measurements of NO_x emissions are compared. Very good agreements are found for all equivalence ratios and swirl numbers, except for the highest swirl number (1.13). It is found that addition of hydrogen increases the NO_x emission. On the other hand, the increase of swirl number and the decrease of equivalence ratio decrease the NO_x emission.

Keywords: Natural Gas, Hydrogen Blending, Propane, Premixed Combustion, Swirl Burner, CFD, NO_x Emission.

Scientific field: Mechanical Engineering.

Narrow scientific field: Combustion.

UDC number: 662.61:662.767:662.769.2 (04.3)

662.94:536.46:519.6 (043.3)

UTICAJ UVOĐENJA VODONIKA U PRIRODNI GAS NA PROCES SAGOREVANJA

Abstrakt

Energija je jedna od funfamenata ekonomije svake zemlje. U većini sveta energija se proizvodi sagorevanjem fosilnih goriva. Očekuje se da će 80 % svetskih potreba za energijom u 2040 godini dobiti iz fosilnih goriva. Zbog lake dostupnosti, cene, odličnih karakteristika sagorevanja, potencijalno male emisije, očekuje se da prirodni gas i tečni naftni gasovi budu vodeća goriva u sledećih 50 godina. Istovremeno će se povećavati proizvodnja energije iz obnovljivih izvora, prevažno, energija vetra, sunčeva energija, hidro i biogoriva. Kao posledica, uvođenje energije vetra i sunca u energetska mrežu može da dovede do ozbiljnih problema. Rešenje ovog problema, kojim se skladišti energija može da bude efikasno i relativno jednostavno. Među raznim metodama skladištenja energije, kao što su, električne baterije, superkondenzatori, hidro i drugi, proizvodnja i skladištenje vodonika se čini da je obećavajuće rešenje. Vodonik može da se meša sa prirodnim gasom i tečnim naftnim gasovima i da se koristi u postojećim motorima, kotlovima, gasnim turbinama i drugim energetskim uređajima. Vodonik može da se uvodi u postojeći gasovod i skladišti, koristeći postojeću infrastrukturu. Smatra se da su mešavine gasova sa 10%vol vodonika sigurne da budu korišćene u postojećim postrojenjima koja koriste prirodni gas i tečne naftne gasove. Relativno velika brzina prostiranja plamena, karakteristike difuzije i mala emisija su prednosti korišćenja vodonika. Već preko dve decenije se u gasnim turbinama i drugim uređajima koristi siromašna smeša i kinetički plamen kao metoda sagorevanja. Ova disertacija se bavi istraživanjem turbulentnog sagorevanja kinetičkim plamenom siromašne prethodno formirane smeše fosilnog goriva i vodonika u gorioniku sa i bez centralnog tela, pri različitim vihornim brojevima i koeficijentima viška vazduha. Istraživanje prikazano u disertaciji se zasniva na numeričkoj analizi i eksperimentalnim nalazima. Numerička analiza koristi „realizable k- ϵ ” model turbulencije koji je varijanta standardnog k- ϵ modela. Pristup je takođe na ideji konačne brzine disipacije energije turbulencije i hemijskih reakcija. Model obuhvata i prenos toplote zračenjem na zidove gorionika. U tezi su dati rezultati uticaja dodatka vodonika u osnovno gorivo, na brzinu

hemijskih reakcija, raspodelu brzina, koncentraciju reaktanata i produkata sagorevanja i raspodelu temperature u gorioniku, emisiju NO_x , za različite vrednosti koeficijenta viška vazduha, $1/\lambda = 0,6$ 0,7 0,8 i 0,9 i razne vihorne brojeve, $s = 0,$ 0,45 0,73 i 1,13. Razmatrana je mešavina osnovnog goriva i vodonika u odnosu 90/10%vol. Utvrđeno je da na temperatursko i brzinsko polje, raspodelu centralne i bočnih recirkulacionih zona, koncentracije reaktanata i produkata sagorevanja značajno utiču prisustvo vodonika, kao koeficijent viška vazduha, i vihorni broj. Veoma dobro je slaganje vrednosti numeričkih i eksperimentalnih rezultata za sve slučajeve izuzev za najveći vihorni broj. Uvođenjem vodonika povećava se emisija NO_x , a povećanjem vihornog broja i koeficijenta viška vazduha smanjuje se emisija NO_x .

Ključne reči: prirodni gas, uvođenje vodonika, propan, kinetički plamen, vihorni gorionik, numeričke metode, emisija NO_x .

Naučna oblast: Mašinsko inženjerstvo

Uža naučna oblast: Sagorevanje

UDK broj: 662.61:662.767:662.769.2 (04.3)

662.94:536.46:519.6 (043.3)

Nomenclature

A	- empirical constant equal to 4.0, [-]
B	- empirical constant equal to 0.5, [-]
S	- swirl number, [-]
d_h	- swirler hub diameter, [m]
d_0	- swirler diameter, [m]
x	- reference for x-axis,
y	- reference for y-axis,
z	- reference for z-axis,
u	- component of velocity in x direction
v	- component of velocity in y direction
w	- component of velocity in z direction
\vec{V}	- velocity vector
ρ	- density, [kg.m ⁻³]
μ	- viscosity, [kg.m ⁻¹ s ⁻¹]
τ	- shear stress
λ	- bulk viscosity coefficient
k	- thermal conductivity
\dot{q}	- rate of heat energy
e	- internal energy per unit mass
\emptyset	- general variable
S_i	- rate of creation of species i , [kg.m ⁻³ s ⁻¹]
Pr_t	- turbulent Prandtl number
μ_t	- turbulent viscosity
M_t	- turbulent Mach number
$\emptyset_{ij,1}$	- slow pressure-strain term
$\emptyset_{ij,2}$	- rapid pressure-strain term
$\emptyset_{ij,w}$	- wall-reflection term.
\mathcal{K}	- von Karman constant
b_{ij}	- Reynolds-stress anisotropy tensor
J_i	- diffusion flux of species, [kg.m ⁻² s]

L	- center body length, [m]
L/L_0	- normalized center body length, [-]
L_0	- nominal center body length, [m]
$M_{w,i}$	- molecular mass of species i , [kg.mol ⁻¹]
R_i	- net rate of production of species i , [kg.m ⁻³ s ⁻¹]
ν_t	- turbulent viscosity, [kg.m ⁻¹ s ⁻¹]
$\nu'_{i,r}$	- stoichiometric coefficient for reactant i in reaction r , [-]
$\nu''_{i,r}$	- stoichiometric coefficient for product i in reaction r , [-]
Y_i	- mass fraction of species i , [-]
X_i	- mole fraction of species i , [-]
Y_P	- mass fraction of any product species, [-]
Y_R	- mass fraction of a particular reactant, [-]
E'_a	- activation energy, [J.mol ⁻¹]
T	- temperature, [K]
R_u	- universal gas constant(=8.314), [J.mol ⁻¹ K ⁻¹]
\mathcal{D}	- effective diffusion coefficient, [kg.m ⁻³ s ⁻¹]
$D_{i,m}$	- mass diffusion coefficient for species i in the mixture,
$D_{T,i}$	- thermal diffusion coefficient
Sc_t	- turbulent Schmidt number
k_f	- forward rate constant for reaction r .
k_b	- backward rate constant for reaction r .
K_r	- equilibrium constant
$C_{j,r}$	- molar concentration of species j in reaction r
$\eta'_{j,r}$	- rate exponent for reactant species j in reaction r
$\eta''_{j,r}$	- rate exponent for product species j in reaction r
β_r	- activation energy for the reaction (J/kmol)
S_i	- entropy of the i^{th} species.
Sc	- reaction progress source
h_i	- enthalpy of the i^{th} species
ν	- kinematic viscosity
\bar{c}	- mean reaction progress variable

U_t	- turbulent flame speed
U_l	- laminar flame speed
α	- molecular heat transfer coefficient
l_t	- turbulence length scale
τ_t	- turbulence time scale
τ_c	- chemical time scale.
U_{NO}	- source term of NO , [m.s ⁻¹]
t	- time, [s]
ε	- turbulent dissipation rate, [m ² .s ⁻³]
κ	- turbulent kinetic energy per unit mass, [J.kg ⁻¹]
Φ	- equivalence ratio, [-]
Θ	- vane outlet angle, [°]

Subscripts:

i	- species, [-]
P and R	- products and reactants, [-]

LIST OF FIGURES

Figure 1-1 The trend of World energy consumption from 1971 until 2013.....	2
Figure 1-2 The fuel shares in electricity generation in 2013.....	2
Figure 1-3 World CO ₂ emissions evolution from 1971 to 2013 by fuel (Mt of CO ₂).....	4
Figure 4-1 Schematics of mixing section and combustor.....	39
Figure 4-2 Cross section of swirler	39
Figure 4-3 Computational mesh for mixer chamber	44
Figure 4-4 Computational mesh for combustor chamber.....	46
Figure 4-5 Grid sensitivity solutions of the component velocity (u)	48
Figure 4-6 Grid sensitivity solutions of the component velocity (v)	49
Figure 4-7 Grid sensitivity solutions of the component velocity (w)	49
Figure 4-8 Grid sensitivity solutions of the total velocity.....	50
Figure 4-9 Grid sensitivity solutions of the temperature.....	52
Figure 5-1 Experimental and numerical NO _x emissions for tubular combustion as a function of equivalence ratio and (S=0 and S= 0.45).....	54
Figure 5-2 Experimental and numerical NO _x emissions for tubular combustion as a function of equivalence ratio and (S=0.73 and S= 1.13).....	55
Figure 5-3 Experimental and numerical NO _x emissions for annular combustion as a function of equivalence ratio and (S=0 and S= 0.45).....	55
Figure 5-4 Experimental and numerical NO _x emissions for annular combustion as a function of equivalence ratio and (S=0.73 and S= 1.13).....	56
Figure 5-5 Temperature profiles along (x-x) line at $\phi=0.7$, $L/L_0=0$ and various swirl numbers	57
Figure 5-6 Temperature profiles along (x-x) line at $\phi=0.8$, $L/L_0=0$ and various swirl numbers	58
Figure 5-7 Temperature profiles along (x-x) line at $\phi=0.9$, $L/L_0=0$ and various swirl numbers	59
Figure 5-8 Radial temperature profiles at $z=4$ mm, $\phi=0.7$, $L/L_0=0$ and various swirl numbers	60
Figure 5-9 Radial temperature profiles at $z=4$ mm, $\phi=0.8$, $L/L_0=0$ and various swirl numbers	60

Figure 5-10 Radial temperature profiles at $z=4$ mm, $\phi=0.9$, $L/L_0=0$ and various swirl numbers	61
Figure 5-11 Temperature profiles along (x-x) line at $\phi=0.7$, $L/L_0=1$ and various swirl numbers	62
Figure 5-12 Temperature profiles along (x-x) line at $\phi=0.8$, $L/L_0=1$ and various swirl numbers	62
Figure 5-13 Temperature profiles along (x-x) line at $\phi=0.9$, $L/L_0=1$ and various swirl numbers	63
Figure 5-14 Radial temperature profiles at $z=4$ mm, $\phi=0.7$, $L/L_0=1$ and various swirl numbers	64
Figure 5-15 Radial temperature profiles at $z=4$ mm, $\phi=0.8$, $L/L_0=1$ and various swirl numbers	64
Figure 5-16 Radial temperature profiles at $z=4$ mm, $\phi=0.9$, $L/L_0=1$ and various swirl numbers	65
Figure 5-17 Flow structure along the central plane of tubular combustor chamber ($L/L_0=0$) for $\Phi =0.8$, and different swirl numbers for pure propane	66
Figure 5-18 Flow structure along the central plane of combustor chamber for $\Phi =0.8$, and different swirl numbers for pure propane	68
Figure 5-19 Flow structure along the central plane of combustor chamber for $\Phi =0.9$, and different swirl numbers for pure propane	69
Figure 5-20 Temperature distributions along the central plane of combustor chamber at $\Phi =0.8$, $L/L_0=0$ and various swirl numbers (pure propane)	71
Figure 5-21 Variation of average temperature at outlet with the central body ratio at equivalence ratio 0.8.....	72
Figure 5-22 Variation of average temperature at outlet with the central body ratio at equivalence ratio 0.9.....	73
Figure 5-23 Temperature distributions along the central plane for $\Phi =0.8$, and different swirl numbers (left - pure propane, right - 90% C_3H_8 and 10% H_2 vol).....	74
Figure 5-24 Propane mass fraction of mixed propane-hydrogen- air flame along (x-x) line at $\phi=0.7$, $L/L_0=0$ and various swirl numbers.....	75
Figure 5-25 Propane mass fraction of mixed propane-hydrogen- air flame along (x-x) line at $\phi=0.8$, $L/L_0=0$ and various swirl numbers.....	76

Figure 5-26 Propane mass fraction of mixed propane-hydrogen- air flame along (x-x) line at $\phi=0.9$, $L/L_0=0$ and various swirl numbers.....	76
Figure 5-27 Hydrogen mass fraction of mixed propane-hydrogen- air flame along (x-x) line at $\phi=0.7$, $L/L_0 = 0$ and various swirl numbers.....	77
Figure 5-28 Hydrogen mass fraction of mixed propane-hydrogen- air flame along (x-x) line at $\phi=0.8$, $L/L_0 = 0$ and various swirl numbers.....	78
Figure 5-29 Hydrogen mass fraction of mixed propane-hydrogen- air flame along (x-x) line at $\phi=0.9$, $L/L_0 = 0$ and various swirl numbers.....	78
Figure 5-30 Profile of reaction rate of propane along (x-x) line at $\phi=0.8$, $L/L_0=0$ and various swirl number	79
Figure 5-31 Profile of reaction rate of propane along (x-x) line at $\phi=0.8$, $L/L_0=0$ and various swirl number	80
Figure 5-32 Oxygen mass fraction along (x-x) line at $\phi=0.7$, $L/L_0 = 0$ and various swirl numbers	81
Figure 5-33 Oxygen mass fraction along (x-x) line at $\phi=0.8$, $L/L_0 = 0$ and various swirl numbers	81
Figure 5-34 Oxygen mass fraction along (x-x) line at $\phi=0.9$, $L/L_0 = 0$ and various swirl numbers	82
Figure 5-35 H ₂ O mass fraction along (x-x) line at $\phi=0.7$, $L/L_0 = 0$ and various swirl numbers	83
Figure 5-36 H ₂ O mass fraction along (x-x) line at $\phi=0.8$, $L/L_0 = 0$ and various swirl numbers	83
Figure 5-37 H ₂ O mass fraction along (x-x) line at $\phi=0.9$, $L/L_0 = 0$ and various swirl numbers	84
Figure 5-38 CO ₂ mass fraction along radial line at outlet of combustor chamber for $\phi=0.7$, $L/L_0 = 0$ and various swirl numbers.....	85
Figure 5-39 CO ₂ mass fraction along radial line at outlet of combustor chamber for $\phi=0.8$, $L/L_0 = 0$ and various swirl numbers.....	85
Figure 5-40 CO ₂ mass fraction along radial line at outlet of combustor chamber for $\phi=0.9$, $L/L_0 = 0$ and various swirl numbers.....	86
Figure 5-41 Average mass fractions of CO ₂ at outlet for different equivalence ratios and swirl numbers of propane/hydrogen mixture ($L/L_0 = 0$).....	87

Figure 5-42 NO_x emission for different equivalence ratios and swirl numbers of propane and propane/hydrogen mixture. 88

LIST OF TABLES

Table 4-1 Details of mixing chamber computational mesh.....	43
Table 4-2 Details for combustor chamber computational mesh.....	45
Table 4-3 Details of proposal computational mesh for mixer chamber	47
Table 4-4 Details of proposal computational mesh for combustion chamber.....	51

1 Chapter 1

1.1 INTRODUCTION

1.1.1 World energy and environmental aspects.

Energy plays an important role in the economics of all countries. It is the driving engine to development and one of the basic factors to improve the quality of life and economic viability. The policies of the electricity and energy sector aim to optimum utilization of primary energy sources. In 2013, the worldwide energy consumption of the human race was estimated at 13451 million ton oil equivalent (Mtoe) with 81.4% from burning fossil fuels, coal, oil and natural gas. Figure 1-1 represents the trend of world energy consumption from 1971 until 2013[1]. Regarding the electricity generation, Figure 1-2 represents the fuel shares in electricity generation in 2013. It is realized that the main energy contribution in the electrical power generation field is the fossil fuel (coal, oil, and gas) with a total percentage about 67.4%. While the nuclear energy contributes 10.6%, and 5.7% from renewables (Wind, Sun, biomass) hydro power contributes 16.3% from the total electricity generation of 23322 TWh [1]

From the previous statistics, it can be concluded that thermal energy is still the main energy source all over the world and deserves appropriate research.

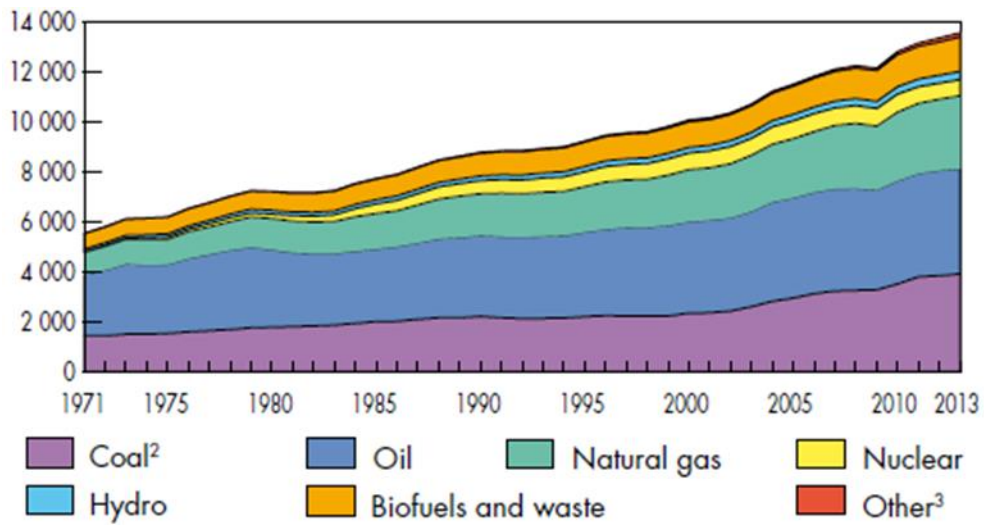


Figure 1-1 The trend of World energy consumption from 1971 until 2013.

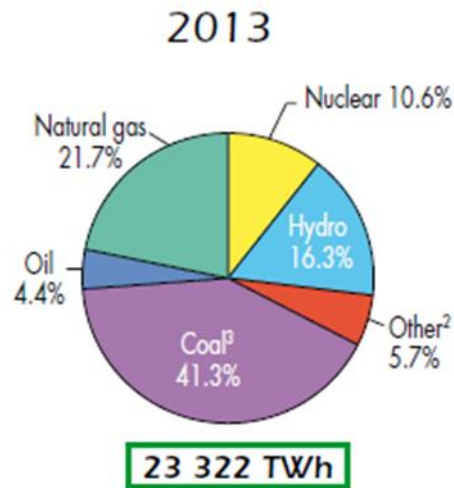


Figure 1-2 The fuel shares in electricity generation in 2013.

The environmental impact of the use of fossil fuels and potential scarcity of supply are the major driving forces behind current energy policies. The environmental problems

associated with fossil fuel consumption are the major problems that most research tackles. Energy production from fossil fuel combustion results in the emission of greenhouse gases, the dominant contributor being CO₂. Public awareness and legislation have led to a policy of reduction of greenhouse gas emissions in most economically well-developed countries [2, 3].

“In recent years, air quality has become a particularly severe problem in many countries. Climate changes has become a global problem of particular concern. Growing concern with exhaust emissions from gas turbines (GT) and internal combustion engines (ICE) has resulted in the implementation of strict emission regulations in many industrial areas such as the United States and Europe. In the meantime, the Kyoto protocol calls for a reduction in greenhouse gas emissions between 2008 and 2012 to the levels that are 5.2% below 1990 levels in 38 industrialized countries. Therefore, how to reduce hazardous emissions and greenhouse gases from engines has now become a research focus. If driven according to the certifying cycle, modern engines with three way catalyst emit very low amounts of hazardous emissions, along with large amounts of water and carbon dioxide (CO₂) emissions,” [4].

According to IEA statistics, the world CO₂ emissions were more than doubled from 1971 till 2013 as shown in Figure 1-3. Emissions were 32190 Mt in 2013. This amount was calculated CO₂ emissions from fuel combustion are based on the IEA energy balances, excluding emissions from non-energy sources [1].

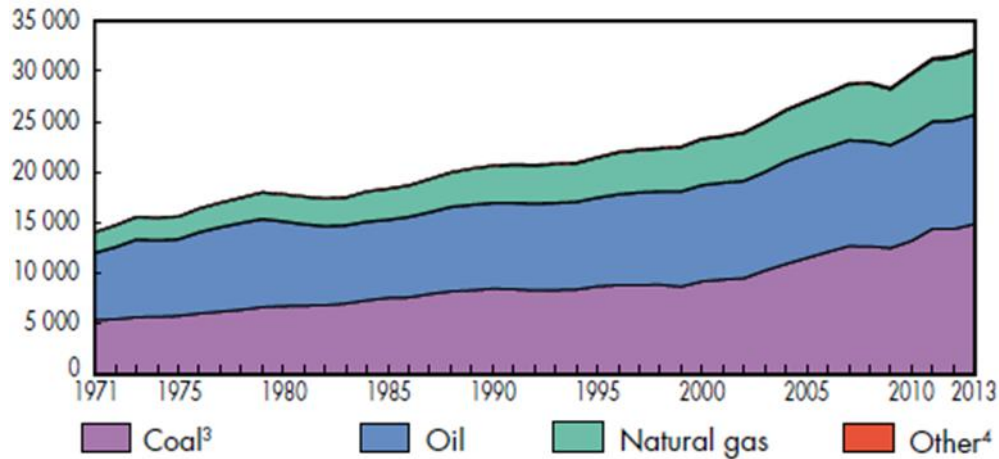


Figure 1-3 World CO₂ emissions evolution from 1971 to 2013 by fuel (Mt of CO₂).

“CO₂ is a greenhouse gas in the exhaust gases of combustion from GTs and ICEs. CO₂ emissions from engines can be reduced by improving fuel economy, using a fuel with higher hydrogen to carbon ratio (H/C) or using a renewable fuel. The fuel economy of GT and ICE can be improved by operating the engine with diluted mixtures through extra air or exhaust gas recirculation (EGR) due to low temperature combustion, low heat transfer losses and low pumping losses at part loads. Direct injection SI engines have reduced pumping losses and heat transfer losses and, hence, have lower fuel consumption. Homogenous charge compression ignition (HCCI) gasoline engines using diluted mixtures can also improve their fuel economy,” [4].

The CO₂ is not the only harmful pollutant resulting from fossil fuel combustion but many other pollutants are produced. Combustion of standard fossil fuels in commercial and industrial combustors results in the following nine emissions; carbon dioxide, nitrogen, oxygen, water, carbon monoxide, nitrogen oxide, sulphur oxides, volatile organic compounds, and particulate matter. The latter five products of combustion are considered pollutants and are known to, either directly or indirectly, cause harmful effects on humans and the environment [5].

This thesis is concerned with the CFD analysis of turbulent combustion of lean premixed fossil fuel/hydrogen/air mixtures in a swirl burner, using the ANSYS/Fluent Software.

This research focuses on natural gas/hydrogen, i.e., methane/hydrogen/air mixtures and propane/ hydrogen/air mixtures.

It is well known that in turbulent regimes the flame speed of fossil fuels is a function of velocity fluctuation intensity, the equivalence ratio, the content of hydrogen, and to far less extension, a function of hydrocarbon fuel type. For that reason, the ANSYS/Fluent combustion modelling is based on the solution of a transport equation for the reaction progress variable. The previous experimental findings of premixed natural gas, propane and air mixtures combustion in this swirl burner, used in this thesis, strongly support the assumption that under turbulent premixed conditions, the turbulent flame speed practically does not depend on a gaseous hydrocarbon fuel type. Keeping that in mind, the availability of pure propane (>99.5 vol %) contrary to the variable composition of natural gas, favors propane as the model, base fuel. Furthermore, the published experimental results using this burner, were for propane, therefore this thesis basically deals with propane as the model fuel of methane and natural gas.

2 Chapter2

2.1 Introduction

The environmental issues of electrical power generation and energy production play an important role in the economic development of modern power plants. In conventional power plant, the industrial gas turbines operate on hydrocarbons with lean premixed flames. Alternative energy such as blended hydrocarbon/hydrogen fuels have recently become important particularly as an attractive fuel [6]. These blends have several advantages due to the beneficial hydrogen characteristics.

Hydrogen has high specific energy on mass basis, it can be generated from various energy sources, it is renewable and it can be a very clean alternative to hydrocarbons, as there is no CO, CO₂, SO_x and UHC emissions from its combustion products [7]

Reduction of emissions has been one of the major challenges and activities of researchers and engineers in combustion technologies. The use of hydrogen and hydrogen enriched fossil fuels appears to be an effective way to low carbon energy production. Besides, hydrogen is a renewable energy source, an energy storage medium and can be directly used in mixtures with natural gas and liquefied petrol gases (LPG) in existing gas piping and combustion systems [8-10].

Hydrogen is a clean, excellent fuel, which combustion product is water. Hydrogen production is based on a number of methods: use of solar, wind and nuclear energy, steam methane reforming, conversion of coal and biomass to hydrogen, water electrolysis and others. Once produced, hydrogen is also considered a renewable energy. One should particularly pay attention to solar and wind energy for hydrogen production at competitive costs resulting from the fast technological developments.

The main limitations of solar and wind power energy sources are site-specific operation, costs and intermittency [11, 12]. Regarding the intermittency problem, energy storage becomes very important and urgent issue [13].

Using batteries to store any energy surplus for later consumption can resolve the time mismatch between energy supply and demand. The shortcomings of battery storage are

high priced, low-storage capacity, shorter equipment life, and considerable solid and wastes generated [14].

In order to better exploit renewable energy, hydrogen has been identified as potential alternative fuel, as well as, an energy storage carrier for the future energy supply [15, 16].

Hydrogen energy storage system presents an opportunity to increase the flexibility and resiliency of the sustainable energy supply system while potentially reducing overall energy costs on account of system integration and better utilization of renewable energy. On the other hand, its low density poses a storage problem [17].

Using pure hydrogen is possible, but not feasible in existing energy utilization systems. One of the possible solutions is hydrogen blending with other gaseous fuels. Blended hydrogen into the existing gas pipeline networks has been proposed as a means of increasing the output of renewable energy systems [18].

At relatively low concentrations of up to 10% vol. hydrogen may be safely injected into existing fossil fuel gas pipeline systems with only minor modifications [19]. Realizing the growing importance of hydrogen, many researchers have focused their investigations on different aspects of its production and use. Nevertheless, in the available literature, there is a lack of published research on combustion of mixtures of liquefied petroleum gases (LPG) and hydrogen.

2.2 Review of previous work

Marcin Dutk et al. [20] performed an experimental investigation to study the emission characteristics of a novel low NO_x burner fueled by hydrogen rich mixtures with methane. The burner was tested in a cylindrical combustion chamber at atmospheric pressure. A burner thermal load of 25 kW and air-fuel equivalence ratio of 1.15 was maintained for various fuel compositions throughout the experimental tests. The investigation showed that lowest NO_x emissions were below 9 ppm and 14 ppm, at 3% of O₂ for 5% and 30% mass fraction of hydrogen in the fuel respectively.

The effect of hydrogen addition to ultra-lean counter flow CH₄/air premixed flame on the extinction limits and the characteristics of NO_x emissions were studied numerically by Horgsheng Guo et al [21]. They indicated that the addition of hydrogen can significantly

enlarge the flammable region and extend the flammability limit to lower equivalence ratios, and in constant equivalence ratio, the addition of hydrogen increases the emission of NO. Peter Therkelsen et al [22] implemented an experimental investigation to study the NO_x formation in hydrogen-fueled gas turbine engine. Three sets of fuel injectors were developed to facilitate stable operation while generating differing levels of fuel/air mixture non-uniformity. One set was designed to produce near uniform mixing while the others had differing degrees of non-uniformity. The higher emission of NO was found even with nearly perfect premixing when operated on hydrogen than when operated with natural gas.

A. Choudhuri et al [23] carried out an experimental investigation to study the characteristics of combustion and pollution of a diffusion flame in a vertical combustion chamber. The authors investigated a range of different fuel blends by varying the volumetric fractions of propane in the fuel mixture (5% up to 35% vol). They reported that the emission index of NO_x was 0.90 [gkg⁻¹], at the baseline condition (95% hydrogen and 5% propane) which decreased to 0.34 [gkg⁻¹], for 65-35% hydrogen/propane mixture. To the authors' knowledge, there are no published papers on LPG/hydrogen mixture effects on NO_x emission for a swirl premixed micro gas turbine combustor.

There have been only few studies dealing with the effect of different swirl intensities on hydrogen enriched hydrocarbon-air premixed flame. Syred et al. [24] performed an experimental investigation to study and reduce the effect of flashback in a compact design generic swirl premixed burner representative of many systems. A range of different fuel blends which include methane, methane/hydrogen blends, pure hydrogen and coke oven gas were investigated for flashback and blow off limits. In addition, they studied three swirl numbers ($S_1=1.47$, $S_2=1.04$ and $S_3=0.8$) by varying the inlets or the configuration of the inlets in the used compact burner. They found two flashback phenomena that are encountered in that study. The first one at lower swirl number ($S=0.8$) involves flashback through the outer wall boundary layer where the crucial parameter is the critical boundary velocity gradient. The second one at higher swirl number ($S=1.47$) the central recirculation zone (CRZ) becomes enlarged and extends backwards over the fuel injector to the burner baseplate for all fuel and causes flashback to occur earlier at higher velocities. Also, the reported for the lower swirl number ($s =0.8$) the best flashback limits for methane based

fuels with hydrogen. Kim et al. [25] carried out an experimental study of the effect of hydrogen addition in methane-air premixed flames in a laboratory-scale swirl-stabilized combustor operated at 5.81 kW. Different swirlers investigated to identify the role of swirl strength to the incoming mixture. The flame stability was examined for the effect of amount of hydrogen addition, combustion air flow rates and swirl strengths. This was done via comparing adiabatic flame temperature at the lean flame limit. The combustion characteristics of hydrogen-enriched methane flame at constant heat load but different swirl strengths examined using particle image velocimetry, micro-thermocouples and OH chemiluminescence diagnostics. The authors reported that the lean stability limit is extended by hydrogen addition and also, the stability limit can reduce at higher swirl intensity to the fuel-air mixture operating at lower adiabatic flame temperatures. They found also that the addition of hydrogen increases the NO_x emission; however, this effect can be reduced by increasing either the excess air or swirl intensity. They also compared emission of NO_x and CO from the premixed flame with a diffusion flame type combustor, the result shows that the NO_x emissions of hydrogen-enriched methane premixed flame were lower than the corresponding diffusion flame under the same operating conditions for the fuel-lean case.

Due to the complex turbulent nature of reacting swirling flows, there are different kinds of models and methods are utilized to simulate all kinds of characteristics of flams. The choice of a suitable model to accurate numerical simulations of such flows requires a careful choice. It is necessary to simulate the combustion characteristics of gas burner since CFD technology can provide more details of flow field than experiment.

There are some of investigations which focus on the simulation of the turbulence flow. The model of k- ϵ with standard wall function is usually accepted and can perform reasonably well for simulating simple turbulent flows.

Roberto M. [26] carried out 3D numerical combustion simulation in a can burner fed with methane to evaluate pollutant emission and the temperature. The k- ϵ model with standard wall function was used to model the turbulent effects. The model was validated against experimental data. He found that numerical results shows a good agreement with the

experimental data in most of the cases, and the best results were obtained in the NO_x prediction, while unburned fuel was slightly overestimated.

A numerical study of confined swirling flows in a cylindrical combustor, it was reported that the standard k- ϵ model shows overestimate the level of turbulent diffusion on the turbulent swirling flow. It is reported that the deficiency of the standard k- ϵ model is due to the use of isotropic eddy viscosity concept, which is not the case for most turbulent swirling flow structures that are anisotropic [27, 28].

To treat the defect of the standard k- ϵ model, a new wall function which named Realizable wall function (Realizable k- ϵ model) was purposed by [29] such model includes a new eddy viscosity formula and a new dissipation rate equation.

Adel Gayed et al. [30] performed numerically study of premixed high swirl flow in a gas turbine combustor using the Realizable k- ϵ model. The found a good agreement between the calculated and measured axial and tangential velocities distribution over the whole combustor.

A numerical computation of premixed propane in a swirl-stabilized burner performed by [31] the numerical simulation was carried out using Reynolds-Average-Stokes (RANS) technique with realizable k- ϵ model as a turbulence closure model, the study was performed with two swirl numbers ($S=0.6$ and $S=1.05$), they show that the validations of the computational models with the experimental date were a good agreement.

For combustion modeling of swirling flows, appropriate turbulence-chemistry interaction models are required to account for the chemistry of the flame and its interaction with the turbulence swirling flow in a detailed way.

Characteristic of combustion temperature, flow velocity, CO distribution and NO_x emissions of a 10 MW gas turbine burner at different primary to secondary air ratios were investigated numerically using computational fluid dynamics software fluent [32], the realizable k- ϵ model with the standard wall function was employed to predict the turbulence in the combustion system. A mixture-fraction equation was solved instead of equations of individual species, and the individual species concentration was derived from the predicted mixture fraction concentration under the assumption of chemical equilibrium. Interaction between turbulence and chemistry was accounted with the β function probability density

function. The Simple algorithm was used to solve the pressure-velocity coupling and a second-order discretization scheme was utilized to solve all governing equations. They reported that the inner flames are the main flame and there is a swirling flow formed between the inner and the outer flames. With the increase of primary to secondary air ratio, the heating area is more concentrated. Meanwhile, the capacity of the swirling flow to absorb the high temperature flue gas enhances, which improves the stability of flames. And also, the distribution situations of mass fraction and generated NO_x have a close relationship with the flame shape.

Magnussen et al. [33] reported that the Eddy-Dissipation concept model lead to good numerical prediction.

Ilker Y. [34] performed a numerical study to investigate the effect of swirl number on combustion characteristics such as temperature, velocity, gas concentration in a natural gas diffusion flame, the combustion reaction scheme in the flame region was modeled using eddy dissipation model with one step global reaction scheme. The standard k- ϵ turbulence model for turbulence closure and P1 radiation model for flame radiation inside the combustor were used in the numerical simulations. Also, the investigation included study the effect of swirling on the combustion characteristics with seven swirl number (0.1, 0.2, 0.3, 0.4, 0.5 and 0.6). The numerical results validated and compared with the published experimental results. He reported that a good consistency was found between numerical and experimental results, also, he reported that the gas concentrations are strongly affected by the swirl number.

De. A et al. [35] assessed the Eddy-Dissipation concept in combustion k- ϵ turbulence models and chemical kinetic schemes for about 20 species, on the Delft jet in hot coflow. They reported that the realizable k- ϵ model exhibits better performance in the prediction of entrainment, compared by standard k- ϵ model. However, the Eddy-Dissipation concept model correctly predicts the experimentally observed decreasing trend of liftoff height with jet Reynolds number. More simple and cost effective model which takes in to account the finite rate chemistry is the Finite-Rate/Eddy-Dissipation model (FR/EDM). It provides an adequate prediction for the flame chemistry and its interaction with swirling flow [36, 37]

Large-eddy simulation of a low swirl stratified premixed flame was performed by using FR/EDC with empirical two-step reduced methane reaction mechanism. They reported that the FR/EDC model produced good predictions of the means and rms velocity fields, temperature and fuel distributions [36].

Another parameter has great effects on the modeling of turbulent swirling flames is the radiation models. Mustafa Ibas [38] performed numerical computations of the effect of radiation models on hydrogen-hydrocarbon turbulent non-premixed flame. He found that the results with the radiation models are in better agreement with the measurements compared with the results without radiation model, by means of temperature and NO_x emissions.

Yilmaz et al. [37] performed a numerical simulation to study the effect of the turbulence and radiation models on the combustion characteristics of the propane-hydrogen diffusion flames. Two different radiation models are examined including P-1 model and Discrete Transfer Radiation model. They found that in terms of predictive accuracy, the temperature gradients obtained with two radiations models are not similar. The predicted temperature gradient with Discrete Transfer Radiation model are not agreement with experiment and simulation results published in the literature.

The P-1 radiation model shows a better overall agreement with the experimental data and other simulation results at different axial distances in the combustion chamber.

Only few works of the effect of different swirl intensities and different equivalence ratios on H_2 containing fuels premixed flames are investigated experimentally.

An experimental research of a purposely designed laboratory-scale lean-premixed combustor with a variable center body length and swirling number was used. During this research, the center body length was varied to 1/3 and 2/3 of the full length, thus making a hybrid turbo-annular combustor to enable better understanding of gradual change from one combustor type to the other. In addition, the other basic variables, such as equivalence ratio and swirl were systematically varied. The fuel-air mixture was prepared in a mixing chamber and injected through a swirler into the combustor. The tests were performed at atmospheric conditions, pressure of 101.3 kPa and temperature of 20° C. The fuel and air flow rates were measured using calibrated rotameters. The exhaust gas composition was

measured using Testo 350-XL and Testo 454 flue gas analyzers. To get representative flue gas samples and to prevent the outer air from interfering with exhaust gases, an extension tube with the same inner diameter and length as the combustor was attached to the combustor exit. The exhaust gas was sampled with a cooled stainless steel probe and transported through a heated tube to the gas analyzer. The cooling water flow rates for the center body and combustor were controlled independently while the temperature of water was measured using glass/mercury thermometers. The measured values of NO_x were corrected to 15% O₂ flue gases dry conditions [40].

The aim of this study is to investigate numerically the effect of hydrogen enrichment, swirl intensity and equivalence ratio on the combustion characteristics of premixed propane flame on the purposely designed laboratory-scale which studied experimentally by [40]

The numerical computations play a fundamental role in achieving this task. ANSYS-Fluent 16 CFD tool [41] is used in this study.

3 CHAPTER 3

3.1 COMBUSTION MODELLING BY CFD

The use of computational fluid dynamics (CFD) to predict internal and external flows has risen dramatically in the past decade. The widespread availability of engineering workstations together with the efficient solution of algorithms and sophisticated pre- and post- processing facilities enable the use of commercial CFD codes by graduate engineers for research, development and design task in industry. Increasingly CFD is becoming a vital component in the design of industrial products and processes. Also the rapid progress in generating high-powered super-fast computers helps in creating more efficient CFD software that have higher accuracy and more efficient prediction with lower cost [42].

“The ultimate aim of developments in the CFD field is to provide a capability comparable to the other Computer-Aided Engineering (CAD) tools such as stress analysis codes. The main reason why CFD has lagged behind is the tremendous complexity of the underlying behavior; at the moment this precludes a complete description of fluid flows and assumptions of time averaged flows is commonly made to give representative solutions that are at the same time economical and sufficiently complete. The availability of affordable high performance computing hardware and the introduction of user friendly interfaces have led to recent upsurge of the interest in CFD for use in many different research and industrial communities” [43].

3.1.1 Governing equations of fluid dynamics

The cornerstone of computational fluid dynamics is the fundamental governing equations of fluid dynamics – the continuity, momentum and energy equations.

3.1.1.1 Mass conservation

The mathematical expression of continuity equation for mass conservation can be written by:

$$\frac{\partial \rho}{\partial t} + \nabla \cdot (\rho \vec{V}) = 0 \dots\dots\dots (1-3).$$

Or can be expressed by

$$\frac{\partial \rho}{\partial t} + \frac{\partial(\rho u)}{\partial x} + \frac{\partial(\rho v)}{\partial y} + \frac{\partial(\rho w)}{\partial z} = 0 \dots\dots\dots (2-3)$$

Equations (1-3) is unsteady, three dimensional mass continuity equation at a point in a compressible flow, the first term on the left side represents the rate of change in time of the density while, the second term is the net flow of mass out of the element across its boundary.

3.1.1.2 Momentum Equation

The momentum equation is a statement of Newton's Second Law and relates the sum of the forces acting on an element of fluid to its acceleration or rate of change of momentum. By Applying Newton's Second Law to a fluid passing through an infinitesimal, fixed control volume, in x, y and z directions:

The x-component

$$\rho \frac{Du}{Dt} = \frac{\partial(-p+\tau_{xx})}{\partial x} + \frac{\partial\tau_{yx}}{\partial y} + \frac{\partial\tau_{zx}}{\partial z} + \rho f_x \dots\dots\dots(3-3)$$

The Y-component

$$\rho \frac{Dv}{Dt} = \frac{\partial\tau_{xy}}{\partial x} + \frac{\partial(-p+\tau_{yy})}{\partial y} + \frac{\partial\tau_{zy}}{\partial z} + \rho f_y \dots\dots\dots(4-3)$$

The Z-component

$$\rho \frac{Dw}{Dt} = \frac{\partial\tau_{xz}}{\partial x} + \frac{\partial\tau_{yz}}{\partial y} + \frac{\partial(-p+\tau_{zz})}{\partial z} + \rho f_z \dots\dots\dots(5-3)$$

Equations (3-3, 4-3 and 5-3) are the x-, y- and z-components respectively of the momentum equation. "Note that they are partial differential equations obtained directly from an application of the fundamental physical principle to an infinitesimal fluid element. Moreover, since this fluid element is moving with the flow, equations (3-3, 4-3 and 5-3) are

in non-conservation form. They are scalar equations, and are called the Navier–Stokes equations

“In the late seventeenth century Isaac Newton stated that shear stress in a fluid is proportional to the time-rate-of-strain, i.e. velocity gradients. Such fluids are called Newtonian fluids. (Fluids in which τ is not proportional to the velocity gradients are non-Newtonian fluids),” [44].

The complete Navier–Stokes equations can be obtained in conservation form as follows:

$$\frac{\partial(\rho u)}{\partial t} + \frac{\partial(\rho u^2)}{\partial x} + \frac{\partial(\rho uv)}{\partial y} + \frac{\partial(\rho uw)}{\partial z} = -\frac{\partial p}{\partial x} + \frac{\partial}{\partial x} \left(\lambda \nabla \cdot \vec{V} + 2\mu \frac{\partial u}{\partial x} \right) + \frac{\partial}{\partial y} \left[\mu \left(\frac{\partial v}{\partial x} + \frac{\partial u}{\partial y} \right) \right] + \frac{\partial}{\partial z} \left[\mu \left(\frac{\partial u}{\partial z} + \frac{\partial w}{\partial x} \right) \right] + \rho f_x \dots \dots \dots (6-3)$$

$$\frac{\partial(\rho v)}{\partial t} + \frac{\partial(\rho v^2)}{\partial y} + \frac{\partial(\rho uv)}{\partial x} + \frac{\partial(\rho vw)}{\partial z} = -\frac{\partial p}{\partial y} + \frac{\partial}{\partial y} \left(\lambda \nabla \cdot \vec{V} + 2\mu \frac{\partial v}{\partial y} \right) + \frac{\partial}{\partial x} \left[\mu \left(\frac{\partial v}{\partial x} + \frac{\partial u}{\partial y} \right) \right] + \frac{\partial}{\partial z} \left[\mu \left(\frac{\partial w}{\partial y} + \frac{\partial v}{\partial z} \right) \right] + \rho f_y \dots \dots \dots (7-3)$$

$$\frac{\partial(\rho w)}{\partial t} + \frac{\partial(\rho w^2)}{\partial z} + \frac{\partial(\rho uw)}{\partial x} + \frac{\partial(\rho vw)}{\partial y} = -\frac{\partial p}{\partial z} + \frac{\partial}{\partial z} \left(\lambda \nabla \cdot \vec{V} + 2\mu \frac{\partial w}{\partial z} \right) + \frac{\partial}{\partial x} \left[\mu \left(\frac{\partial u}{\partial z} + \frac{\partial w}{\partial x} \right) \right] + \frac{\partial}{\partial y} \left[\mu \left(\frac{\partial w}{\partial y} + \frac{\partial v}{\partial z} \right) \right] + \rho f_z \dots \dots \dots (8-3)$$

Where μ is the molecular viscosity coefficient and λ is the bulk viscosity coefficient

3.1.1.3 Energy Equation

The energy equation is extract from the first law of thermo dynamics which expresses that the rate of change of energy inside the fluid element is equal to the net flux of heat into the element plus the rate of working done on the element due to body and surface force.

The net rate of work done on the moving fluid element due to surface forces can be expressed as [44].

$$-\nabla \cdot (p\vec{V}) + \left[\frac{\partial(u\tau_{xx})}{\partial x} + \frac{\partial(u\tau_{yx})}{\partial y} + \frac{\partial(u\tau_{zx})}{\partial z} + \frac{\partial(v\tau_{xy})}{\partial x} + \frac{\partial(v\tau_{yy})}{\partial y} + \frac{\partial(v\tau_{zy})}{\partial z} + \frac{\partial(w\tau_{xz})}{\partial x} + \frac{\partial(w\tau_{yz})}{\partial y} + \frac{\partial(w\tau_{zz})}{\partial z} \right] dx dy dz + \rho \vec{f} \cdot \vec{V} dx dy dz \dots \dots \dots (9-3)$$

The net flux of heat into the element represented the heat flux due to: (1) volumetric heating such as absorption or emission of radiation, and (2) heat transfer across the surface due to temperature gradients.

$$\left[\rho \dot{q} + \frac{\partial}{\partial x} \left(k \frac{\partial T}{\partial x} \right) + \frac{\partial}{\partial y} \left(k \frac{\partial T}{\partial y} \right) + \frac{\partial}{\partial z} \left(k \frac{\partial T}{\partial z} \right) \right] dx dy dz \dots \dots \dots (10-3)$$

Where k is the thermal conductivity.

The total energy of a moving fluid per unit mass is the sum of its internal energy per unit mass, e , and its kinetic energy per unit mass, $\frac{v^2}{2}$

The time-rate-of-change of energy per unit mass is given by

$$\rho \frac{D}{Dt} \left(\frac{v^2}{2} + e \right) dx dy dz \dots \dots \dots (11-3)$$

The energy equation can be written as: [44].

$$\rho \frac{D}{Dt} \left(\frac{v^2}{2} + e \right) dx dy dz = \rho \dot{q} + \frac{\partial}{\partial x} \left(k \frac{\partial T}{\partial x} \right) + \frac{\partial}{\partial y} \left(k \frac{\partial T}{\partial y} \right) + \frac{\partial}{\partial z} \left(k \frac{\partial T}{\partial z} \right) - \nabla \cdot (p\vec{V}) + \frac{\partial(u\tau_{xx})}{\partial x} + \frac{\partial(u\tau_{yx})}{\partial y} + \frac{\partial(u\tau_{zx})}{\partial z} + \frac{\partial(v\tau_{xy})}{\partial x} + \frac{\partial(v\tau_{yy})}{\partial y} + \frac{\partial(v\tau_{zy})}{\partial z} + \frac{\partial(w\tau_{xz})}{\partial x} + \frac{\partial(w\tau_{yz})}{\partial y} + \frac{\partial(w\tau_{zz})}{\partial z} + \rho \vec{f} \cdot \vec{V} \dots \dots \dots (12-3)$$

3.1.2 Differential forms of general Transport Equation

“There are significant commonalities between the prior various equations. If a general variable ϕ is introduced, the conservative form of all fluid flow equations, including

equations for scalar quantities such as temperature and pollutant concentration can usefully be written in the following form

$$\frac{\partial(\rho\phi)}{\partial t} + \text{div}(\rho\phi U) = \text{div}(\Gamma \text{grad } \phi) + S_\phi \dots \dots \dots (13-3)$$

The rate of increase of ϕ of fluid element plus the net of flow of ϕ out of fluid element is equal to the sum of rate of increase ϕ due to diffusion plus rate of increase of ϕ due to sources,”[42].

3.2 Modeling Turbulence

“The fluctuating in velocity fields occur in turbulent flow, this fluctuating cause blend transported quantities such as momentum, energy, and species concentration. Since these fluctuations can be of small scale and high frequency, they are too computationally expensive to simulate directly in practical engineering calculations. Instead, the instantaneous (exact) governing equations can be time-averaged, ensemble-averaged, or otherwise manipulated to remove the resolution of small scales, resulting in a modified set of equations that are computationally less expensive to solve. The modified equations contain additional unknown variables, and turbulence models are needed to determine these variables in terms of known quantities” [45].

3.2.1 Classification turbulent flow model in fluent

“In fact, there is no a unique turbulence model can be universally admitted as being superior for all classes of problems. Fluent has a wide variety of models to be suitable for the requirements different classes of engineering problems, however, the selection of the turbulence model depends on the desired level of precision , computational resources, and calculation time,” [46].

3.2.1.1 Standard k – ε model

“The standard k – ε model in Ansys fluent has become the workhorse of practical engineering flow calculations in the time since it was proposed by Launder and Spalding. Robustness, economy, and reasonable accuracy for a wide range of turbulent flows explain its popularity in industrial flow and heat transfer simulation. It is semi-empirical model, and the derivation of the model equations relies on phenomenological considerations and empiricism.

The assumption in derivation of k – ε model is that the flow is fully turbulent, and the effects of molecular viscosity are negligible. And the model transport equation for k is derived from the exact equation, while the model transport equation for ε was obtained using physical reasoning and bears little resemblance to its mathematically exact counterpart,” [43].

The turbulent kinetic energy, k and its rate of dissipation, ε, are obtained from the following transport equations:

$$\frac{\partial}{\partial t}(\rho k) + \frac{\partial}{\partial x_i}(\rho k u_i) = \frac{\partial}{\partial x_j} \left[\left(\mu + \frac{\mu_t}{\sigma_k} \right) \frac{\partial k}{\partial x_j} \right] + G_k + G_b - \rho \varepsilon - Y_M + S_k \dots \dots \dots (14-3)$$

$$\frac{\partial}{\partial t}(\rho \varepsilon) + \frac{\partial}{\partial x_i}(\rho \varepsilon u_i) = \frac{\partial}{\partial x_j} \left[\left(\mu + \frac{\mu_t}{\sigma_\varepsilon} \right) \frac{\partial \varepsilon}{\partial x_j} \right] + C_{1\varepsilon} \frac{\varepsilon}{k} (G_k + C_{3\varepsilon} G_b) - C_{2\varepsilon} \rho \frac{\varepsilon^2}{k} + S_\varepsilon \dots \dots \dots 15-3)$$

In these equations, G_k represents the generation of turbulence kinetic energy due to the mean velocity gradients, calculated as follows:

$$G_k = -\rho \overline{u'_i u'_j} \frac{\partial u_j}{\partial x_i} \dots \dots \dots (16-3)$$

G_b is the generation of turbulence kinetic energy due to buoyancy, calculated by this equation

$$G_b = \beta g_i \frac{\mu_t}{Pr_t} \frac{\partial T}{\partial x_i} \dots\dots\dots(17-3)$$

Where: Pr_t is the turbulent Prandtl number for energy and g_i is the component of gravitational vector in the i^{th} direction. And β is the coefficient of thermal expansion which defined as

$$\beta = -\frac{1}{\rho} \left(\frac{\partial \rho}{\partial T} \right)_P \dots\dots\dots(18-3)$$

Y_M represents the contribution of the fluctuating dilatation in compressible turbulence to the overall dissipation rate, which is calculated as

$$Y_M = 2\rho\varepsilon M_t^2 \dots\dots\dots(19-3)$$

where: M_t is the turbulent Mach number.

$C_{1\varepsilon}$, $C_{2\varepsilon}$ and $C_{3\varepsilon}$ are constant. σ_k and σ_ε are the turbulent Prandtl numbers for k and ε , respectively. S_k and S_ε are user-defined source terms.

The turbulent viscosity, μ_t is computed by combining k and ε as follows:

$$\mu_t = \rho C_\mu \frac{k^2}{\varepsilon} \dots\dots\dots (20-3)$$

The model constants $C_{1\varepsilon}$, $C_{2\varepsilon}$, C_μ , σ_k and σ_ε have the following default values:

$$C_{1\varepsilon} = 1.44, C_{2\varepsilon} = 1.92, C_\mu = 0.09, \sigma_k = 1.0, \sigma_\varepsilon = 1.3$$

These default values have been determined from experiments for fundamental turbulent flows.

3.2.1.2 Realizable k – ε model

The Reynolds-average approach to turbulence modeling requires that the Reynolds stresses in this equation

$$\frac{\partial}{\partial t}(\rho u_i) + \frac{\partial}{\partial x_j}(\rho u_i u_j) = -\frac{\partial p}{\partial x_i} + \frac{\partial}{\partial x_j} \left[\mu \left(\frac{\partial u_i}{\partial x_j} + \frac{\partial u_j}{\partial x_i} - \frac{2}{3} \delta_{ij} \frac{\partial u_l}{\partial x_l} \right) \right] + \frac{\partial}{\partial x_j} (-\rho \overline{u'_i u'_j}) \dots \dots (21-3)$$

In the above equation, the additional terms appear that represents the effects of turbulence. These Reynolds stresses, $-\rho \overline{u'_i u'_j}$, must be modeled. A common method employs the Boussinesq hypothesis to relate the Reynolds stresses to the mean velocity gradients:

$$-\rho \overline{u'_i u'_j} = \mu_t \left(\frac{\partial u_i}{\partial x_j} + \frac{\partial u_j}{\partial x_i} \right) - \frac{2}{3} \left(\rho k + \mu_t \frac{\partial u_k}{\partial x_k} \right) \delta_{ij} \dots \dots \dots (22-3)$$

In the Realizable $k - \varepsilon$ model, the combining between the Boussinesq hypothesis eq. (22-3) and the eddy viscosity definition eq. (20-3) to obtain the following expression for the normal Reynolds stresses in an incompressible strained mean flow:

$$\overline{u^2} = \frac{2}{3} k - 2\nu_t \frac{\partial U}{\partial x} \dots \dots \dots (23-3)$$

3.2.1.3 Transport equations for the Realizable $k - \varepsilon$ model

The modeled transport equations for k and ε in the realizable $k - \varepsilon$ model are

$$\frac{\partial}{\partial t}(\rho k) + \frac{\partial}{\partial x_j}(\rho k u_j) = \frac{\partial}{\partial x_j} \left[\left(\mu + \frac{\mu_t}{\sigma_k} \right) \frac{\partial k}{\partial x_j} \right] + G_k + G_b - \rho \varepsilon - Y_M + S_k \dots \dots \dots (24-3)$$

And

$$\begin{aligned} \frac{\partial}{\partial t}(\rho \varepsilon) + \frac{\partial}{\partial x_j}(\rho \varepsilon u_j) \\ = \frac{\partial}{\partial x_j} \left[\left(\mu + \frac{\mu_t}{\sigma_\varepsilon} \right) \frac{\partial \varepsilon}{\partial x_j} \right] + \rho C_1 S \varepsilon - \rho C_2 \frac{\varepsilon^2}{k + \sqrt{\nu \varepsilon}} + C_{1\varepsilon} \frac{\varepsilon}{k} C_{3\varepsilon} G_b + S_\varepsilon \end{aligned} \quad (25 - 3)$$

Where

$$C_1 = \max \left[0.43, \frac{\eta}{\eta + 5} \right], \eta = S \frac{k}{\varepsilon}, S = \sqrt{2S_{ij}S_{ij}}$$

The eddy viscosity for realizable k – ε model can be calculated by

$$\mu_t = \rho C_\mu \frac{k^2}{\varepsilon} \dots\dots\dots(26-3)$$

The difference between the realizable k – ε model and the standard k – ε model is that C_μ is no longer constant. It is computed from

$$C_\mu = \frac{1}{A_0 + A_s \frac{kU^*}{\varepsilon}} \dots\dots\dots(27-3)$$

Where:

$$U^* \equiv \sqrt{S_{ij}S_{ij} + \tilde{\Omega}_{ij}\tilde{\Omega}_{ij}} \dots\dots\dots(28-3)$$

And

$$\tilde{\Omega}_{ij} = \Omega_{ij} - 2\varepsilon_{ijk}\omega_k \dots\dots\dots(29-3)$$

$$\Omega_{ij} = \bar{\Omega}_{ij} - \varepsilon_{ijk}\omega_k \dots\dots\dots(30-3)$$

The $\bar{\Omega}_{ij}$ is the mean rate-of –rotation tensor viewed in a moving reference with the angular velocity ω_k . The constant A_0 and A_s are given by

$$A_0 = 4.04, \quad A_s = \sqrt{6}\cos\varnothing$$

Where:

$$\varnothing = \frac{1}{3}\cos^{-1}(\sqrt{6}W) \dots\dots\dots(31-3)$$

$$W = \frac{S_{ij}S_{jk}S_{ki}}{\tilde{S}^3} \dots\dots\dots(32-3)$$

$$\tilde{S} = \sqrt{S_{ij}S_{ij}} \dots\dots\dots(33-3)$$

$$S_{ij} = \frac{1}{2}\left(\frac{\partial u_j}{\partial x_i} + \frac{\partial u_i}{\partial x_j}\right) \dots\dots\dots(34-3)$$

“The alternative approach, embodied in the RSM is to solve transport equations for each of the terms in the Reynolds stress tensor. An additional scale-determining equation is also required. This means that five additional transport equations are required in 2D flows and seven additional transport equations must be solved in 3D.

In many cases, models based on the Boussinesq hypothesis performed very well, and the additional computational expense of the Reynolds stresses model is not justified. However, the RSM is clearly superior in situations where the anisotropy of turbulence has a dominant effect on the mean flow. Such cases include highly swirling flows and stresses-driven secondary flows,” [45].

3.2.1.4 Reynolds Stress Model (RSM)

“The Reynolds stress model is the most elaborate type of RANS model that ANSYS Fluent provides. Abandoning the isotropic eddy-viscosity hypothesis, the RSM closes the Reynolds-averaged Navier-Stokes equations by solving transport equations for the Reynolds stresses, together with an equation for the dissipation rate. This means that five additional transport equations are required in 2D flows, in comparison to seven additional transport equations solved in 3D. Since the RSM accounts for the effect of streamline, swirl, rotation, and rapid changes in strain rate in a more rigorous manner than one-equation and two-equation models, it has greater potential to give accurate predictions for complex flows,” [45].

The exact transport equations for the transport of the Reynolds stresses, $\overline{\rho u'_i u'_j}$ is written as follows:

$$\frac{\partial}{\partial t} (\overline{\rho u'_i u'_j}) + \frac{\partial}{\partial x_k} (\rho x_k \overline{u'_i u'_j}) = -\frac{\partial}{\partial x_k} [\overline{\rho u'_i u'_j u'_k} + \overline{p'(\delta_{kj} u'_i + \delta_{ik} u'_j)}] + D_{L,ij} - P_{ij} - G_{ij} + \phi_{ij} - \varepsilon_{ij} - F_{ij} + S_{user} \dots \dots \dots (35-3)$$

Where:

$$D_{L,ij} = \frac{\partial}{\partial x_k} \left[\mu \frac{\partial}{\partial x_k} (\overline{u'_i u'_j}) \right] \text{ Molecular Diffusion.}$$

$$P_{ij} = \rho \left[\overline{u'_i u'_k} \frac{\partial u_j}{\partial x_k} + \overline{u'_j u'_k} \frac{\partial u_i}{\partial x_k} \right] \text{ stresses production}$$

$$G_{ij} = \rho \beta (g_i \overline{u'_j \theta} + g_j \overline{u'_i \theta}) \text{ Bouyancy Production}$$

$$\phi_{ij} = P' \left[\frac{\partial u'_i}{\partial x_j} + \frac{\partial u'_j}{\partial x_i} \right] \text{ pressure strain}$$

$$\varepsilon_{ij} = 2\mu \frac{\partial u'_i}{\partial x_k} \frac{\partial u'_j}{\partial x_k} \text{ Dissipation}$$

$$F_{ij} = 2\rho \Omega_k (\overline{u'_i u'_m} \varepsilon_{ikm} + \overline{u'_j u'_m} \varepsilon_{jkm}) \text{ production by system rotation}$$

The modeling of turbulent diffusive transport has been simplified in ANSYS Fluent to use a scalar turbulent diffusivity as follows

$$D_{T,ij} = \frac{\partial}{\partial x_k} \left(\frac{\mu_t}{\sigma_k} \frac{\partial \overline{u'_i u'_j}}{\partial x_k} \right) \dots \dots \dots (36-3)$$

Lien and Leschziner derived a value of $\sigma_k = 0.82$ by applying the generaling gradient-diffusion model to the case of a planar homogeneous shear flow.

1. modeling the pressure-strain
2. linear pressure-strain model

The classical approach to modeling ϕ_{ij} uses the following decomposition:

$$\phi_{ij} = \phi_{ij,1} + \phi_{ij,2} + \phi_{ij,w}$$

Where $\phi_{ij,1}$ is the slow pressure-strain term, also known as the return-to-isotropy term, $\phi_{ij,2}$ is called the rapid pressure-strain term, and $\phi_{ij,w}$ is the wall-reflection term.

The slow pressure-strain term, $\phi_{ij,1}$ is modeled as follows

$$\phi_{ij,1} \equiv -C_1 \rho \frac{\varepsilon}{k} \left[\overline{u'_i u'_j} - \frac{2}{3} \delta_{ij} k \right] \dots \dots \dots (37-3)$$

Where $C_1 = 1.8$

The rapid pressure-strain term $\phi_{ij,2}$ is modeled as follows

$$\phi_{ij,2} \equiv -C_2 \left[\left(P_{ij} + F_{ij} + \frac{5}{6} G_{ij} - C_{ij} \right) - \frac{2}{3} \delta_{ij} (P + \frac{5}{6} G - C) \right] \dots \dots \dots (38-3)$$

Where

$$C_2 = 0.60$$

$$P = \frac{1}{2}P_{kk}, G = \frac{1}{2}G_{kk} \text{ and } C = \frac{1}{2}C_{kk}$$

The wall-reflection term, $\phi_{ij,w}$ is responsible for the redistribution of normal stresses near the wall. It tends to damp the normal stress perpendicular to the wall, while enhancing the stresses parallel to the wall. This can be modeled as

$$\phi_{ij,w} \equiv C'_1 \left(\overline{u'_k u'_m} n_k n_m \delta_{ij} - \frac{3}{2} \overline{u'_l u'_k} n_j n_k - \frac{3}{2} \overline{u'_j u'_k} n_i n_k \right) \frac{C_l k^{3/2}}{\varepsilon d} + C'_2 \left(\phi_{km,2} n_k n_m \delta_{ij} - \frac{3}{2} \phi_{ik,2} n_j n_k - \frac{3}{2} \phi_{jk,2} n_i n_k \right) \frac{C_l k^{3/2}}{\varepsilon d} \dots\dots\dots(39-3)$$

Where:

$C'_1 = 0.5$, $C'_2 = 0.3$, n_k is the x_k component of the unit normal to the wall, d is the normal distance to the wall, and $C_l = C_\mu^{3/4} / \mathcal{K}$, $C_\mu = 0.09$ and \mathcal{K} is the von Karman constant ($\mathcal{K} = 0.4187$)

3.2.1.4.1 Flow re-modification to the linear pressure-strain model

“When the RSM is applied to near-wall flows using the enhanced wall treatment, the pressure-strain model must be modified. The modification used in ANSYS Fluent specifies the values of C_1 , C_2 , C'_1 and C'_2 as functions of the Reynolds stress invariants and the turbulent Reynolds number, according to the suggestion of Launder and Shima,” [45].

$$C_1 = 1 + 2.5AA_2^{0.25} \{1 - \exp[-(0.0067Re_t)^2]\}$$

$$C_2 = 0.75\sqrt{A}$$

$$C'_1 = -\frac{2}{3}C_1 + 1.67$$

$$C'_2 = \max \left[\frac{\frac{2}{3}C_2 - \frac{1}{6}}{C_2}, 0 \right]$$

With the turbulent Reynolds number defined as $Re_t = \rho k^2 / \mu \varepsilon$ the flatness parameter A and tensor invariants, A_2 and A_3 , are defined as

$$A = \left[1 - \frac{9}{8} (A_2 - A_3) \right]$$

$$A_2 = a_{ik} a_{ki}$$

$$A_3 = a_{ik} a_{kj} a_{ji}$$

$$a_{ij} = - \left[\frac{-\rho \overline{u'_i u'_j} + \frac{2}{3} \rho k \delta_{ij}}{\rho k} \right]$$

3.2.1.4.2 Quadratic pressure-strain model

“An optional pressure-strain model proposed by Speziale, Sarkar, and Gatski is provided in ANSYS Fluent. This model has been demonstrated to give superior performance in a range of basic shear flows, including plane strain, rotating plane shear, and axisymmetric expansion/contraction. This improved accuracy should be beneficial for a wide of complex engineering flows, particularly those with streamline curvature,”[45].

This model is written as follows:

$$\begin{aligned} \phi_{ij} = & -(C_1 \rho \varepsilon + C_1^* P) b_{ij} + C_2 \rho \varepsilon \left(b_{ik} b_{kj} - \frac{1}{3} b_{mn} b_{mn} \delta_{ij} \right) + (C_3 - C_3^* \sqrt{b_{ij} b_{ij}}) \rho k S_{ij} + \\ & C_4 \rho k \left(b_{ik} S_{jk} + b_{jk} S_{ik} - \frac{2}{3} b_{mn} S_{mn} \delta_{ij} \right) + C_5 \rho k (b_{ik} \Omega_{jk} + b_{jk} \Omega_{ik}) \dots \dots \dots (40-3) \end{aligned}$$

Where b_{ij} is the Reynolds-stress anisotropy tensor defined as

$$b_{ij} = \frac{-\rho \overline{u'_i u'_j} + \frac{2}{3} \rho k \delta_{ij}}{2 \rho k} \dots \dots \dots (41-3)$$

The main strain rate S_{ij} is defined as

$$S_{ij} = \frac{1}{2} \left(\frac{\partial u_j}{\partial x_i} + \frac{\partial u_i}{\partial x_j} \right) \dots \dots \dots (42-3)$$

The mean rate-of-rotation tensor Ω_{ij} is defined by

$$\Omega_{ij} = \frac{1}{2} \left(\frac{\partial u_i}{\partial x_j} + \frac{\partial u_j}{\partial x_i} \right) \dots \dots \dots (43-3)$$

The constants are

$$C_1 = 3.4, C_1^* = 1.8, C_2 = 4.2, C_3 = 0.8, C_3^* = 1.3, C_2 = 1.25, C_5 = 0.4$$

The quadratic pressure-strain model does not require a correction to account for the wall-reflection effect in order to obtain a satisfactory solution in the logarithmic region of a turbulent boundary.

3.3 Combustion modeling

“Combustion is one of the most important processes in engineering, which includes turbulent fluid flow, heat transfer, chemical reaction, radiative heat transfer and other complicated physical and chemical processes. In engineering applications which represent internal combustion engines, power station combustors, aero engines, gas turbine, boilers, furnaces and much other combustion equipment. It is important to be able to predict the flow, temperature, resulting species concentrations and emissions from various combustion systems for the design and improvement of combustion equipment.

CFD lends itself very well to the modeling of combustion. During combustion a fuel reacts with an oxidant stream to form products of combustion, the products are not usually formed in a single chemical reaction; the fuel components and the oxidant undergo a series of reaction,” [44].

The transport equations for the mass fraction m_i of each species i can be written by using the general transport equation

$$\frac{\partial}{\partial x} (\rho m_i) + \text{div}(\rho m_i) = \text{div}(\Gamma \text{grad } m_i) + S_i \dots \dots \dots (44-3)$$

The volumetric rate of generation (or destruction) of a species due to chemical reactions appears as source (or sink) term S_i in each of their transport equations.

3.3.1 Combustion models in Ansys Fluent

3.3.1.1 Generalized finite-rate model

Ansys Fluent predicts the local mass fraction of each species, Y_i through the solution of a convection-diffusion equation for i^{th} species. The general form of conservation equation can be written as below[47].

$$\frac{\partial}{\partial x}(\rho Y_i) + \nabla \cdot (\rho \vec{v} Y_i) = -\nabla \cdot \vec{J}_i + R_i + S_i \dots \dots \dots (45-3)$$

Where:

R_i is the net rate of production of species i by chemical reaction.

S_i is the rate of creation by addition from the dispersed phase plus any defined sources.

\vec{J}_i is the diffusion flux of species coefficient for i , which arises due to gradient of concentration and temperature.

In laminar flow, the mass diffusion, \vec{J}_i can be calculate from the following equation

$$\vec{J}_i = - \left[\rho D_{i,m} \nabla Y_i - D_{T,i} \frac{\nabla T}{T} \right] \dots \dots \dots (46-3)$$

$D_{i,m}$ is the mass diffusion coefficient for species i in the mixture, and $D_{T,i}$ is the thermal diffusion coefficient.

In turbulent flow

$$\vec{J}_i = - \left[\rho D_{i,m} + \frac{\mu_t}{Sc_t} \right] \nabla Y_i - D_{T,i} \frac{\nabla T}{T} \dots \dots \dots (47-3)$$

Where Sc_t is the turbulent Schmidt number and μ_t is the turbulent viscosity.

In the multi-component mixing flows, the transport of enthalpy due to species diffusion

$$\nabla \cdot \left[\sum_{i=1}^n h_i \vec{J}_i \right]$$

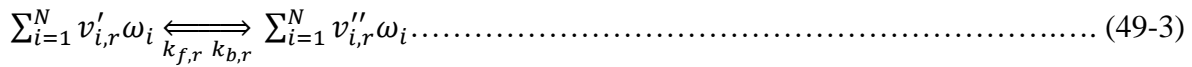
The reaction rates that appear as source term in the equation (45-3) are computed for turbulent flows by laminar finite model:

The source of chemical species i due to reaction is computed as the sum of the Arrhenius reaction sources over the N_R reactions.

$$R_i = M_{w,i} \sum_{r=1}^{N_R} \hat{R}_{i,r} \dots\dots\dots (48-3)$$

Where, $M_{w,i}$ is the molecular weight of species i and $\hat{R}_{i,r}$ is the Arrhenius molar rate of creation/destruction of species i in reaction r .

The general form of the r^{th} reaction can be written as follows:



Where,

N = number of chemical species in the system.

$v'_{i,r}$ = stoichiometric coefficient for reactant i in reaction r .

$v''_{i,r}$ = stoichiometric coefficient for product i in reaction r .

ω_i = symbol denoting species i

k_f = forward rate constant for reaction r .

k_b = backward rate constant for reaction r .

Equation (49-3) is valid for both reversible and non-reversible reactions. The molar rate of creation/destruction of species i in the r can be calculated as following:

For a reversible reaction

$$\hat{R}_{i,r} = \Gamma(v''_{i,r} - v'_{i,r}) \left(k_{f,r} \prod_{j=1}^N [C_{j,r}]^{\eta'_{j,r}} - k_{b,r} \prod_{j=1}^N [C_{j,r}]^{v''_{j,r}} \right) \dots\dots\dots (50-3)$$

And for non-reversible reaction is given by

$$\hat{R}_{i,r} = \Gamma(v''_{i,r} - v'_{i,r}) \left(k_{f,r} \prod_{j=1}^N [C_{j,r}]^{\eta'_{j,r} + \eta''_{j,r}} - k_{b,r} \prod_{j=1}^N [C_{j,r}]^{v''_{j,r}} \right) \dots\dots\dots (51-3)$$

Where,

$C_{j,r}$ = molar concentration of species j in reaction r

$\eta'_{j,r}$ = rate exponent for reactant species j in reaction r

$\eta''_{j,r}$ = rate exponent for product species j in reaction r

Γ = the net effect of third bodies on the reaction rate, which given by

$$\Gamma = \sum_j^N \gamma_{j,r} C_j \dots \dots \dots (52-3)$$

Where,

$\gamma_{j,r}$ is the third-body efficiency of the j^{th} species in the r^{th} reaction.

The forward rate constant for reaction r ($k_{f,r}$) is computed using the Arrhenius expression

$$k_{f,r} = A_r T^{\beta_r} e^{-E_r/RT} \dots \dots \dots (53-3)$$

Where,

A_r = pre-exponential factor

β_r = Temperature exponent

E_r = activation energy for the reaction (J/kmol)

R = universal gas constant (J/kmol-K)

If the reaction is reversible, the backward rate constant for reaction r , $k_{b,r}$ is computed by

$$k_{b,r} = \frac{k_{f,r}}{K_r} \dots \dots \dots (54-3)$$

Where, K_r is the equilibrium constant for the r^{th} reaction, which can be calculated by:

$$K_r = \exp\left(\frac{\Delta S_r}{R} - \frac{\Delta H_r}{RT}\right) \left(\frac{P_{atm}}{RT}\right)^{\sum_{i=1}^N (v''_{i,r} - v'_{i,r})} \dots \dots \dots (55-3)$$

The term within the exponential function represents the change in Gibbs free energy, and its components are computed as follows:

$$\frac{\Delta S_r}{R} = \sum_{i=1}^N (v''_{i,r} - v'_{i,r}) \frac{S_i}{R} \dots \dots \dots (56-3)$$

$$\frac{\Delta H_r}{RT} = \sum_{i=1}^N (v''_{i,r} - v'_{i,r}) \frac{h_i}{RT} \dots \dots \dots (57-3)$$

Where S_i and h_i are the entropy and enthalpy of the i^{th} species.

3.3.1.2 Eddy-dissipation model

“Reaction rates are assumed to be controlled by the turbulence, so expensive Arrhenius chemical kinetic calculation can be avoided. Ansys Fluent provides a turbulence-chemistry interaction model, based in the work of Magnussen and Hjertager called the eddy-dissipation model,” [47].

The net rate of production of species i due to reaction r , $R_{i,r}$ is given by the smaller of the two equations below:

$$R_{i,r} = v'_{i,j} M_{w,i} A \rho \frac{\varepsilon}{k} \min_R \left(\frac{Y_R}{v'_{i,r} M_{w,R}} \right) \dots \dots \dots (58-3)$$

$$R_{i,r} = v'_{i,j} M_{w,i} A B \rho \frac{\varepsilon}{k} \left(\frac{\sum_P Y_P}{\sum_j^N v'_{j,r} M_{w,j}} \right) \dots \dots \dots (59-3)$$

Where

Y_p is the mass fraction of any product species, P

Y_R is the mass fraction of a particular reactant, R

A is an empirical constant equal to 4.0

B is an empirical constant equal to 5.0

ε is the turbulent dissipation rate ($m^2 s^{-3}$)

k is the turbulent kinetic energy per unit mass (J/kg)

“In premixed flames, the reactants will burn as soon as they enter the computational domain, upstream of the flam stabilizer. To remedy this, fluent provides the finite-rate/eddy-dissipation mode, where both the Arrhenius, Eq (50-3), and eddy dissipation, Equations (58-3) and (59-3) reaction rates are calculated. The net reaction rate is taken as the minimum of these two rates. In practice, the Arrhenius rates as a kinetic switch, preventing reaction before the flame holder. Once the flame is ignited, the eddy-dissipation rate is generally smaller than the Arrhenius rates, and reaction are mixed-limited.

The eddy-dissipation model requires products to initiate reaction. When the solution is initialized for steady flows, fluent sets all species mass fractions to a maximum of the user specified initial value and 0.01. This is usually sufficient to start the reaction. However, if a mixing solution converges first, where all product mass fractions are zero, there may be a need to patch products into the reaction zone to ignite the flame,” [45].

3.3.1.3 Eddy-dissipation-concept (EDC) model:

“The eddy-dissipation-concept (EDC) model is an extension of the eddy-dissipation model to include detailed chemical mechanisms in turbulent flows. It assumes that reaction occurs in small turbulent structures, called the fine scales. The length fraction of the fine scales is modeled as

$$\xi^* = C_\xi \left(\frac{\nu_\epsilon}{k^2}\right)^{1/4} \dots\dots\dots(60-$$

3)

Where,

* denotes fine-scale quantities

C_ξ = volume fraction constant = 2.1377

ν = kinematic viscosity.

The volume fraction of the fine scales is calculated as $(\xi^*)^3$. Species are assumed to react in the fine structures over a time scale

$$\tau^* = C_\tau \left(\frac{\nu}{\epsilon}\right)^{1/2} \dots\dots\dots(61-3)$$

Where, C_τ is a time scale constant equal to 0.4082.

In Ansys Fluent, combustion at the fine scales is assumed to occur as a constant pressure reactor, with initial conditions taken as the current species and temperature in the cell. Reactions proceed over the time scale τ^* , governed by the Arrhenius rates of Equation (50-3), and are integrated numerically using the ISAT algorithm. ISAT can accelerate the

chemistry calculations by two to three orders of magnitude, offering substantial reductions in run-times,” [47].

The source term in the conservation equation for the mean species i is modeled as

$$R_i = \frac{\rho(\xi^*)^2}{\tau^*(1-(\xi^*)^2)} (Y_i^* - Y_i) \dots\dots\dots(62-3)$$

Where, Y_i^* is the fine-scale species mass fraction after reacting over the time τ^* .

3.3.2 Premixed Combustion Modeling

“Premixed combustion is much more difficult to model than non-premixed combustion, the reason for this is that premixed combustion usually occurs as a thin, propagating flame that is stretched and contorted by turbulence. For subsonic flows, the overall rate of propagation of the flame is determined by both the laminar flame speed and the turbulent eddies. The laminar flame speed is determined by the rate that species and heat diffuse upstream into the reactants and burn.

The turbulent premixed combustion model, involves the solution of a transport equation for the reaction progress variable. The closure of this equation is based on the definition of the turbulent flame speed,” [45].

3.3.2.1 Propagation of the Flame Front

The flame front propagation is modeled by solving a transport equation for the density-weighted mean reaction progress variable, denoted by \bar{c} :

$$\frac{\partial y}{\partial t} (\rho \bar{c}) + \nabla \cdot (\rho \vec{v} \bar{c}) = \nabla \cdot \left(\frac{u_t}{Sc_t} \nabla \bar{c} \right) + \rho Sc \dots\dots\dots(63-3)$$

Where

\bar{c} = mean reaction progress variable

Sc_t = turbulent Schmidt number

Sc = reaction progress source

The progress variable is defined as a normalized sum of the product species mass fraction

$$c = \frac{\sum_k a_k (Y_k - Y_k^u)}{\sum_k a_k Y_k^{eq}} = \frac{Y_c}{Y_c^{eq}} \dots\dots\dots(64-3)$$

Where:

Superscript u denotes the unburnt reactant

Y_k denotes the k^{th} species mass fraction

Superscript eq denotes chemical equilibrium

a_k are constants that are typical zero for reactants and unity for a few product species .

Based on this definition, $c = 0$ where the mixture is unburnt and $c = 1$ where the mixture is burnt

The mean reaction rate in equation (63-3) is modeled as

$$\rho S_c = \rho_u U_t |\nabla c|$$

Where:

ρ_u density of unburnt mixture

U_t turbulent flame speed

The turbulent flame speed is computed using a model of wrinkled and thickened flame fronts:

$$U_t = A(u')^{3/4} U_l^{1/2} \alpha^{-1/4} l_t^{1/4} = Au' \left(\frac{\tau_t}{\tau_c} \right)^{1/4} \dots\dots\dots(65-3)$$

Where:

A = model constant

u' = RMS (root-mean-square) velocity

U_l = laminar flame speed

$\alpha = k/\rho c_p$ = molecular heat transfer coefficient of unburnt mixture (unburnt thermal diffusivity)

l_t = turbulence length scale

$\tau_t = l_t/u'$ = turbulence time scale

$\tau_c = \alpha/U_l^2$ = chemical time scale.

The turbulence length scale (l_t) is computed from

$$l_t = C_D \frac{(u')^3}{\varepsilon}$$

Where: ε is the turbulence dissipation rate.

“The model is based on the assumption of equilibrium small-scale turbulence inside the laminar flame, resulting in a turbulent flame speed expression that is purely in terms of the large-scale turbulent parameters. The default values of 0.52 for A, 0.37 for Cd are recommended, and are suitable for most premixed flames.

Non-adiabatic premixed combustion model is considered. The energy transport equation is solved in order to account for any heat losses or gains within the system. These losses/gains may include heat sources due to chemical reaction or radiation heat losses,”[45].

The energy equation in terms of sensible enthalpy, h, for the fully premixed fuel is as follows:

$$\frac{\partial}{\partial t}(\rho h) + \nabla \cdot (\rho \vec{v} h) = \nabla \cdot \left[\frac{k+k_t}{c_p} \nabla h \right] + S_{h,chem} + S_{h,rad} \dots \dots \dots (66-3)$$

$S_{h,rad}$ represents the heat losses due to radiation and $S_{h,chem}$ represents the heat gains due to chemical reaction:

$$S_{h,chem} = \rho S_c H_{comb} Y_{fuel} \dots \dots \dots (67-3)$$

Where:

S_c = normalized average rate of product formation (s⁻¹)

H_{comb} = heat of combustion for burning 1 kg of fuel (J/kg)

Y_{fuel} = fuel mass fraction of unburnt mixture

3.3.3 Partially Premixed Combustion Modeling

“The partially premixed model in FLUENT is a simple combination of the non-premixed model and the premixed model. The premixed reaction-progress variable, c, determines the position of the flame front. Behind the flame front (c = 1), the mixture is burnt and the

equilibrium or laminar flamelet mixture fraction solution is used. Ahead of the flame front ($c = 0$), the species mass fractions, temperature, and density are calculated from the mixed but unburnt mixture fraction. Within the flame ($0 < c < 1$), a linear combination of the unburnt and burnt mixtures is used,” [45].

3.4 NO_x modeling

“In this simulation the prediction of NO_x has been calculated including both thermal and prompt NO_x. Ansys Fluent solves the mass transport equation for the species, taking into account convection, diffusion, production, and consumption of related species. This approach is completely general, being derived from the fundamental principle of mass conservation. The effect of residence time in mechanisms (the Lagrangian reference frame concept) is included through the convection terms in the governing equations written in the Eulerian reference frame,”[45].

For thermal and prompt mechanisms, only the species transport equation is needed

$$\frac{\partial}{\partial x}(\rho Y_{NO}) + \nabla \cdot [\rho \vec{v} Y_{NO}] = \nabla \cdot [\rho \mathcal{D} Y_{NO}] + U_{NO} \dots\dots\dots(68-3)$$

Where: \mathcal{D} is the effective diffusion coefficient and U_{NO} is the source term.

The NO source term due to NO_x thermal mechanisms is

$$U_{thermal,NO} = M_{w,NO} \frac{d[NO]}{dt} \dots\dots\dots(69-3)$$

The prompt NO_x formation rate

$$\frac{d[NO]}{dt} = f k'_{pr} [O_2]^a [N_2] [FUEL] e^{(E'_a/R_u T)} \dots\dots\dots(70-3)$$

In the above equation,

$$f = 4.75 + 0.0819n - 23.2\phi + 32\phi^2 - 12.2\phi^3 \dots\dots\dots (71-3)$$

$$k'_{pr} = 6.4 \cdot 10^6 \left(\frac{R_u T}{P} \right)^{a+1} \dots\dots\dots(72-3)$$

Where: n is the number of carbon atoms per molecule for the hydrocarbon fuel and a is the oxygen reaction order. The correction factor is a curve fit for experimental data, valid for aliphatic alkane hydrocarbon fuels ($C_n H_{2n+2}$) and for equivalence ratios between 0.6 and 1.6 [45].

CHAPTER 4

4 COMBUSTOR MODELING AND SETUP

4.1 COMBUSTOR AND MIXER DESCRIPTION

This chapter depicts the work implemented in this research study. A purpose-built laboratory microturbine combustor, made of steel, set up vertically, has been used for this study. The combustor consists of three main parts:

- 1- A combustor.
- 2- A variable-length centerbody.
- 3- A swirler.

The axially mounted mixing chamber consist of an annular mixing tube with axial air flow and six gas fuel injection in the cross flow to the mixing chamber axis. An axial flat-vane swirlers is mounted in the annular tube. Three swirlers with different vane angles of 30, 45, and 60 deg. To maintain similar flow conditions, a 0 deg vane angle swirler was used as well. The mixer has six nozzles each one has a diameter of 10.5 mm to supply the air inside the mixer, also it has six fuel nozzle with a diameter of 0.7mm. The centerboard diameter was 25mm, while the combustor inner diameter was 66mm and the length was 104mm. the maximum length of the centerbody was 66mm. The center body and combustion chamber were cooled to keep the temperature of the surfaces around 50°C. In the all cases of study, the nominal power of $P_0 = 8.1\text{kW}$. And the nominal atmospheric conditions were a pressure of 101.3 kPa and a temperature of 20°C. All calculation parameters and the numerical description of the combustor are described.

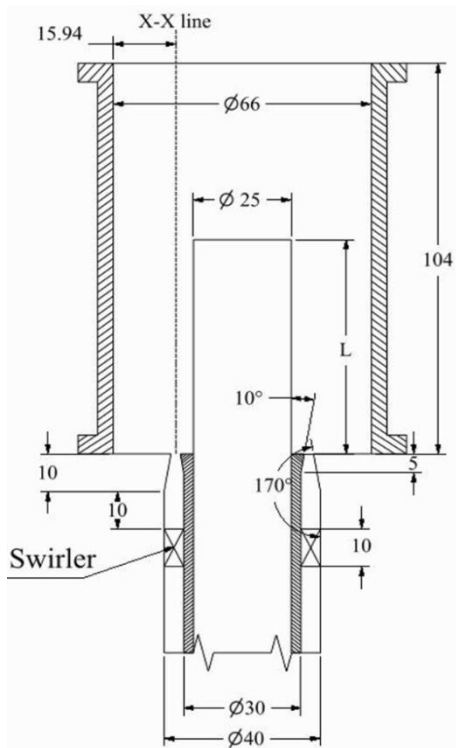


Figure 4-1 Schematics of mixing section and combustor.

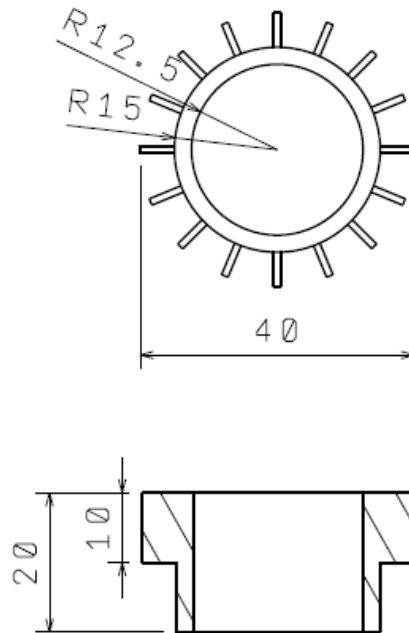


Figure 4-2 cross section of swirler.

The CFD simulation implemented in this research study for the combustor perform based on experimental research done by [40].

4.2 EXPERIMENT - DESCRIPTION

During the experimental research carried out by [40], the effect of the combustor type , equivalence ratio, swirl number, and power on NO_x and CO emissions of a purposely built, lean-premixed laboratory-scale model combustor with water-cooled walls and centerbody, which simple geometry simulates combustors found in micro gas turbine. Air and gaseous propane were used as fuel mixture. The tests have been performed at atmospheric conditions. The effect of influential parameters on the emissions and the heat transfer to the combustor walls and the centerbody, the following independent variables were systematically varied.

- 1- Combustor type, nominally defined by the normalized centerbody length L/L_0 (tubular combustor corresponds to $L/L_0 = 0$, an annular combustor corresponds to $L/L_0 = 1$,
- 2- Swirl number $S = 0, 0.45, 0.73$, and 1.13 .
- 3- Normalized power $P/P_0 = 0.36, 0.56, 0.78$, and 1 .
- 4- Equivalence ratio range $\phi = 0.6 - 0.95$

The central body was varied to $\frac{1}{3}$ and $\frac{2}{3}$ of the full length, thus making a hybrid tubo-annular combustor to enable better understanding of gradual change from one combustor type to the other. In addition, the other basic variables, such as equivalence ratio, swirl number, and power, were systematically varied, which resulted in a library of connected data.

The fuel-air mixture is prepared in a mixing chamber and injected through a swirler into the combustor. The tests were performed at atmospheric conditions: pressure of 101.3 kPa and temperature of 20°C. The tests were performed under parametric variations of equivalence ratio, swirl number and thermal power. The fuel and air flow rates were measured using calibrated rotameters, while the exhaust gas composition was measured using Testo 350-XL and Testo 454 flue gas analyzers. To get representative flue gas samples and to prevent the outer air from interfering with exhaust gases, an extension tube with the same inner diameter and length as the combustor was attached to the combustor exit. The exhaust gas was sampled with a cooled stainless steel probe and transported through a heated tube to the gas analyzer. The accuracy of measurements is $\pm 0.2\%$ for O₂ and $\pm 5\%$ of reading for NO. The measured values of NO were corrected to 15% O₂ flue gas dry conditions.

4.3 NUMERICAL SETUP AND BOUNDARY CONDITIONS

In this study, simulations were carried out using Ansys-Fluent 16.0 CFD software. The mass and momentum Reynolds-averaged equations are used to solve the turbulent steady flow. Closure for the Reynolds stress terms in the momentum equations was performed via the Realizable k- ϵ turbulence model, which is a variant of the Standard k- ϵ turbulence model. The Enhance Wall Treatment was used with Realizable k- ϵ turbulence model.

The Finite Rate/Eddy Dissipation Mode is used to address the turbulence-chemical reaction. Radiation from the gas constituted a significant portion of the heat transfer between the gas and combustor wall. The P_1 radiation model is chosen in this study in order to avoid the high computing costs.

The boundary conditions were as follows: The mass flow rate of basic fuel was 0.175 g/s as shown in table 4-1, which corresponds to thermal power of 8.1 kW. The radiation model is chosen to be (P_1) model. The fluid mixture density is calculated by using the ideal law. The specific heat, viscosity, and the thermal conductivity of the fluid mixture are calculated using the mass weighted average method. Second-order upwind scheme is used to discretize the governing equations, and the second order the solution convergence is assumed when all of residuals parameters fall below 10^{-6} . The SIMPLE algorithm is used to deal with pressure-velocity coupling. The surface temperature of central body and combustion chamber was constant at 50°C. The combustor outlet pressure was assumed 101.3 kPa and the outlet temperature 200°C. The flow is steady. As oxidant, air is used and it comprises a mixture of 23% mass O_2 and 77% mass N_2 .

4.4 COMBUSTOR MODELING

Generally, to implement CFD simulation, the first and important step is the preparation of the model (drawing and meshing), specifying the flow domain of the physical system, this allows to apply and solve the governing equations in the domain, however, the accuracy of the final solution depends on choosing the grid type, the method of constructing the mesh, and the number of cells. As a number of nodes is higher, the accuracy of final solution also is higher. On the other hand, the cost of the calculation (processing time) is higher. So, it is important for the model to choose a suitable mesh which gives conversion and a good result of the final solution with a reasonable calculation time, especially for complex models. In these cases, the independency of the mesh must be repeated several times until reaching the optimum mesh.

In this study, the model was split into two connected parts (two domains); the mixing zone and the combustion zone. The mixing zone represents the flow field in the system as shown

in figure 4-1, in this zone the air and fuel are mixed together and the swirl flow is produced by using a swirler closed to the outlet of mixer, however, during the calculation, there is no any combustion process occurs in mixing zone. The numerical simulation carried out in this zone by using four different angles of the swirler (0° , 30° , 45° , 60°). The second zone describes the flow field in the combustion chamber as shown in figure 4-1, in this zone combustion process occur within in the normal combustion conditions and performed by a mixture of propane and hydrogen as fuel with two volumetric fractions of hydrogen $X_{H_2} = 0\%$ and $X_{H_2} = 10\%$, and four regimes of $\phi = 0.6, 0.7, 0.8,$ and 0.9 .

Catia P3V5R21 was used for constructing the geometry of the model. A three dimensional model was used for simulation; this 3D geometry was split into two parts (mixing part and combustor part). The two domains were meshed using commercial software ANSYS16, and due to the symmetry of the model, only half of the mixing zone and half of the combustion chamber zone are considered, which results in the decrease of calculation time.

4.4.1 Mixing chamber meshing

The mixing chamber zone was meshed by the tetrahedral mesh; the main problem with this model was constructing the mesh for the swirler zone. Hence a mixed mesh was used, but mainly tetrahedral mesh of the mixing domain, which can lead to a higher number of elements generated and results in longer computation times. As one can see in figure 4-3, to get a more detailed for mixing chamber mesh, it is preferred to summarize the details in table 4-1.

Table 4-1 Details of mixing chamber computational mesh

	Grid details	
1	Number of nodes	1168974
2	Number of elements	3233594
3	Relevance	100
4	Smoothing	Fine
5	Use advance function	Proximity and curvature
6	Curvature normal angle	12.0°
6	Minimum size	$1.4912 * 10^{-5}m$
7	Maximum size	$2.9824 * 10^{-3}m$
8	Maximum face size	$1.4912 * 10^{-3}m$
9	Minimum edge length	$3.7136 * 10^{-4}m$
10	Elements size	$0.7 * 10^{-4}m$
11	Inner inflation layers	12 (smooth transition)
12	Outer inflation layers	12 (smooth transition)
13	Growth rate for inner and Outer inflations	1

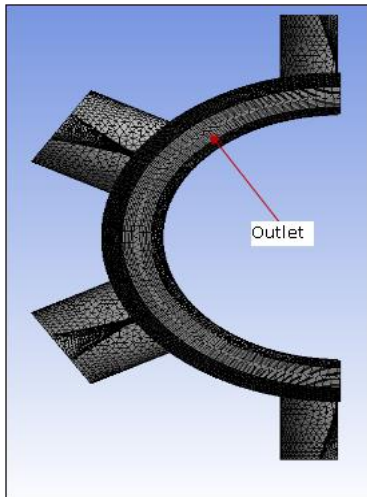
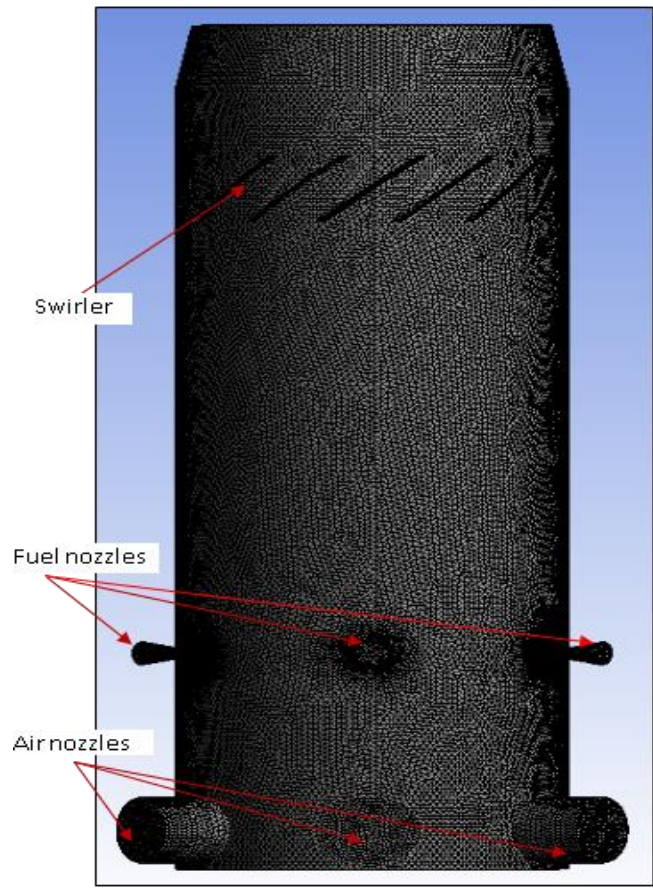


Figure 4-3 Computational mesh for mixer chamber.

4.4.2 Combustion chamber meshing

A hexahedral mesh was used to mesh the Combustion chamber zone, which can give faster and stable so it prefer to be used more than tetrahedral mesh. As can see in figure 4-4, to get a more detailed for Combustion chamber mesh, it is preferred to summarize the details in table 4-2

Table 4-2 details for combustor chamber computational mesh

	Grid details	
1	Number of nodes	2372309
2	Number of elements	2328120
3	Relevance	80
4	Smoothing	Fine
5	Use advance size function	curvature
6	Relevance center size function	Coarse
7	Minimum size	$6.9653 * 10^{-5}m$
8	Maximum face size	$1.3931 * 10^{-3}m$
9	Maximum size	$6.9653 * 10^{-3}m$
10	Elements size	$7 * 10^{-4}m$
11	Method	Multi zone (hexahedral mesh)
12	Sweep element size	$5.9 * 10^{-4}m$
13	Surface mesh method	Uniform
14	First layer thickness of inflation	$2 * 10^{-4}m$
15	Maximum number of layers	18
16	Growth rate	1

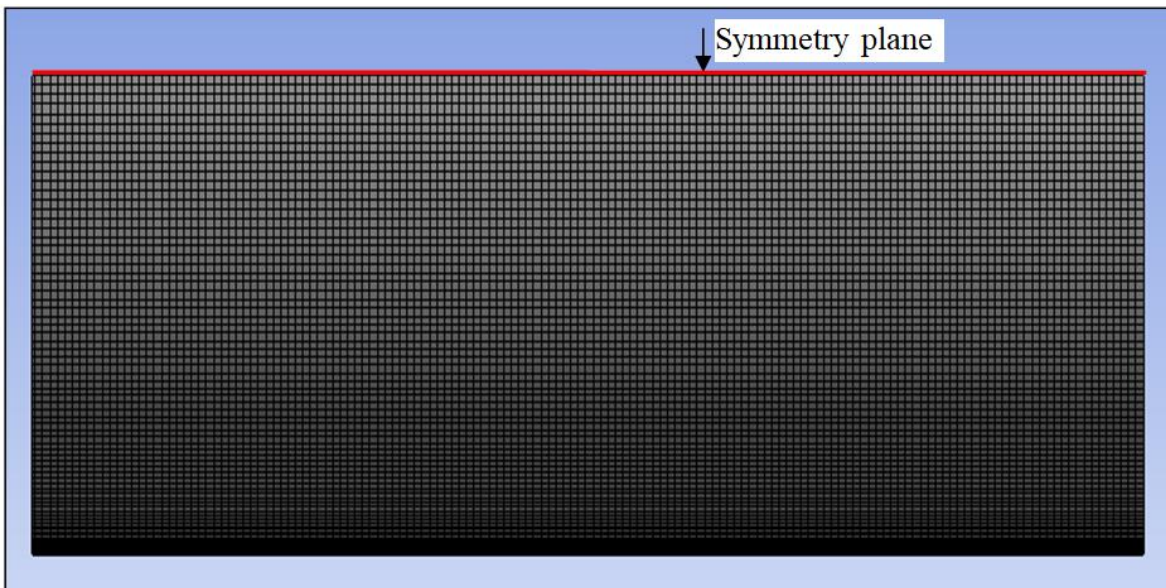
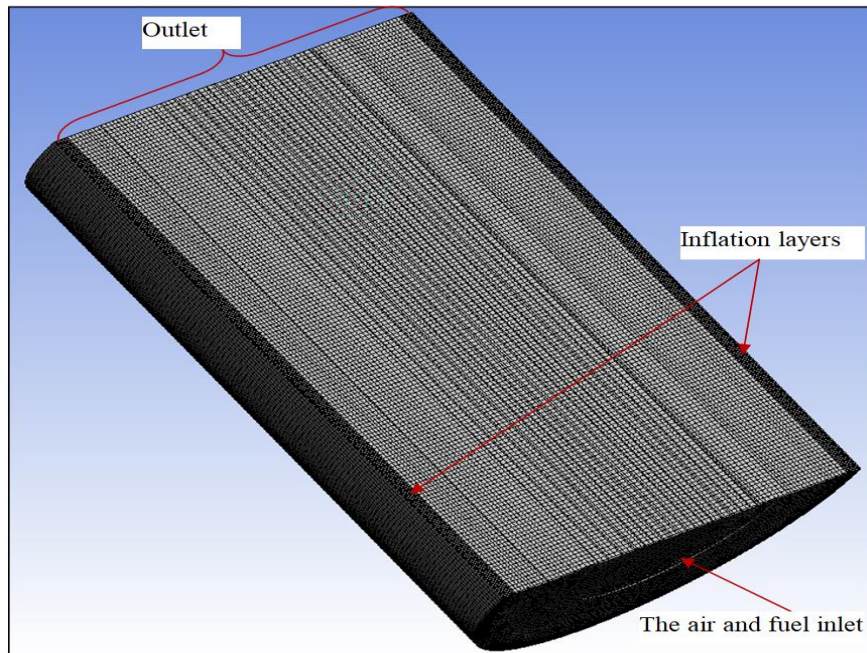


Figure 4-4 Computational mesh for combustor chamber

4.4.3 Independency of grid Quality for mixer (grid sensitivity solutions)

It is important to check the mesh quality to ensure good quality results, so a grid independency test to assess the computational mesh solution convergence and its solution

dependency has been conducted for six different computational grids are designed, as presented in table 4-4. The difference in these six meshes is mainly due to different mesh resolution requirements to reach a higher resolution in the premixing chamber zone. To improve near wall grid resolution, inflation layers were applied in the six meshes. Because the grid influence upon the results, the mixing flow has to be solved via a sensitivity analysis using the four meshes.

A grid convergence study was conducted for the six meshes shown in table 4-3. This analysis was done by simulating the flow in the mixing zone for the case of ($H_2\% = 0.75$, $\phi = 0.8$, swirl number = 0.45) using the realizable $k - \varepsilon$ model with an Enhanced wall treatment.

It can be observed from figures 4-5, 4-6, 4-7 and 4-8 the comparison of mean velocity and its components profiles at a line passing the outlet of the mixing zone, these velocities have calculated by the six different meshes in table 4-4

Table 4-3 Details of proposal computational mesh for mixer chamber.

Grid details	Mesh-1	Mesh-2	Mesh-3	Mesh-4	Mesh-5	Mesh-6
Relevance	40	65	80	100	100	100
Use advanced size function	Proximity & curvature	Proximity-curvature	Proximity-curvature	Proximity-curvature	Proximity-curvature	Proximity-curvature
Body sizing	-	-	-	-	0.8 mm	0.65 mm
Min. size	1.8378 $* 10^{-5}m$	1.676 $* 10^{-5}m$	1.5915 $* 10^{-5}m$	1.4912 $* 10^{-5}m$	1.4912 $* 10^{-5}m$	1.4912 $* 10^{-5}m$
Max. size	3.6774 $* 10^{-3}m$	3.3519 $* 10^{-3}m$	3.1829 $* 10^{-3}m$	2.9824 $* 10^{-3}m$	2.9824 $* 10^{-3}m$	1.4912 $* 10^{-5}m$
Max. face size	1.8378 $* 10^{-3}m$	1.676 $* 10^{-3}m$	1.5915 $* 10^{-3}m$	1.4912 $* 10^{-3}m$	1.4912 $* 10^{-3}m$	1.4912 $* 10^{-3}m$
Outer side	-	3 layers	5 layers	8 layers	12 layers	16 layers

wall inflation						
inner side wall inflation	-	3 layers	5 layers	8 layers	12 layers	16 layers
Number of nodes	131113	312082	562796	828860	1168974	1417524
Number of elements	655498	1214898	1999720	2649700	3233594	3818361

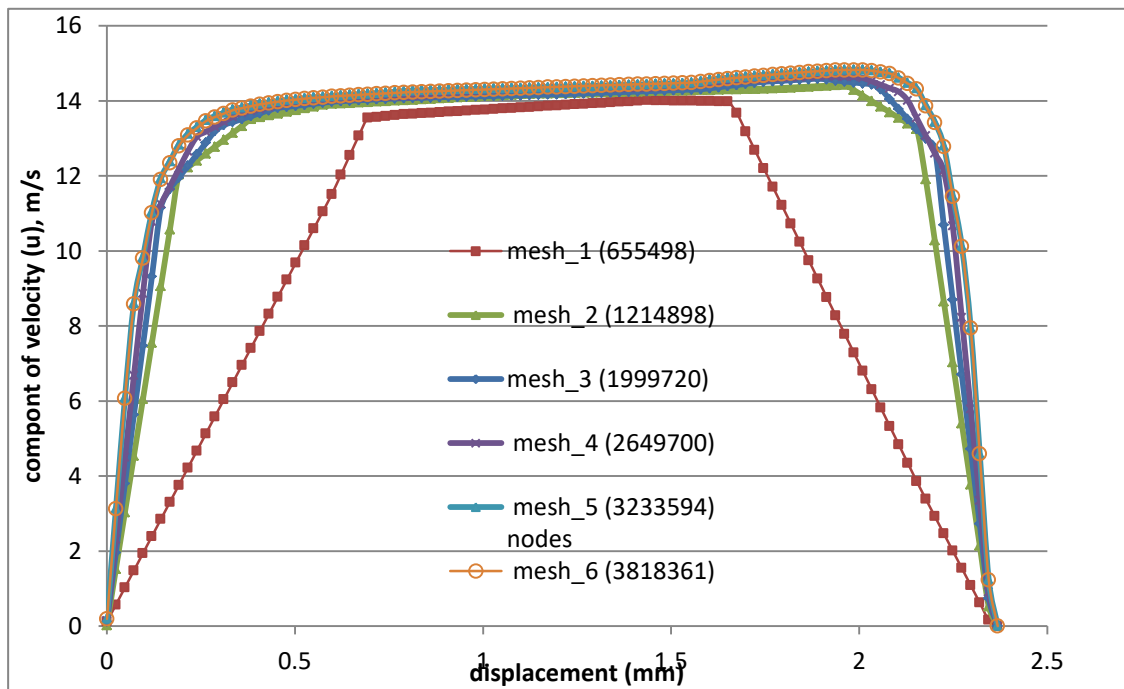


Figure 4-5 Grid sensitivity solutions of the component velocity (u).

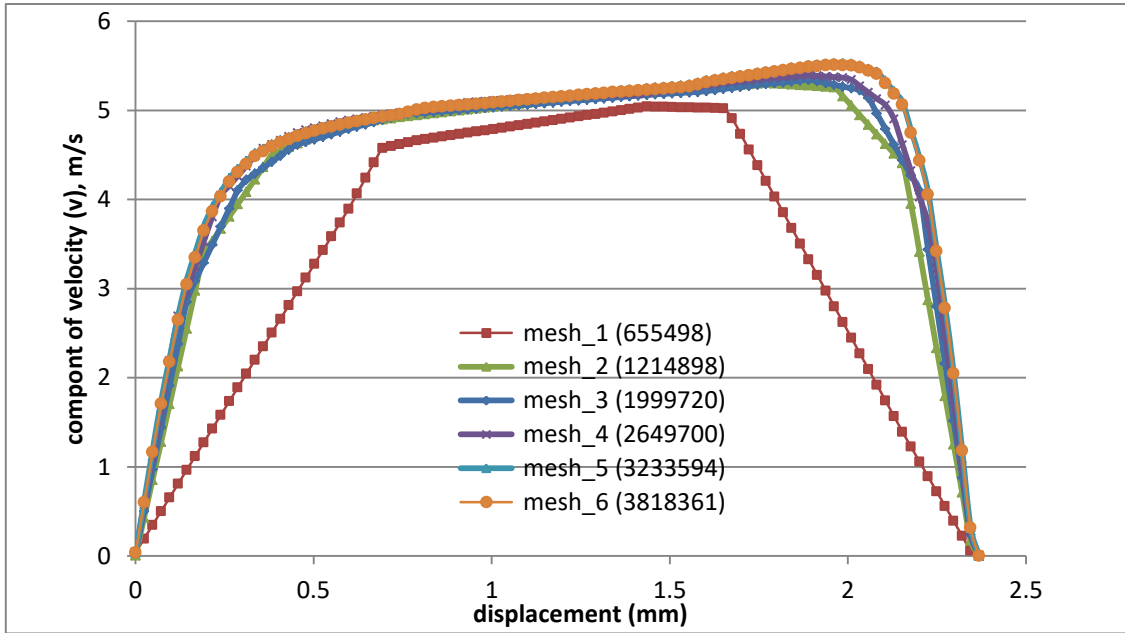


Figure 4-6 Grid sensitivity solutions of the component velocity (v).

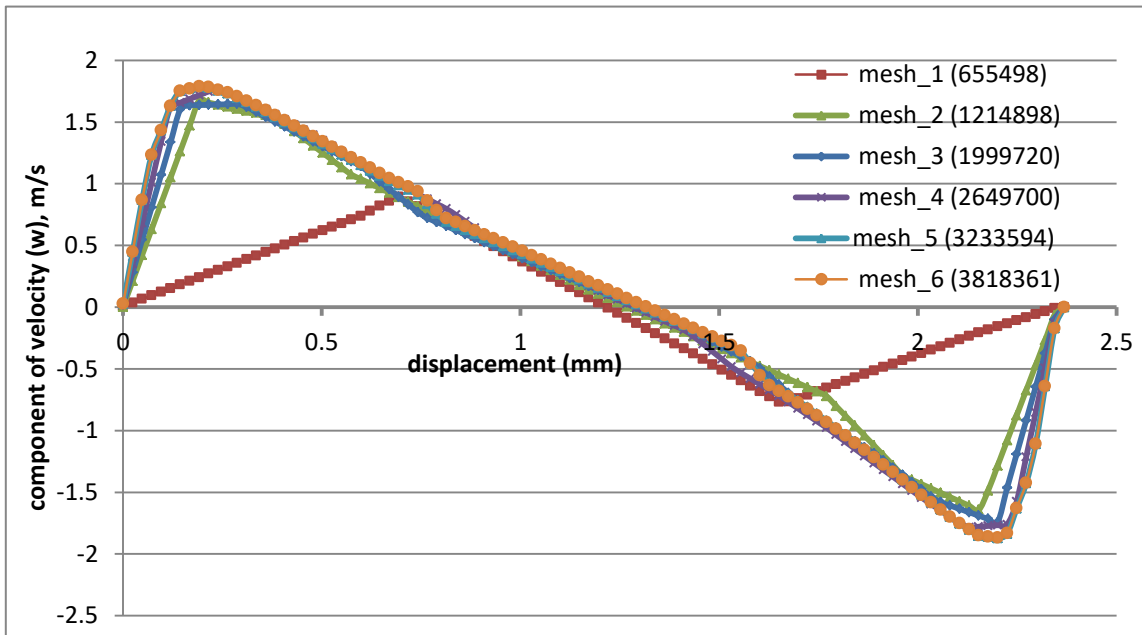


Figure 4-7 Grid sensitivity solutions of the component velocity (w).

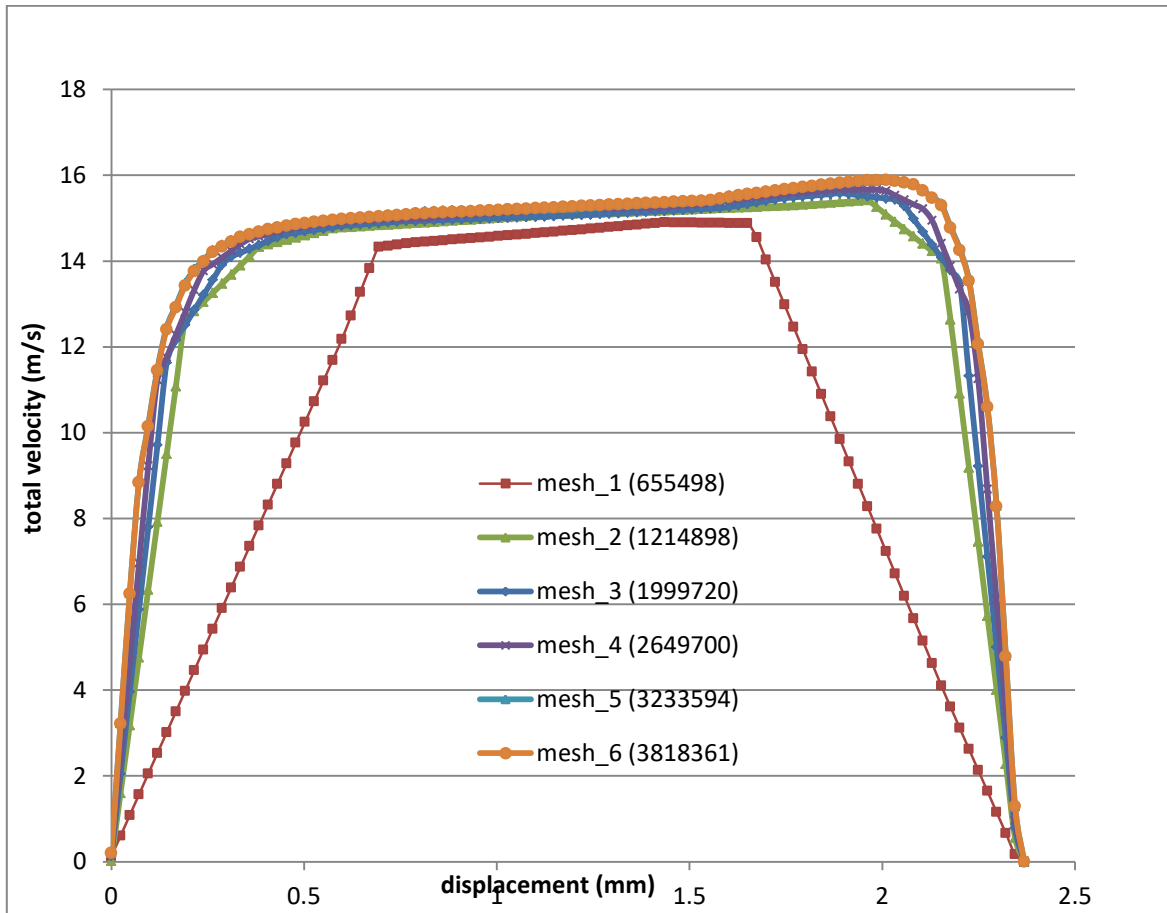


Figure 4-8 Grid sensitivity solutions of the total velocity.

A grid convergence study is conducted for six meshes as shown in the table 4-4, a comparison of mean velocity and its components along a line passing the outlet of the mixture are presented in figures 4-5, 4-6, 4-7 and 4-8. It can be seen that the profiles of velocity (U) which calculated by using meshes 1, 2, 3 and 4 have a gradual different trends compared to the profiles which calculated by using meshes 5 and 6, this is very clear nearby the wall. For example, the mesh 1 underestimates the velocity near the wall ($0 < x < 0.8$) compared to the other meshes. This under estimates is reduced with enhancing the mesh (2, 3, 4, 5 and 6), so the profiles of mesh 5 and mesh 6 present exactly the same trends at each location. Increasing the nodes number does not have any advantage, in addition, increases the calculation time and causes convergence difficulties; thus, it makes

the numerical modeling more expensive. Since the mesh 6 gives the same results as the mesh5 and to reduce the computational time, the mesh 5 is chosen for calculations in the present study.

And also, the profiles of radial and vertical velocity were checked by using the six meshes as shown in figures 4-6 and figures 4-7.

4.4.4 Independency of grid Quality for combustion

A grid independency test to assess the computational mesh solution convergence and its solution dependency has been conducted for five meshes as shown in table 4-4.

Table 4-4 Details of proposal computational mesh for combustion chamber.

Grid details	Mesh-1	Mesh-2	Mesh-3	Mesh-4	Mesh-5
Relevance	-	30	60	80	100
Use advanced size function	curvature	curvature	curvature	curvature	curvature
Min. size	6.9653 $* 10^{-5}m$				
Max. size	1.3931 $* 10^{-3}m$				
Max. face size	6.9653 $* 10^{-3}m$				
Wall inflation	-	8 layers	12 layers	18 layers	20 layers
Number of nodes	57132	344697	801728	2372309	3246364
Number of elements	53205	332896	781123	2328120	3203526
Min. zone sweep element size	$2 * 10^{-2}m$	1.2 $* 10^{-3}m$	$9 * 10^{-4}m$	5.9 $* 10^{-4}m$	$3 * 10^{-4}m$

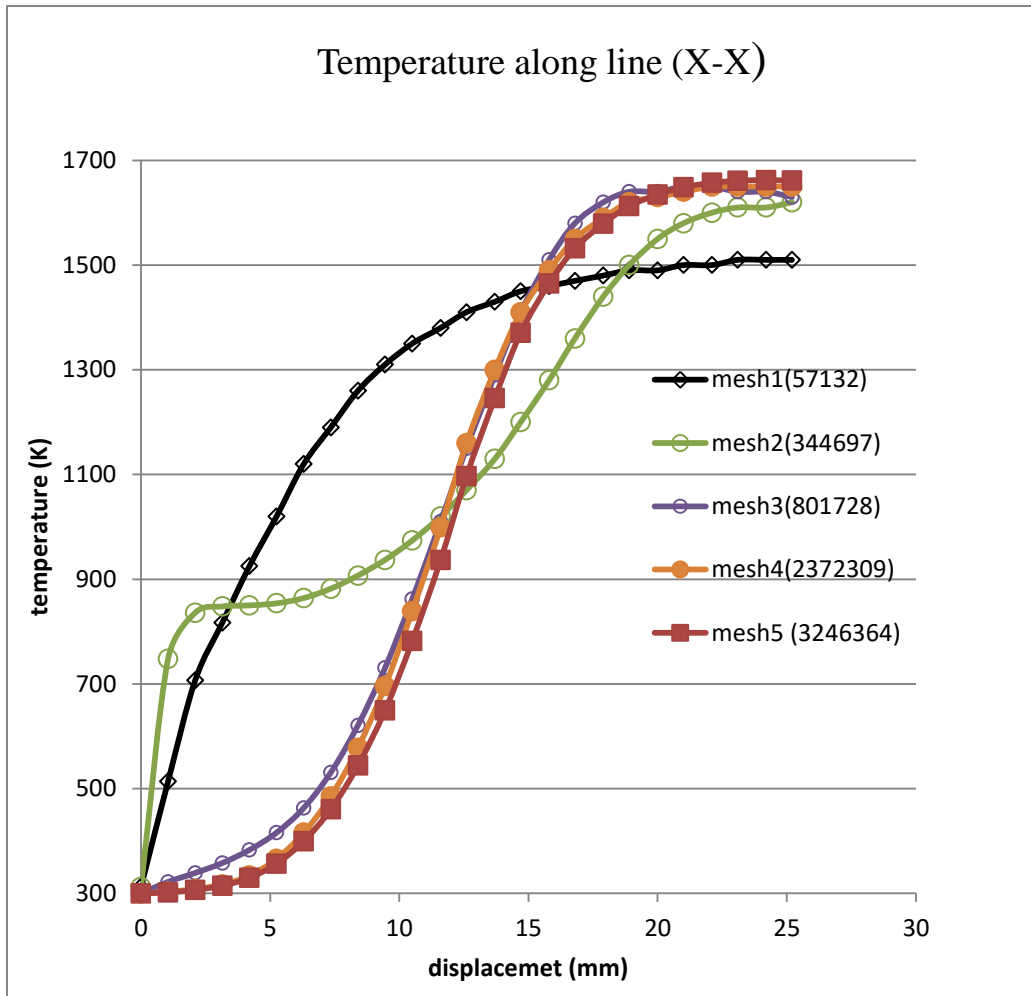


Figure 4-9 Grid sensitivity solutions of the temperature.

Figure 4-9 shows a comparison of predicted temperature profiles in the (X-X) line locations of combustion chamber, these predicted temperature profiles calculated by using five different type of meshes. The difference in these five meshes is mainly due to different grid resolution requirements to have a higher resolution in the combustion chamber. Because the grid influence upon the results, the reacting flow has to be solved via a sensitivity analysis using the five meshes.

As show in figure 4-9, the predicted temperature profiles, calculated by using mesh (1) and mesh (2) are very poorly estimates, this due to the two profiles describe the different tends.

For example, in rang of $3.5\text{mm} < x < 20\text{mm}$ the mesh (1) overestimates the predicted profile of temperature. In addition, it underestimates the predicted temperature on two ranges of the line (X-X) which are $x < 3.5 \text{ mm}$ and $x > 20\text{mm}$.

In case of meshes (4) and mesh (5), the predicted temperature profiles present exactly the same tends at each location. Increasing the nodes number does not have any advantage, in addition, increases the calculation time and causes convergence difficulties; thus, it makes the numerical modeling more expensive. Since the mesh (4) gives the same results as the mesh (5) and to reduce the calculation cost (computational time), the mesh (4) is chosen for all calculations of combustion chamber in the present study.

Chapter 5

5 RESULTS

5.1 Validation of predicted results with experimental data

For validation of the applied numerical analysis, results of experimental investigation of the micro gas turbine combustor, fueled by propane, are used [41]. The NO_x emissions of experimental and this numerical research, as a function of equivalence ratio and swirl number, are presented in figures 1-5 to 4-5. Figures 1-5 and 2-5 present the tubular combustor (L/L0=0), while figures 3-5 and 4-5 present the annular combustor, as shown in figures 1-5 to 4-5. It can be seen that predicted values of NO_x emissions agree very well with measured data for the equivalence ratios between 0.6 and 0.85, except for the highest value of swirl number (S = 1.13).

These findings of NO_x emission show that the applied numerical method can be used with a high level of confidence when burning pure propane. It can be assumed, therefore, that a similar level of confidence can be expected for numerical analysis of propane/hydrogen mixtures for lower concentrations of hydrogen of up to 10% vol of hydrogen.

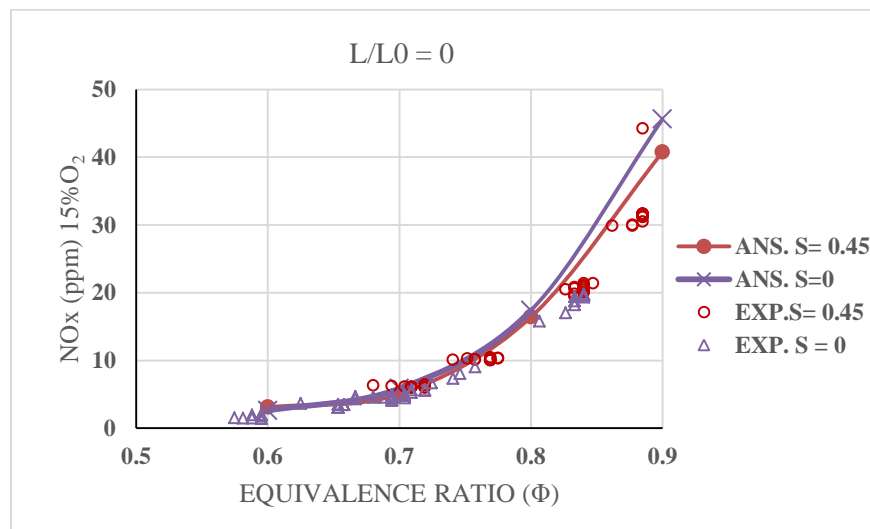


Figure 5-1 Experimental and numerical NO_x emissions for tubular combustion as a function of equivalence ratio and (S=0 and S= 0.45).

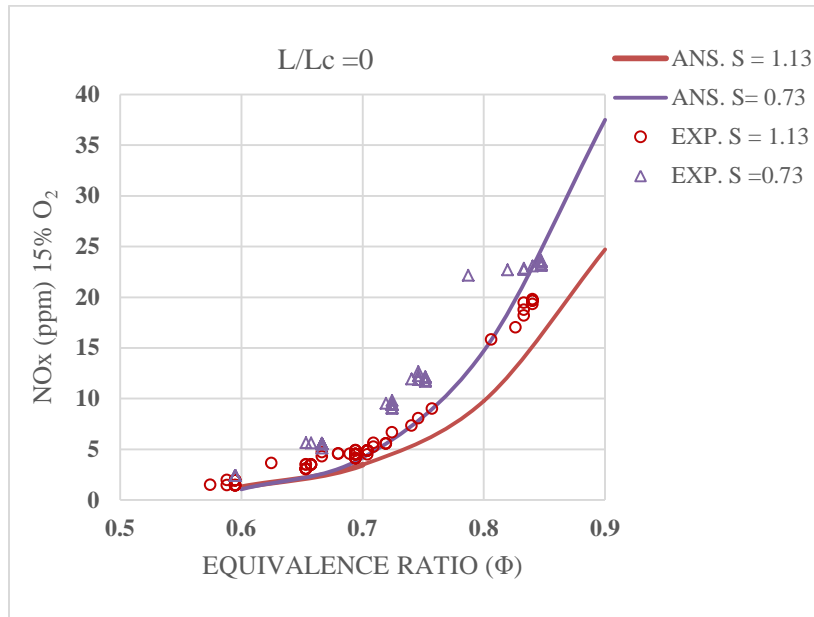


Figure 5-2 Experimental and numerical NO_x emissions for tubular combustion as a function of equivalence ratio and (S=0.73 and S= 1.13).

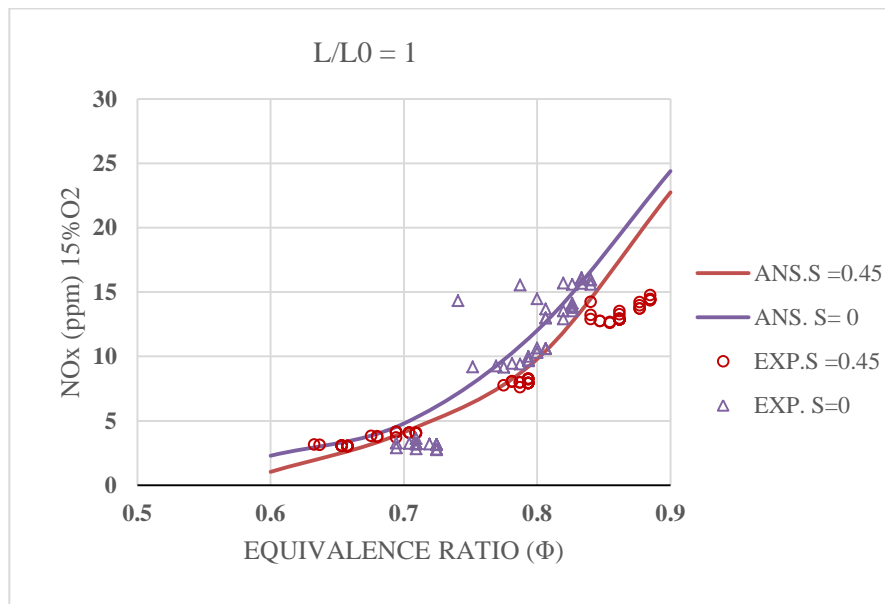


Figure 5-3 Experimental and numerical NO_x emissions for annular combustion as a function of equivalence ratio and (S=0 and S= 0.45).

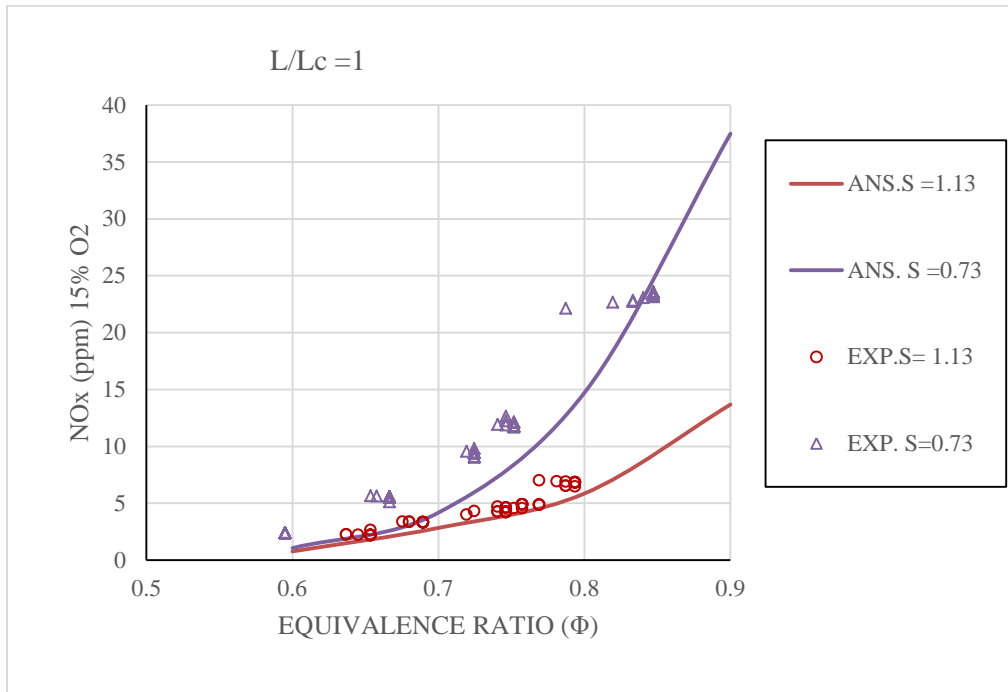


Figure 5-4 Experimental and numerical NO_x emissions for annular combustion as a function of equivalence ratio and (S=0.73 and S= 1.13).

Figures 5-5 and 5-6 show the average temperature at the outlet of combustion chamber at equivalence ratios 0.8 and 0.9, respectively. It can be seen that the maximum temperature at the outlet is at $s=0$ while the minimum temperature occurs at $s=1.13$. These results are due to the cooling effects of the center body and wall of combustor, increased heat transfer rates with swirl number. Also, the average temperature on the outlet for swirl numbers 0.45, 0.73 and 1.13 (at $L/L_0 = 0$) are less than that of ($s=0$) by 1.31%, 4.2% and 7.46% which is clear from Figs.4 a, b, c and d.

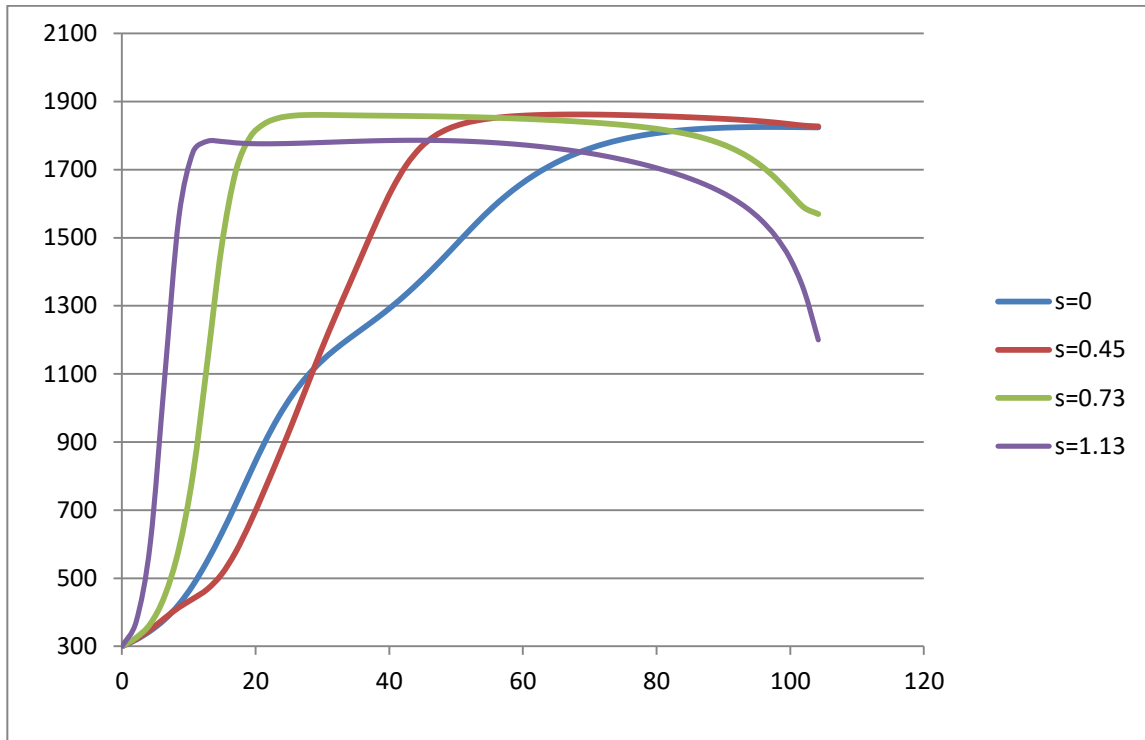


Figure 5-5 Temperature profiles along (x-x) line at $\Phi=0.7$, $L/L_0=0$ and various swirl numbers.

Figures 5-5 illustrate the temperature distribution along (x-x) line in the case of $L/L_0=0$ for swirl numbers ($S = 0, 0.45, 0.73$ and 1.13) and equivalence ratio $\Phi = 0.7$. It can be seen that in general, the increase of the swirl number moves the flame closer to the combustor inlet. The peak temperature takes places at $x=89$ mm for ($s = 0$), $x= 59$ mm for ($s= 0.45$), $x=27.5$ mm for ($s=0.73$) and $x=13$ mm for the strongest swirl ($s=1. 13$). As shown in figure 5-5 the maximum temperature levels are around 1820 K in case of ($s = 0$), 1858 K with ($s = 0.45$), 1860 K in case of ($s = 0.73$) and 1784 K in case of ($s = 0.73$).

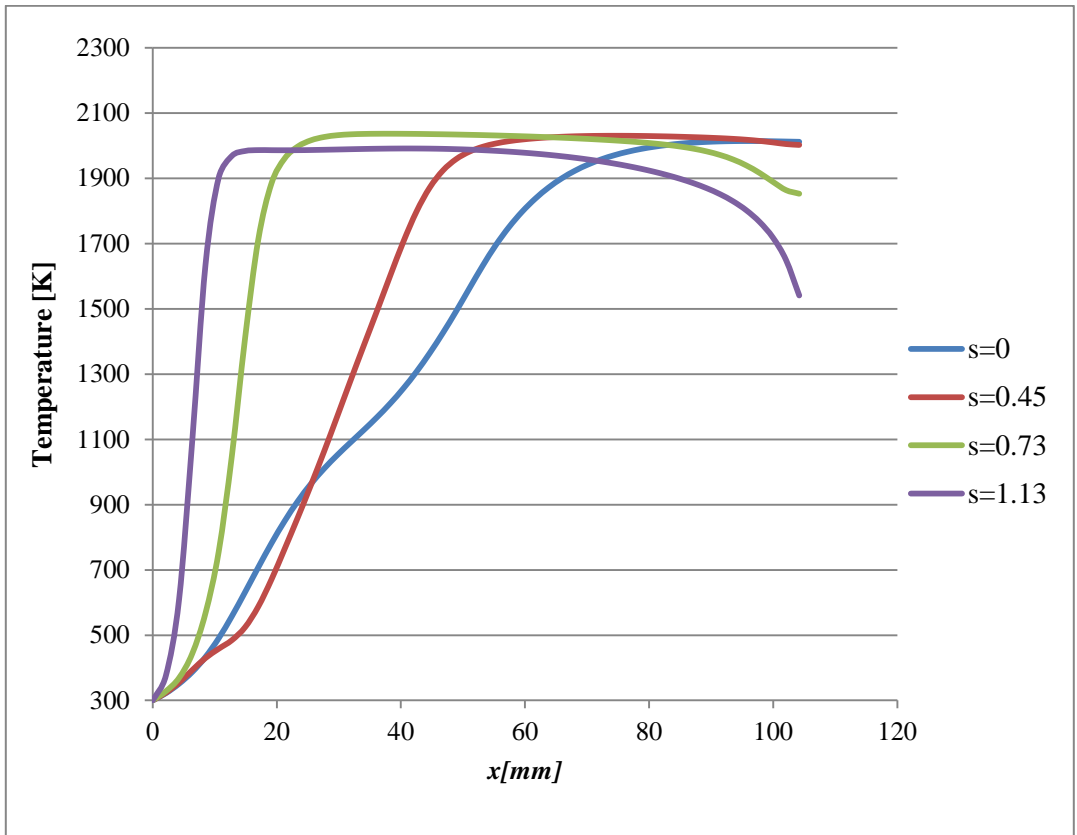


Figure 5-6 Temperature profiles along (x-x) line at $\phi=0.8$, $L/L_0=0$ and various swirl numbers.

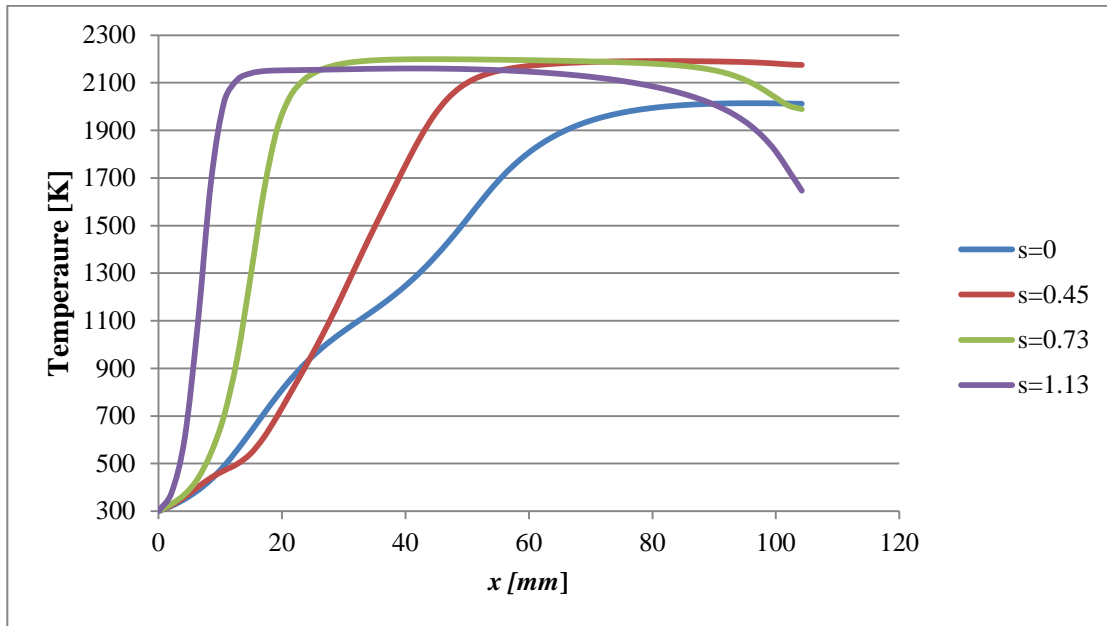


Figure 5-7 Temperature profiles along (x-x) line at $\phi=0.9$, $L/L_0=0$ and various swirl numbers.

Figures 5-5, 5-6 and 5-7 represent the temperature profiles along (x-x) line for swirl numbers ($s = 0, 0.45, 0.73$ and 1.13) and equivalence ratios $\Phi = 0.7, 0.8$ and 0.9 for the tubular combustor ($L/L_0=0$). As shown in figures 5-5, 5-6 and 5-7, in general, the temperature profiles for the same swirl numbers show similar trend in all cases of equivalence ratio $\Phi = 0.7, 0.8$ and 0.9 . In addition, close to the outlet of combustor the temperature gradient decreases, which can be seen for swirl number of ($s = 0.73$ and 1.13). This effect can be attributed to formation of the central recirculation zone (CRZ) at the combustor outlet, as shown in the figure (5-17).

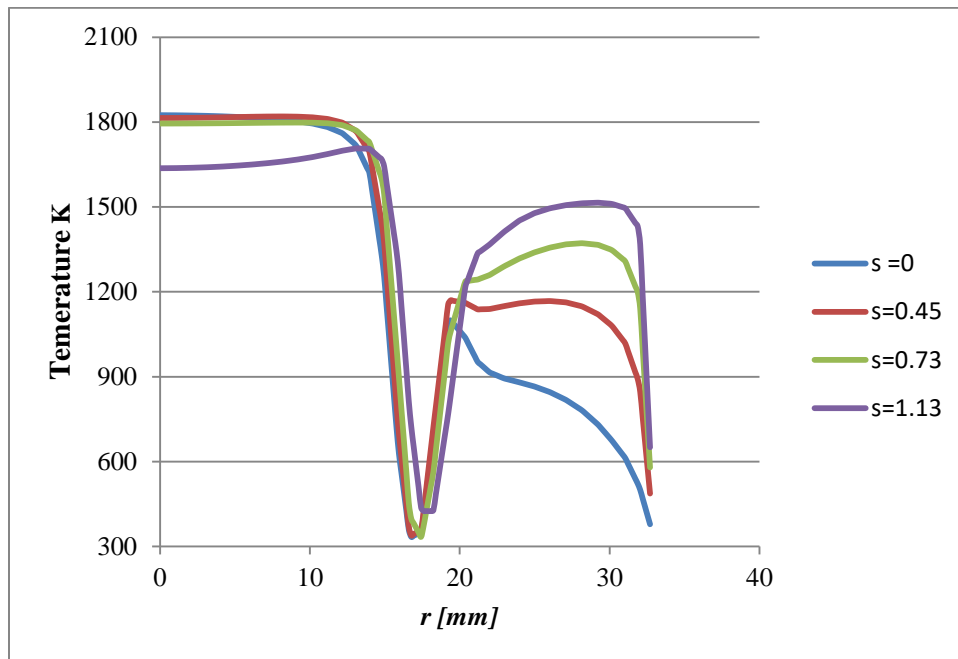


Figure 5-8 Radial temperature profiles at $z=4$ mm, $\Phi=0.7$, $L/L_0=0$ and various swirl numbers.

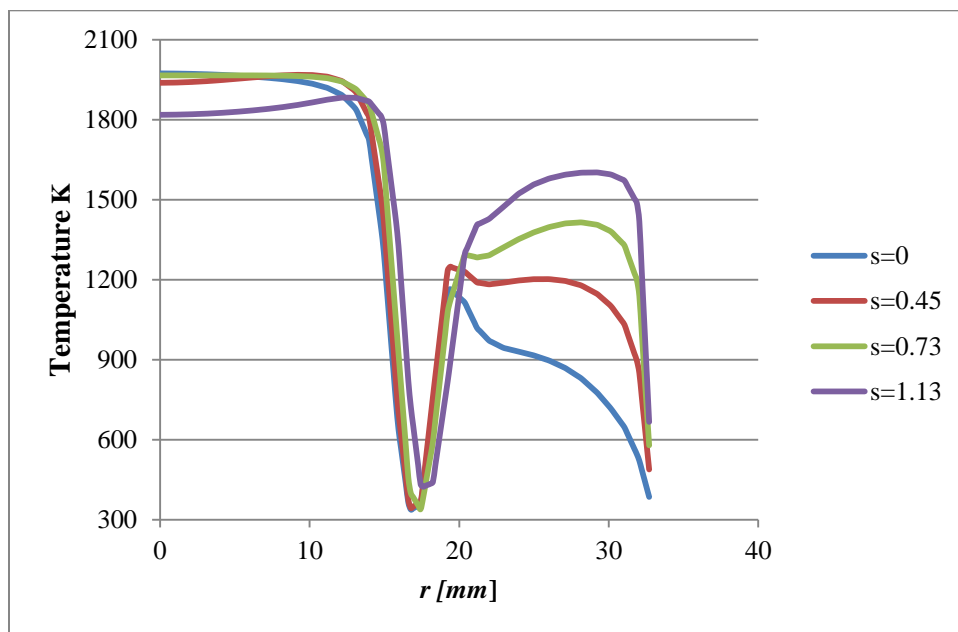


Figure 5-9 Radial temperature profiles at $z=4$ mm, $\Phi=0.8$, $L/L_0=0$ and various swirl numbers.

numbers.

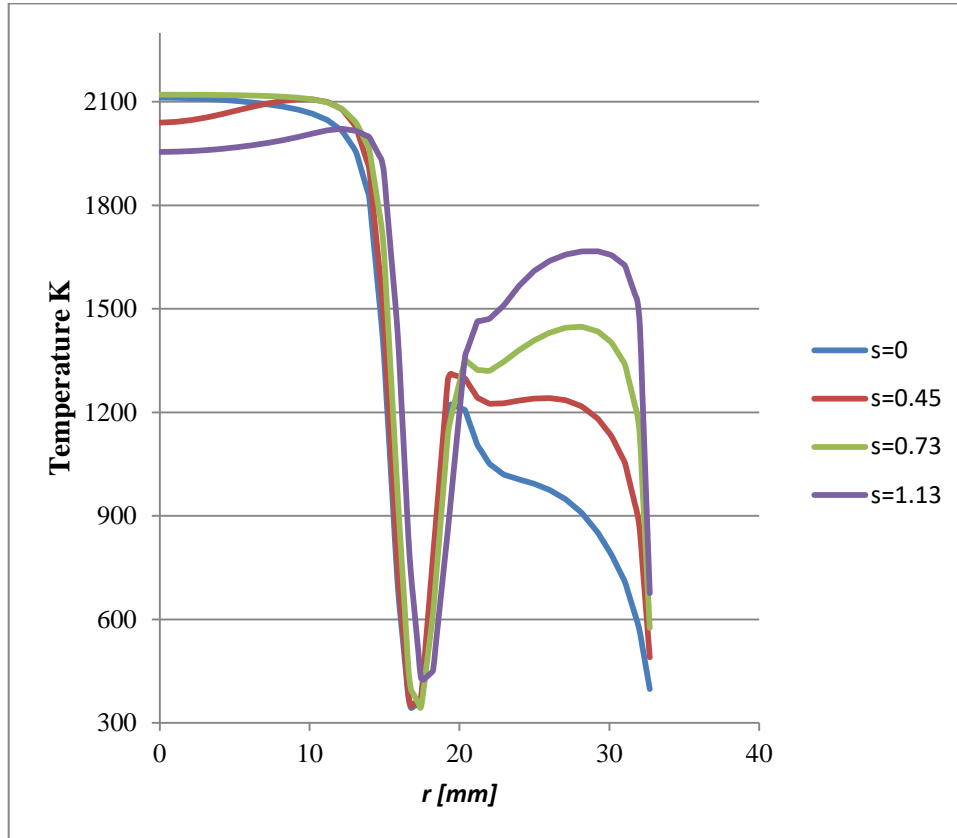


Figure 5-10 Radial temperature profiles at $z=4$ mm, $\phi=0.9$, $L/L_0=0$ and various swirl numbers.

The effect of swirl number on the radial temperature gradients at axial distance of ($z=4$ mm) for tubular combustor ($L/L_0=0$) is plotted in figures 5-8, 5-9 and 5-10 for equivalence ratio $\Phi =0.7$, 0.8 and 0.9 respectively. It can be seen from the figures that there is a small effect of increasing swirl number on temperature distribution in the preheat zone, while near to the wall area from $r=20$ mm to $r=33$ mm It is very clear that the effect of increasing swirl number increases the temperature level. This results is expected because a higher swirl number leads to decrease of the size of WRZ for confined flow and therefore decreases cooling rate with the wall, as shown in figure 5-17.

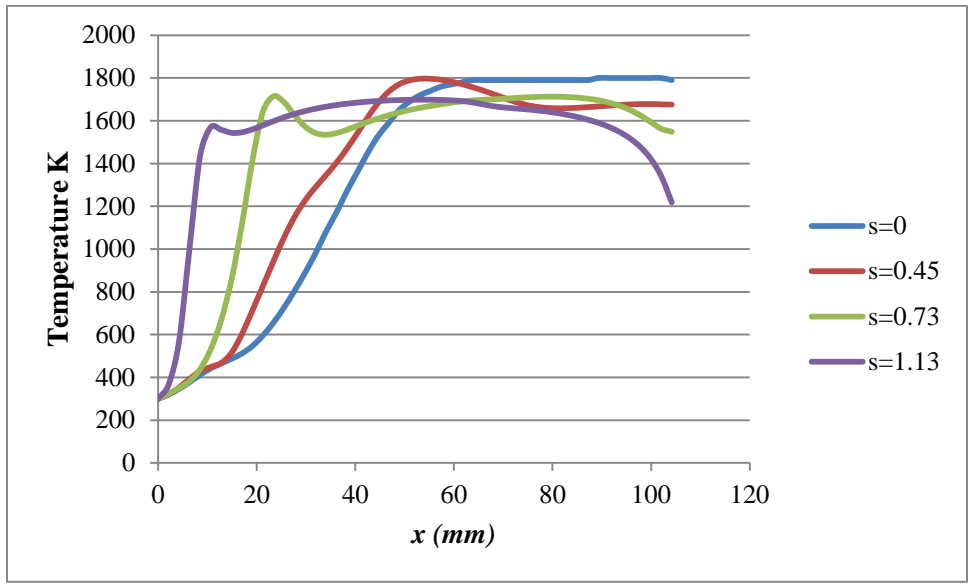


Figure 5-11 Temperature profiles along (x-x) line at $\phi=0.7$, $L/L_0=1$ and various swirl numbers.

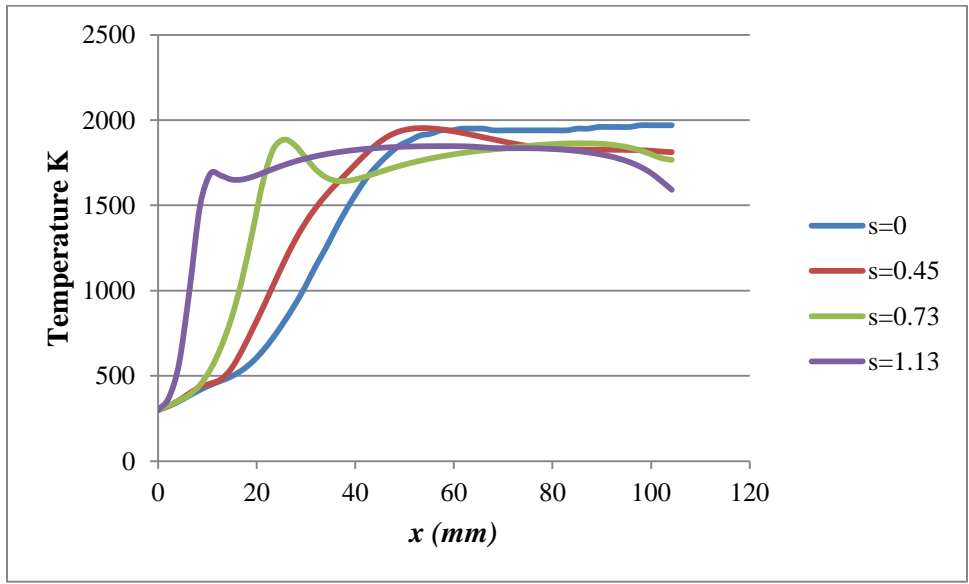


Figure 5-12 Temperature profiles along (x-x) line at $\phi=0.8$, $L/L_0=1$ and various swirl numbers.

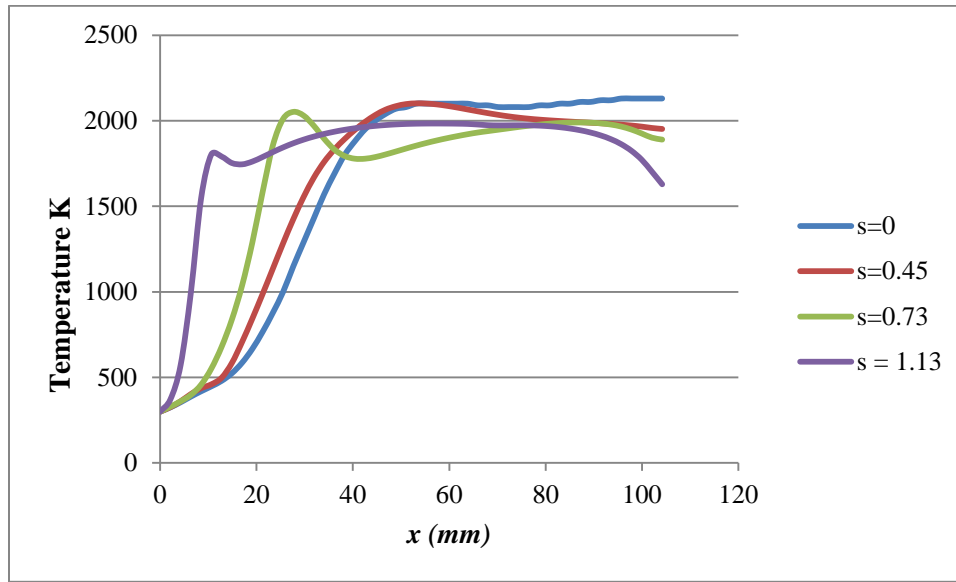


Figure 5-13 Temperature profiles along (x-x) line at $\phi=0.9$, $L/L_0=1$ and various swirl numbers.

Figures 5-11, 5-12 and 5-13 represent the temperature profiles along (x-x) line for swirl numbers ($s = 0, 0.45, 0.73$ and 1.13) and equivalence ratio $\Phi = 0.7, 0.8$ and 0.9 for the annular combustor ($L/L_0=1$). As shown in these figures the temperature profiles for the same swirl numbers show similar trend in all cases of equivalence ratio $\Phi = 0.7, 0.8$ and 0.9 . in addition, in cases of swirl numbers of ($s = 0.73$ and $s = 1.13$), the temperature profile for these cases has inflection point at $x = 10.5$ mm and 25.5 mm respectively, which takes place due to wall recirculation zones (WRZ) of the central body as shown in figures 5-18 and 5-19. Also, close to the outlet of combustor the temperature gradient decreases which can be clear for swirl number of ($s=0.73$ and 1.13), this affect attribute to formation of the central recirculation zone (CRZ) at the combustor outlet as shown in the figure 5-18 and 5-19.

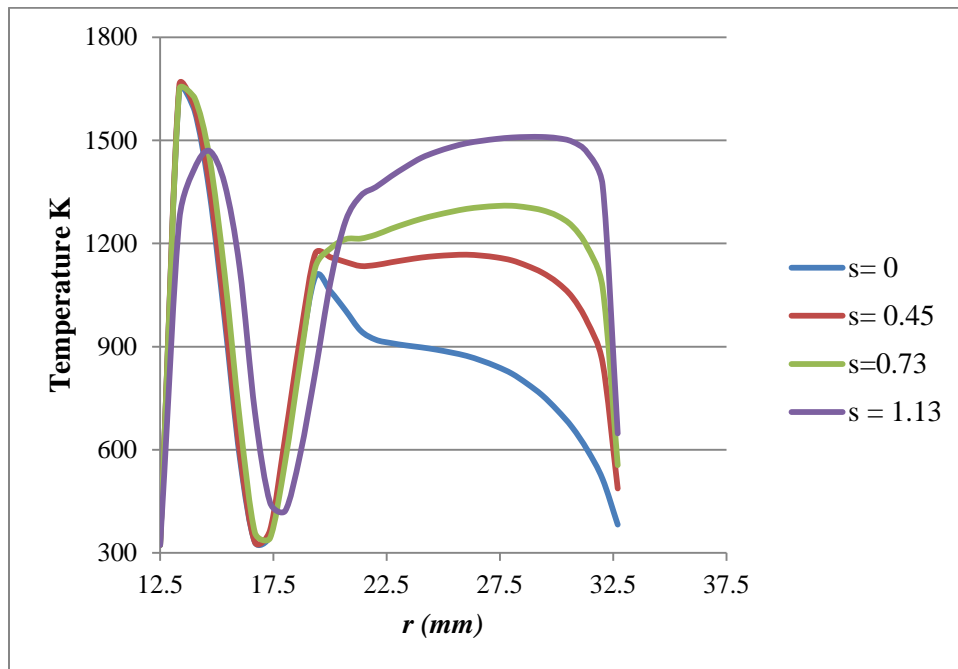


Figure 5-14 Radial temperature profiles at $z=4$ mm, $\phi=0.7$, $L/L_0=1$ and various swirl numbers.

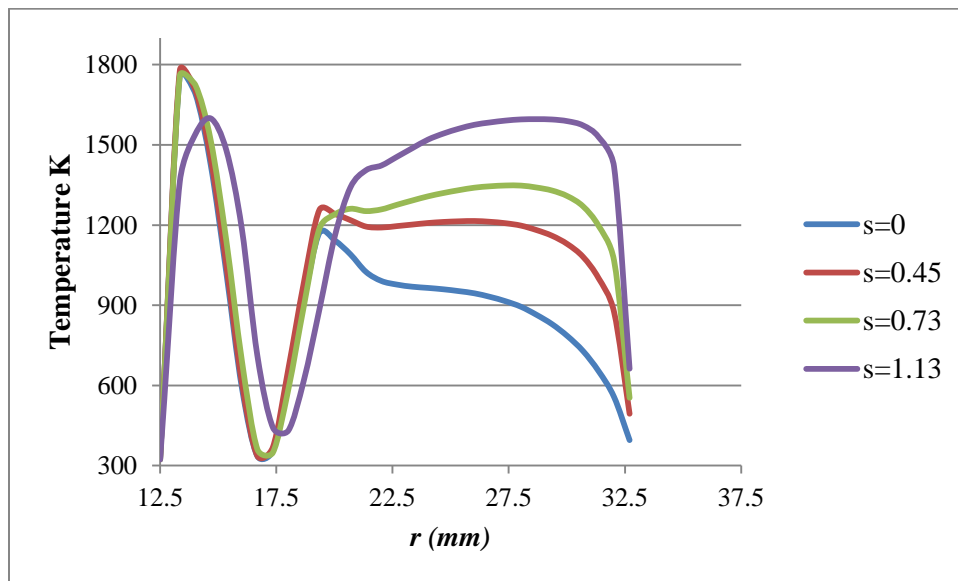


Figure 5-15 Radial temperature profiles at $z=4$ mm, $\phi=0.8$, $L/L_0=1$ and various swirl numbers.

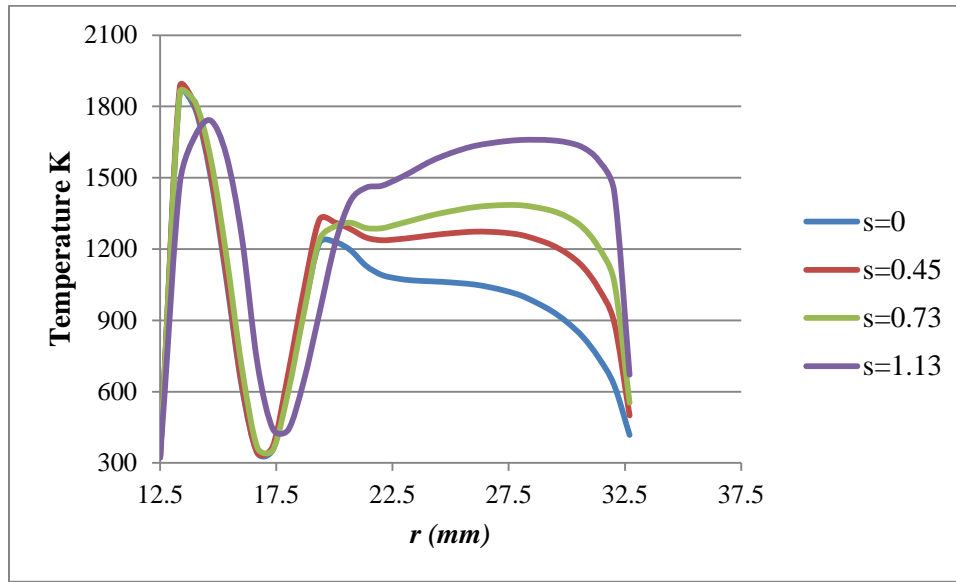


Figure 5-16 Radial temperature profiles at $z=4$ mm, $\Phi=0.9$, $L/L_0=1$ and various swirl numbers.

The effect of swirl number on the radial temperature gradients at axial distance of ($z=4$ mm) for annular combustor ($L/L_0=1$) is represented in figures 5-14, 5-15 and 5-16 for equivalence ratio $\Phi = 0.7, 0.8$ and 0.9 respectively. The first noticeable observation from the figures is the small effect of the increase of swirl number on temperature distribution in the preheat zone, while near to the wall area from $r=20.6$ mm to $r= 33$ mm, it is very clear that the effect of increasing swirl number increases the temperature level. This result is expected because a higher swirl number leads to decrease of the size of WRZ and therefor to decrease of heat transfer rate with the wall, as shown in figures 5-18 and 5-19. Also near the center body where $r= 12.5$ mm to $r= 15$ mm, the temperature falls down in the case of swirl number ($s=1.13$) which can be attribute to formation of stronger central recirculation zone (CRZ), with pronounced mixing, as shown in figures 5-18 and 5-19.

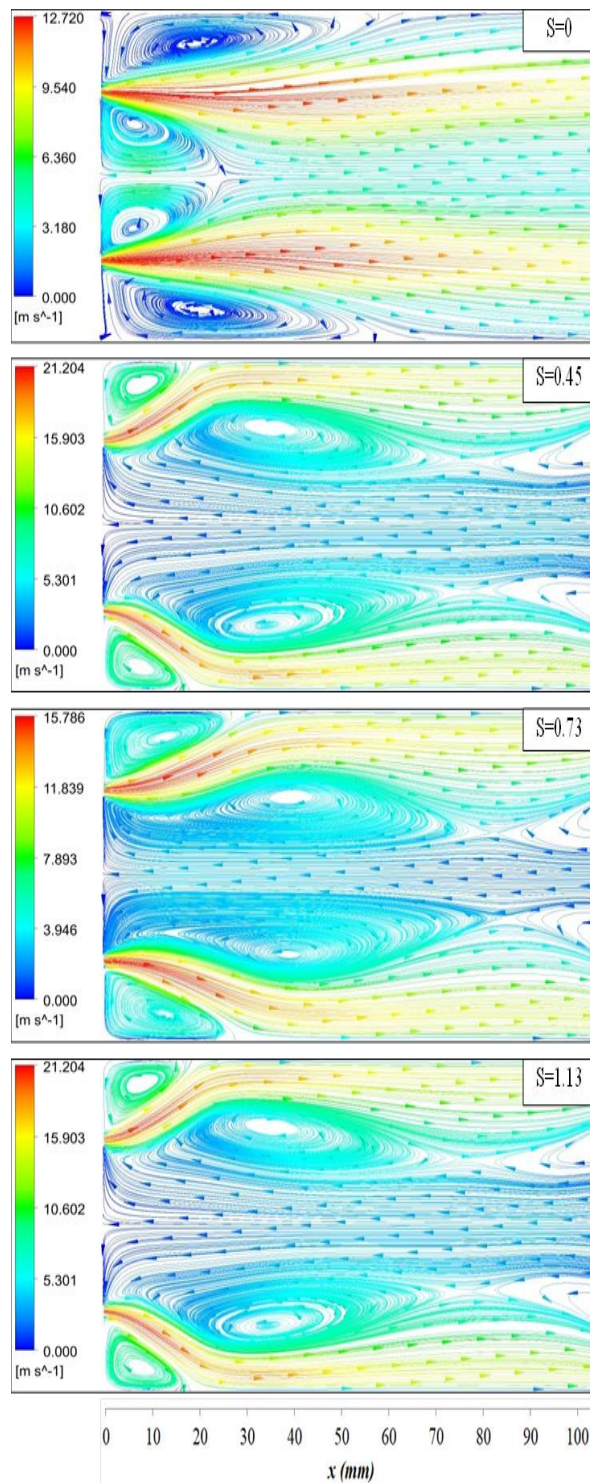


Figure 5-17 Flow structure along the central plane of tubular combustor ($L/L_0=0$) for $\Phi = 0.8$, and different swirl numbers for base fuel.

Streamline pattern contours are plotted along a central plane of the tubular combustion chamber ($L/L_0=0$) for four swirl numbers (0, 0.45, 0.73 and 1.13) at equivalence ratio $\Phi = 0.8$, as shown in figure 5-17, The first noticeable observation is the presence of a central recirculation zone (CRZ) at the combustor inlet and wall recirculation zones (WRZ) in the burner corners. As the swirl number increases, the length of the WRZ decreases; this is due to the radial expansion of the flow under the swirl effect. At no-swirling flow ($S = 0$) the CRZ is smaller compared to the size of the WRZ, as can be observed in this case, the length of CRZ is about 24 mm, while, the WRZ length is about 59 mm. For strong swirl number ($S=1.13$), the flow structure is different and the size of the WRZ is reduced, contrary to the size of WRZ, the CRZ reaches a length of 80 mm, while the WRZ length decreases to 17 mm. Also, in cases of swirl numbers (0.73 and 1.13), it can be seen that recirculation zone at the combustor outlet increases with s to the length of about 25 mm for ($S = 1.13$).

Comparing flow structures of tubular and annular combustors for $\Phi = 0.8$, different swirl numbers and base fuel, Figs 5-17 and 5-18, it can be concluded that the WRZs are similar for all cases except for lower swirl, $s = 0.45$, where for the annular case is of double size vs. tubular one. Also, for $s=0.45$ CRZ do not exist in annular combustor. For no swirl and $s = 0.45$ cases the CRZs for annular combustor are moved at the top of the center body. For $s = 0.73$, annular case, the CRZ consist of two zones, one at the $2/3 L$ and the other at the center body top. For strong swirl $s = 1.13$, recirculation zones are similar except that the annular has a one CRZ more, at the center body top.

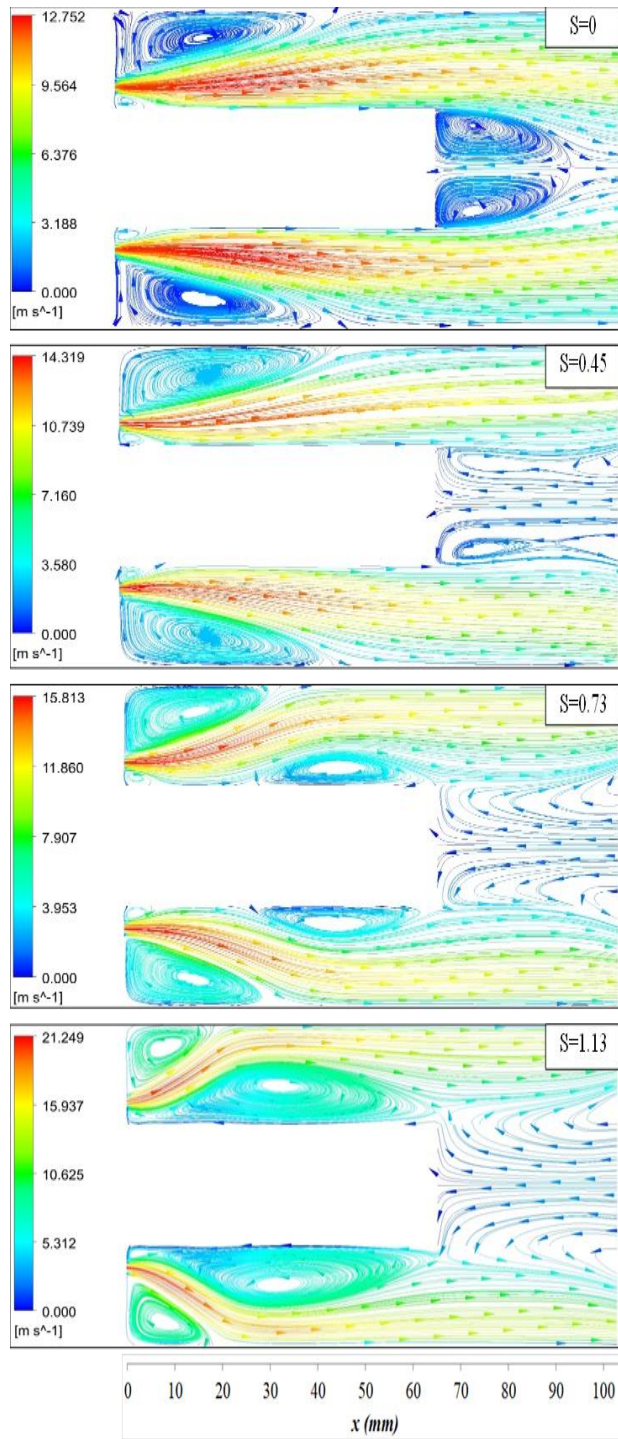


Figure 5-18 Flow structure along the central plane of annular combustor for $\Phi = 0.8$, $L/L_0=1$, and different swirl numbers for base fuel.

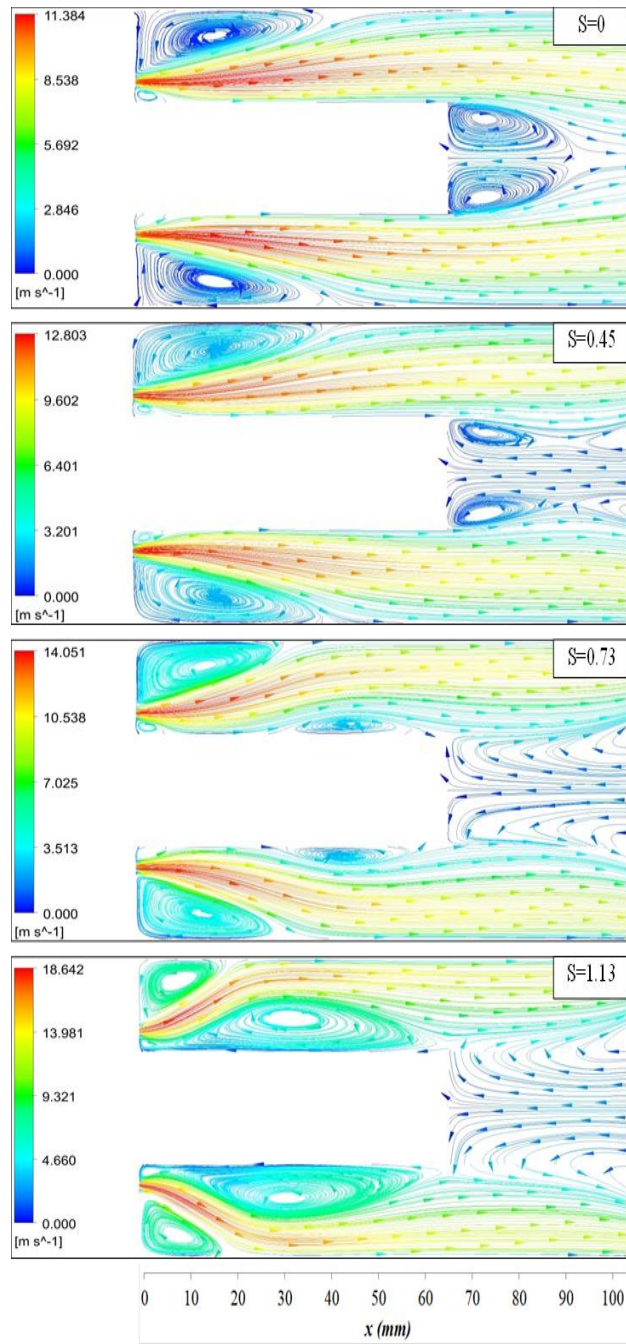


Figure 5-19 Flow structure along the central plane of annular combustor for $\Phi = 0.9$, and different swirl numbers for base fuel.

Streamline pattern contours are plotted along a central plane of the annular combustion chamber ($L/L_0=1$) for four swirl numbers (0, 0.45, 0.73 and 1.13) at equivalence ratio $\Phi = 0.8$ and 0.9. As shown in figures 5-18 and 5-19, wall recirculation zones (WRZ) in the burner corners, as the swirl number increases, the length of the WRZ decreases, which is the same as mentioned for tubular combustion chamber ($L/L_0=0$). As can be observed from the figures at no-swirling flow ($s = 0$), the central recirculation zone (CRZ_1) is formed at the end of the center body, by increasing swirl number, the second central recirculation zone (CRZ_2) appears at outlet of combustor chamber. For strong swirl numbers ($s= 0.73$ and 1.13), the CRZ_1 and CRZ_2 are formed on one CRZ. Also it can be seen for $s= 0.73$ and 1.13, the third central recirculation zone CRZ_3 appears beside the center body, which is small in case of $s= 0.73$ (25 mm length) and biggest in case of 1.13 (57 mm length).

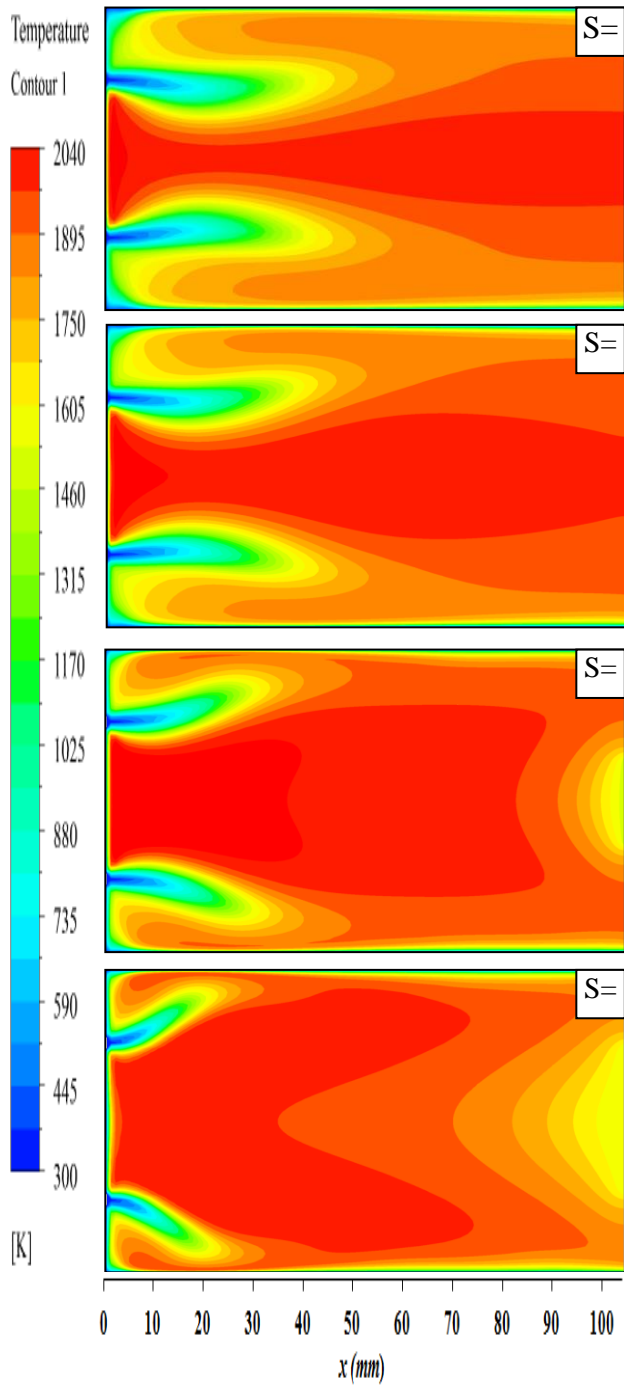


Figure 5-20 Temperature distributions along the central plane of combustor chamber at $\Phi = 0.8$, $L/L_0 = 0$ and various swirl numbers.

Figure 5-20 represents the mean temperature distribution along a central plan of the combustor, equivalence ratio ($\phi=0.8$) and various swirl numbers (0, 0.45, 0.73 and 1.13) for tubular combustion ($L/L_0=0$). It can be observed that by increasing the swirl number, the shape of maximum temperature zone is changed. At non-swirling flow ($s = 0$) the length of that zone reaches a location of the outlet of combustor (104 mm), while, for swirl numbers (0.45, 0.73 and 1.13) reach locations of 96mm, 81mm and 58mm, respectively. Moreover, it can be seen at swirl numbers (0.73 and 1.13) that zone becomes thick and tends to take the M-shape and also, due to recirculation zone close to the outlet of combustor, a decreasing temperature zone appears near the outlet.

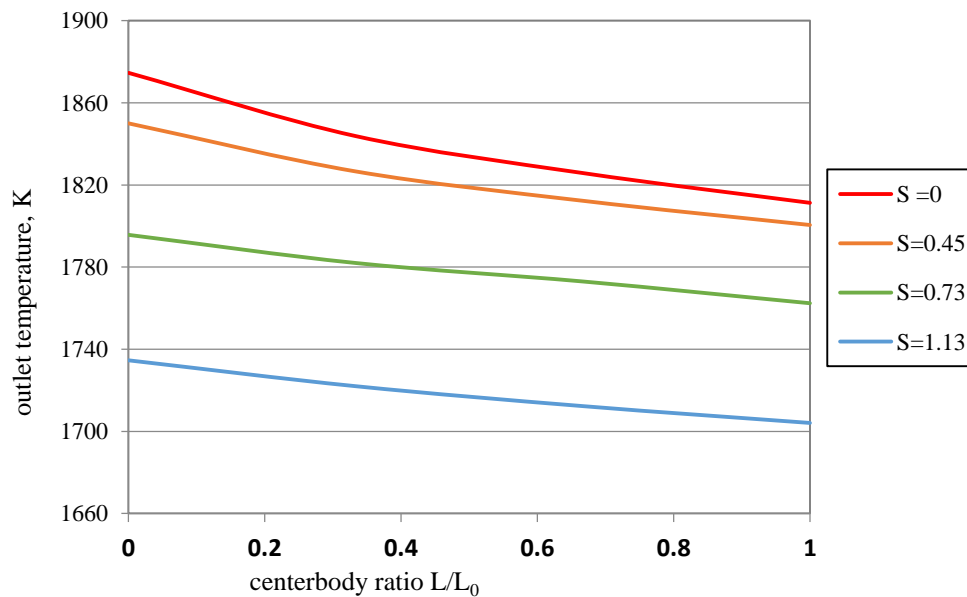


Figure 5-21 Variation of average temperature at outlet with the central body ratio at equivalence ratio 0.8

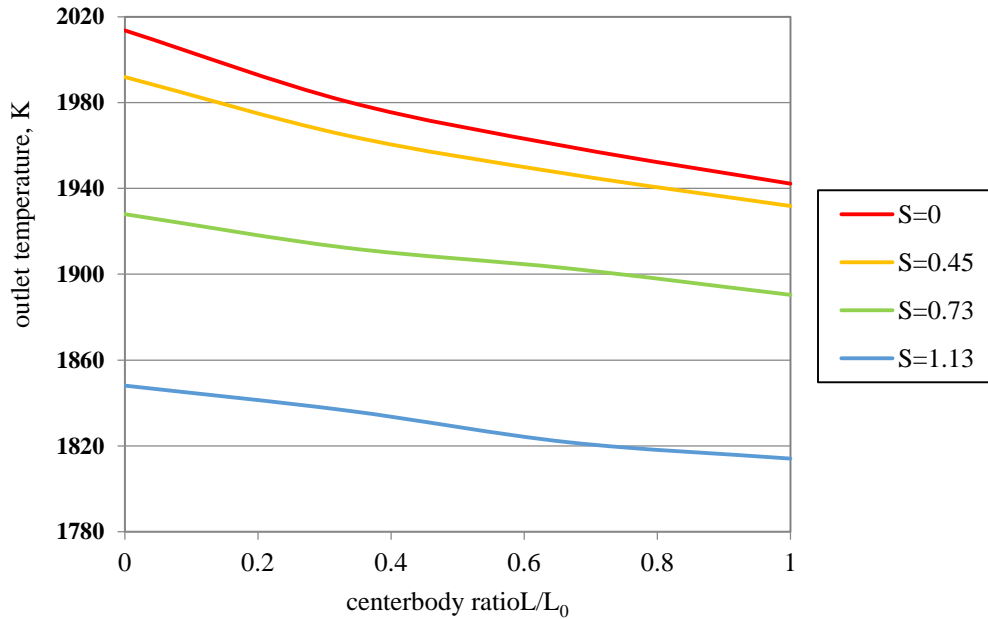


Figure 5-22 Variation of average temperature at outlet with the central body ratio at equivalence ratio 0.9

For more details of overall effect of the center body on temperature at the outlet of combustion chamber, Figures 5-21 and 5-22 show the average temperature at the outlet of combustion chamber at equivalence ratios 0.8 and 0.9 respectively, at different center body length, it can be seen that the maximum temperature at the outlet is at $s = 0$ while the minimum temperature occurs at $s=1.13$. These results are due to the cooling effects of the center body and wall of combustor, increased heat transfer rates with swirl number, also from Figure 5-21 and 5-22, it is observed that the average temperature on the outlet for swirl numbers 0.45, 0.73 and 1.13 (at $L/L_0 = 0$) are less than that of ($s=0$) by 1.31%, 4.2% and 7.46% .

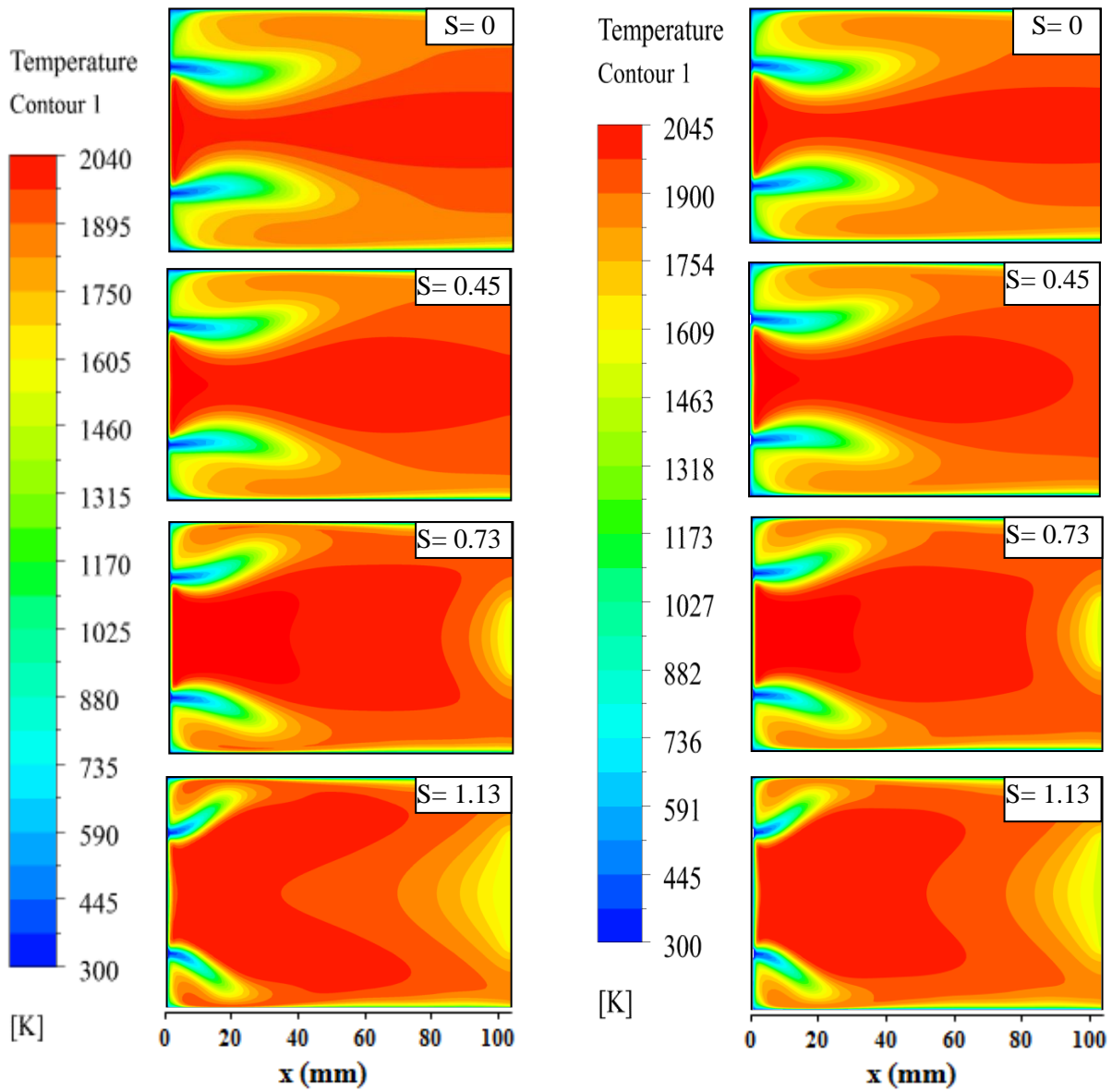


Figure 5-23 Temperature distributions along the central plane for $\Phi = 0.8$, and different swirl numbers (left, base fuel, right - 90%vol base fuel and H₂ 10%vol).

Figure 5-23 represents the mean temperature distribution along the central plane of combustor for equivalence ratio $\Phi = 0.8$ and different swirl numbers (0, 0.45, 0.73 and 1.13). It can be observed that by increasing the swirl number, the shape of high temperature zone changes. For flow with no swirl ($s=0$) the flame is elongated, narrow, and protrudes out of the combustor. With the increase of swirl number (0.73 and 1.13) the flame becomes wider, shorter and ends inside the combustor for both fuels. The most pronounced difference between the flames of these two fuels can be seen in ($s = 1.13$). The flame of propane/hydrogen mixture is shorter and more compact than that of propane. This can be attributed to the increase of flame speed of the propane / hydrogen mixture. Comparison of these two cases shows very similar images with one noticeable difference: the central high temperature zone is slightly shorter in the case of base fuel/hydrogen mixture.

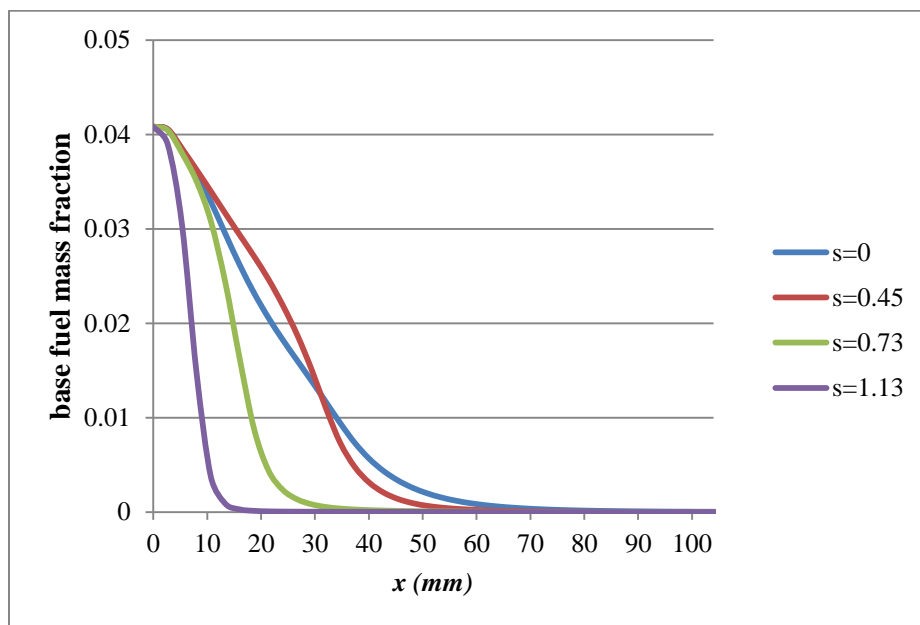


Figure 5-24 Base fuel mass fraction of mixed base fuel-hydrogenair flame along (x-x) line at $\Phi=0.7$, $L/L_0=0$ and various swirl numbers.

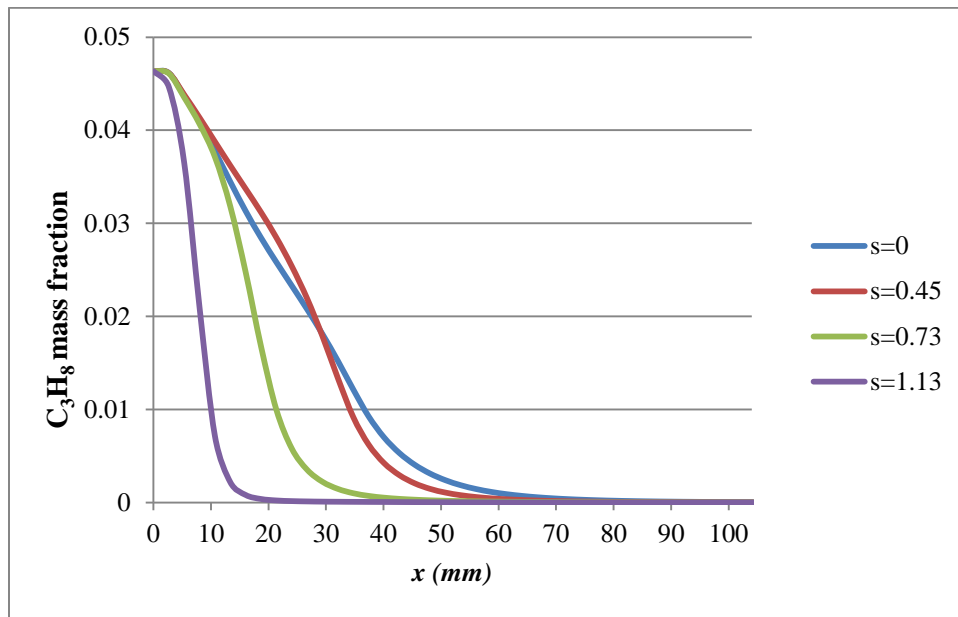


Figure 5-25 Base fuel mass fraction of mixed base fuel-hydrogen- air flame along (x-x) line at $\phi=0.8$, $L/L_0=0$ and various swirl numbers

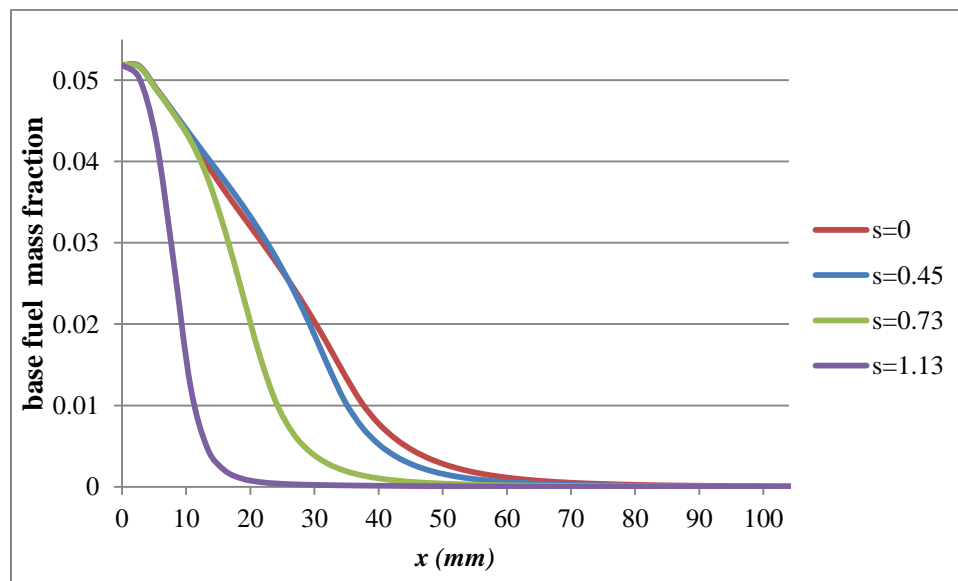


Figure 5-26 Base fuel mass fraction of mixed base fuel-hydrogen-air flame along (x-x) line at $\phi=0.9$, $L/L_0=0$ and various swirl numbers.

The mass fraction profile of propane of mixed propane-hydrogen- air flames at equivalence ratio ($\phi=0.7, 0.8$ and 0.9) with swirl intensities of $0, 0.45, 0.73$ and 1.13 are shown in figures 5-24, 5-25 and 5-26. The results show that the increasing of swirl number leads to decrease distance consumption of propane to reach the minimum value. It is clear from figure 5-24, at equivalence ratio ($\phi=0.7$), the minimum values of C_3H_8 fraction are located at around 78 mm, 62 mm, 41 mm and 17 mm for swirl number $s=0, 0.45, 0.73$ and 1.13 , respectively. While from figure 5-25, at equivalence ratio ($\phi=0.8$), propane is fully consumed at around 81 mm, 68 mm, 51 mm and 24 mm for swirl number $s=0, 0.45, 0.73$ and 1.13 , respectively. Also, in case of equivalence ratio ($\phi=0.9$), for figure 5-26, the minimum values of fuel fraction are located at 85 mm, 75 mm, 60 mm and 33 mm for swirl number $s=0, 0.45, 0.73$ and 1.13 respectively. It can be noticed that at constant equivalence ratio, the increasing of swirl number leads to a faster combustion of fuel/air mixtures.

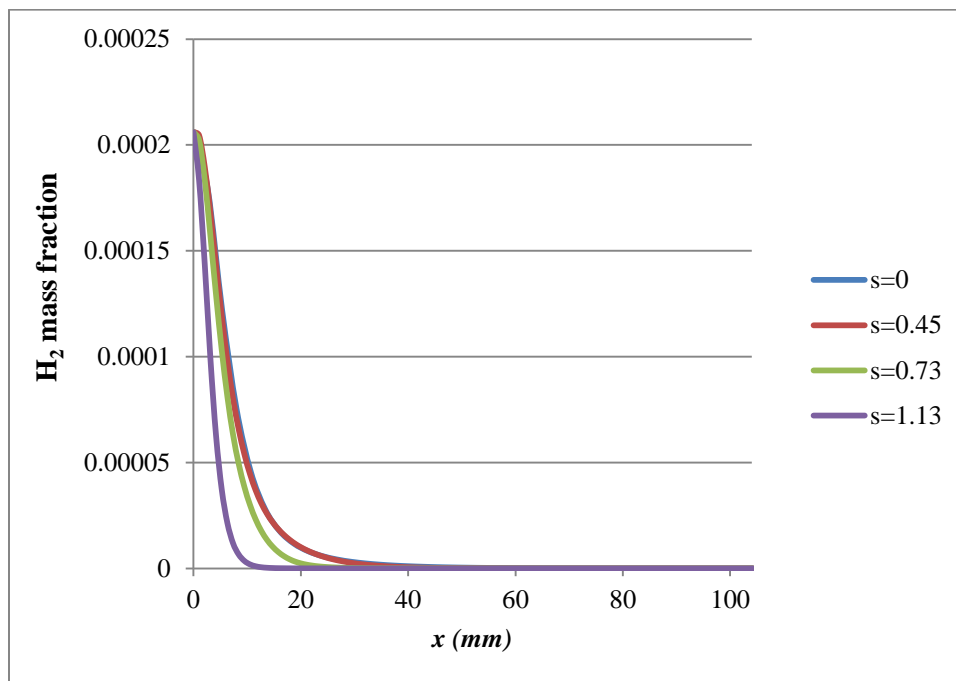


Figure 5-27 Hydrogen mass fraction of mixed fuel-hydrogen- air flame along (x-x) line at $\phi=0.7, L/L_0 = 0$ and various swirl numbers.

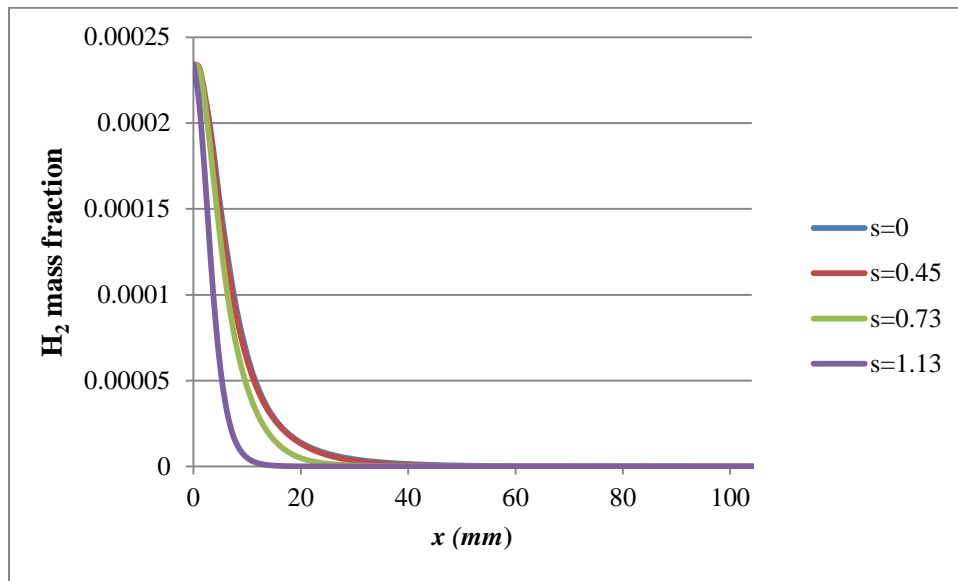


Figure 5-28 Hydrogen mass fraction of mixed propane-hydrogen- air flame along (x-x) line at $\Phi=0.8$, $L/L_0 = 0$ and various swirl numbers.

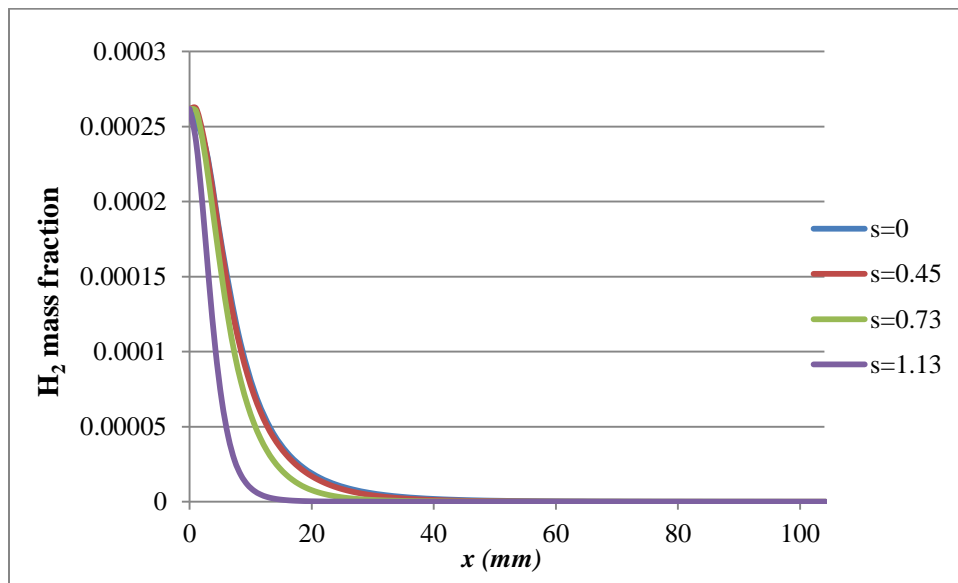


Figure 5-29 Hydrogen mass fraction of mixed base fuel-hydrogen-air flame along (x-x) line at $\Phi=0.9$, $L/L_0 = 0$ and various swirl numbers.

The mass fraction profile of hydrogen of mixed propane-hydrogen- air flames at equivalence ratio ($\phi=0.7, 0.8$ and 0.9) with swirl intensities of $0, 0.45, 0.73$ and 1.13 are shown in figures 5-27, 5-28 and 5-29. It is from figures, hydrogen is almost fully consumed at around 44 mm, 40 mm, 32 mm and 19 mm for swirl numbers $s=0, 0.45, 0.73$ and 1.13 , respectively. A noticeable difference between propane and hydrogen is faster consumption of hydrogen, in general. The effect of swirl increase from 0.45 to 0.73 on fuel consumption is moderate, while for ($s = 1.13$) the rates of consumption have pronounced peaks.

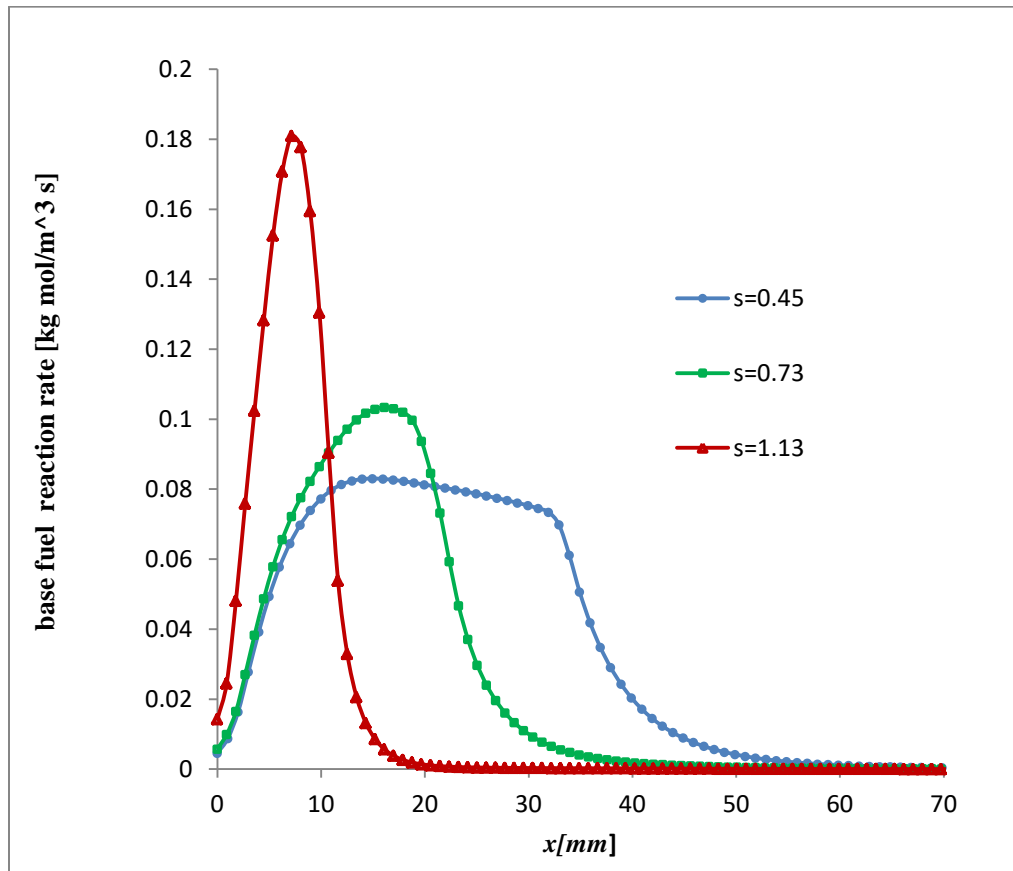


Figure 5-30 Profile of reaction rate of base fuel along (x-x) line at $\phi=0.8, L/L_0=0$ and various swirl numbers.

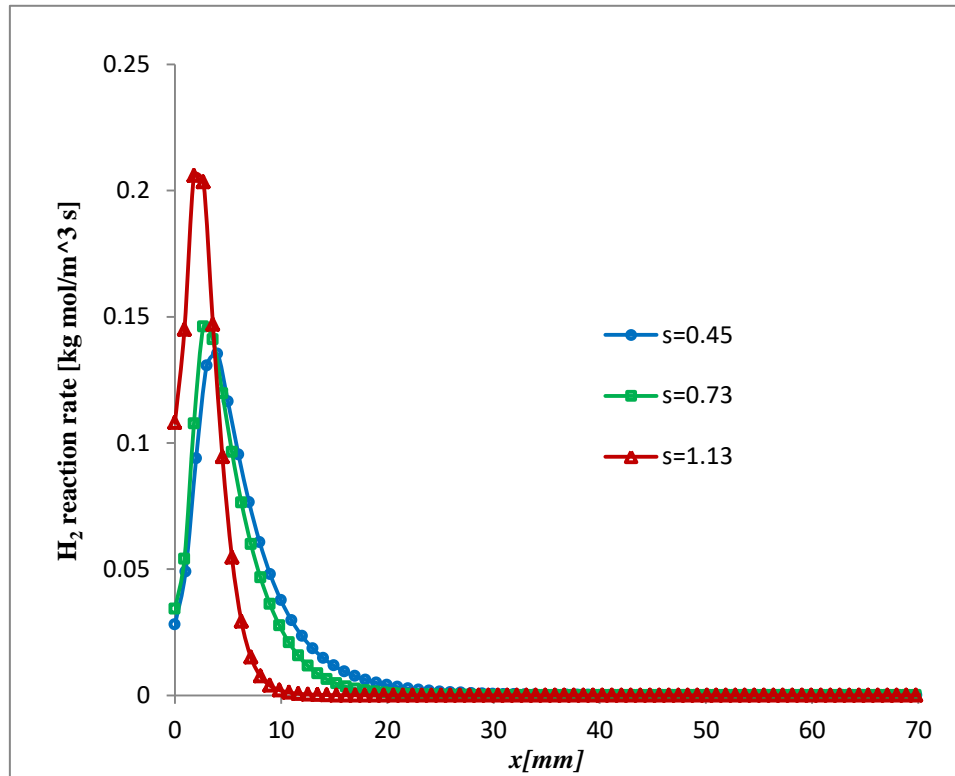


Figure 5-31 Profile of reaction rate of hydrogen along (x-x) line at $\phi=0.8$, $L/L_0=0$ and various swirl numbers.

The (x-x) line of fuel reaction rate and hydrogen reaction rate are given in figures 5-30 and 5-31. It can be seen that the increasing of swirl intensity results a high increase for both propane and hydrogen reaction rates. The (x-x) line reaction rate of base fuel increases from 0.0803 at swirl number ($s=0.45$) to 0.1809(kg mole /m³s) at swirl number ($s=1.13$). This augmentation of base fuel reaction rate is about 125 %. This value is reached by the increase of swirl intensity. In addition, as the swirl number increases, the ending point of flame becomes closer to the combustor inlet. These finishing points are located at around 56, 38 and 21mm for swirl numbers 0.45, 0.73 and 1.13 mm, respectively. Regarding the (x-x) line, the reaction rate of hydrogen, increases from 0.1353 at $s=0.45$ to 0.2058 (kg mole /m³s) at $s=1.13$, that is to say, there is an increase of 52%. As a conclusion, the swirl number has a noticeable effect on the reaction rate.

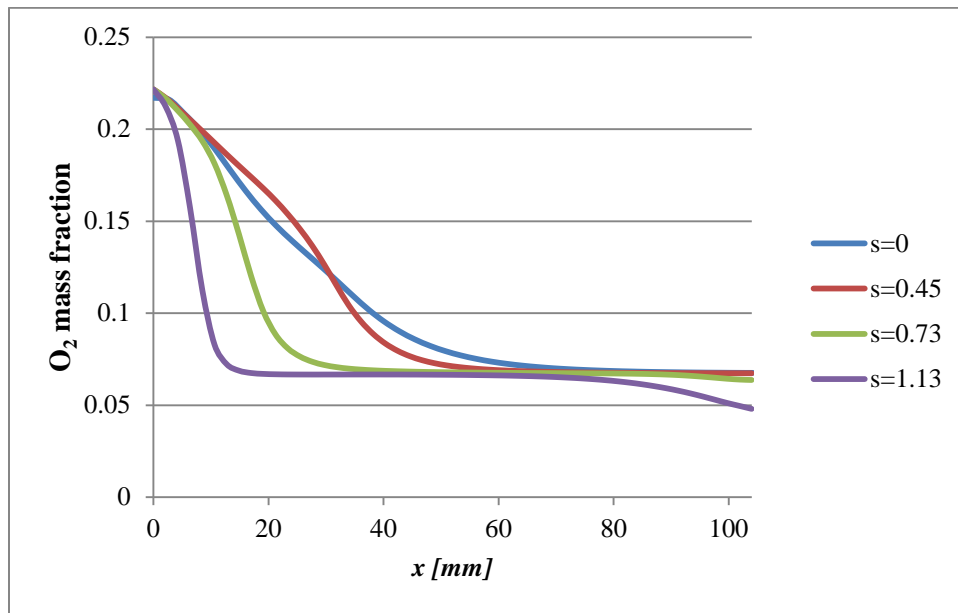


Figure 5-32 Oxygen mass fraction along (x-x) line at $\phi=0.7$, $L/L_0 = 0$ and various swirl numbers.

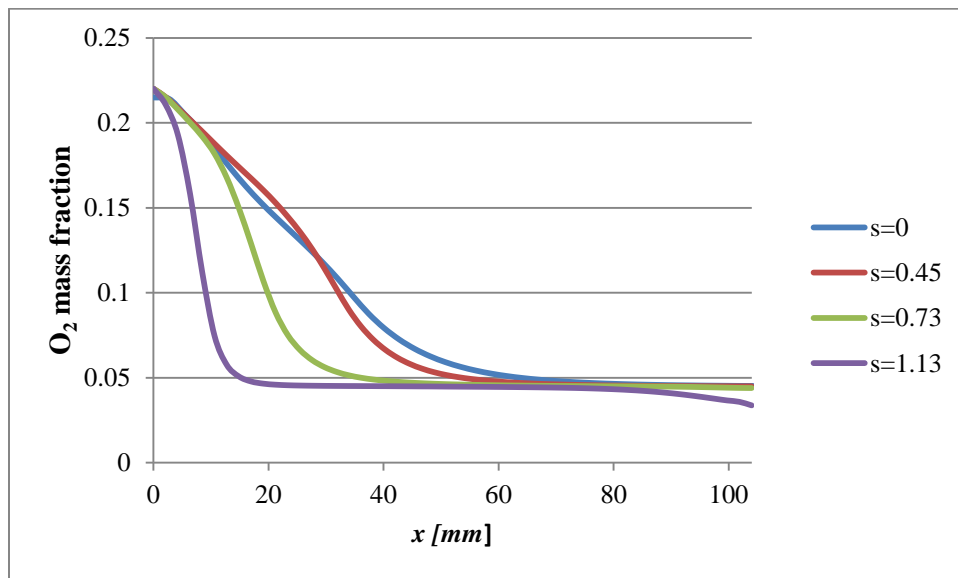


Figure 5-33 Oxygen mass fraction along (x-x) line at $\phi=0.8$, $L/L_0 = 0$ and various swirl numbers.

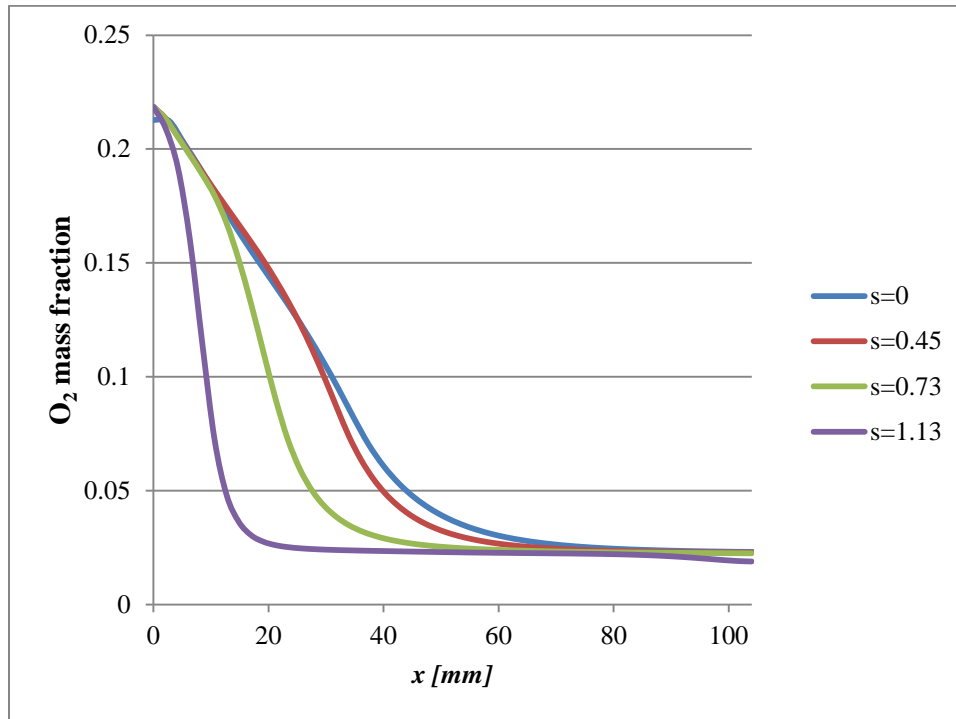


Figure 5-34 Oxygen mass fraction along (x-x) line at $\phi=0.9$, $L/L_0 = 0$ and various swirl numbers.

Figures 5-32, 5-33 and 5-34 represent the mass fraction profiles along (x-x) line of oxygen of premixed base fuel-hydrogen-air flames with various swirl numbers of 0, 0.45, 0.73 and 1.13. As can be seen from these figures, the increase of swirl number leads to a faster consumption of oxygen, The results show that the increasing of swirl number leads to decrease distance consumption of oxygen to reach the minimum value, it is be clear from figures 5-32, 5-33 and 5-34, at equivalence ratio $\phi=0.7$, 0.8 and 0.9 respectively , the minimum values of O_2 fraction are located at around 77 mm, 62 mm, 40 mm and 15 mm for swirl number $s=0$, 0.45, 0.73 and 1.13 respectively. The minimum consumption values are 0.0652, 0.0443 and 0.0221 for equivalence ratio $\phi = 0.7$, 0.8 and 0.9 respectively.

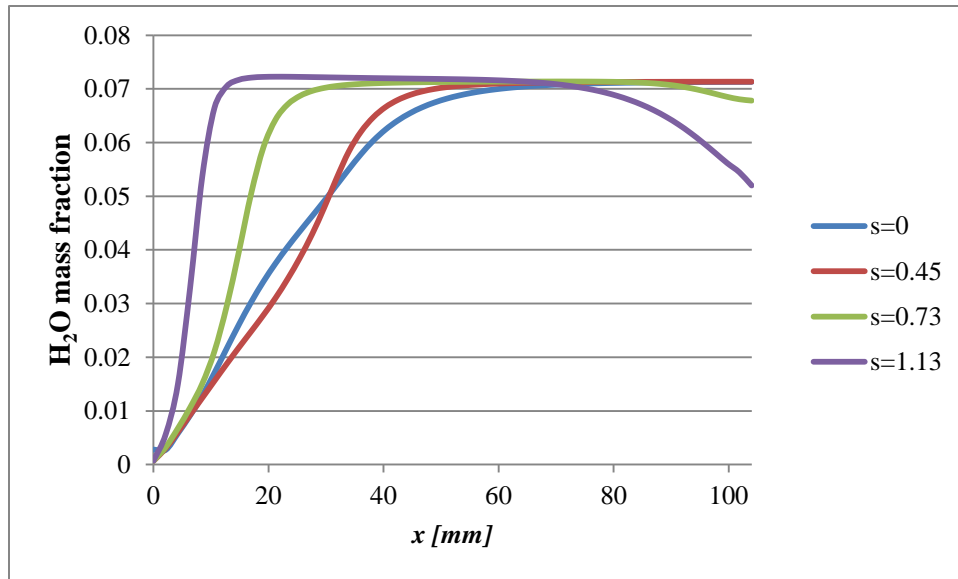


Figure 5-35 H₂O mass fraction along (x-x) line at $\phi=0.7$, $L/L_0 = 0$ and various swirl numbers.

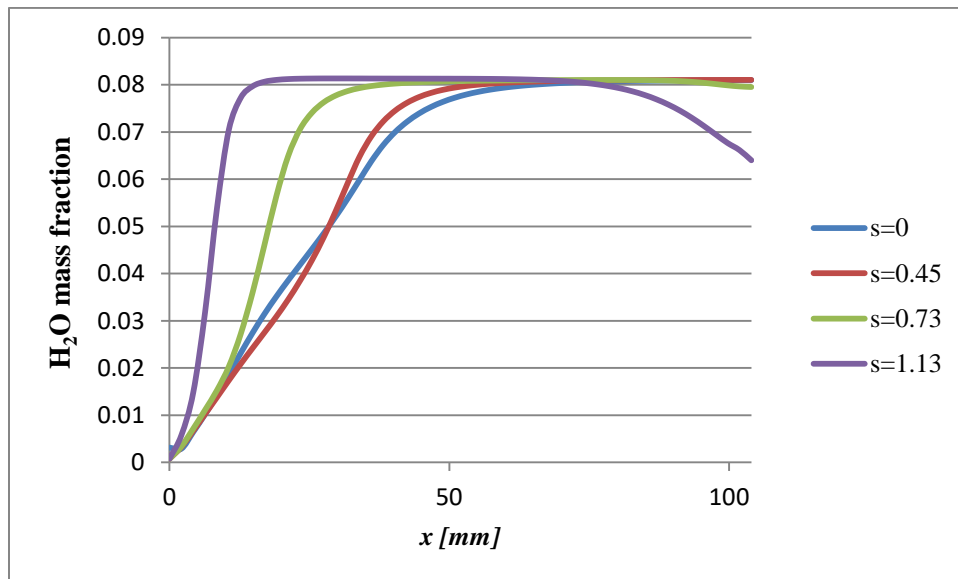


Figure 5-36 H₂O mass fraction along (x-x) line at $\phi=0.8$, $L/L_0 = 0$ and various swirl numbers.

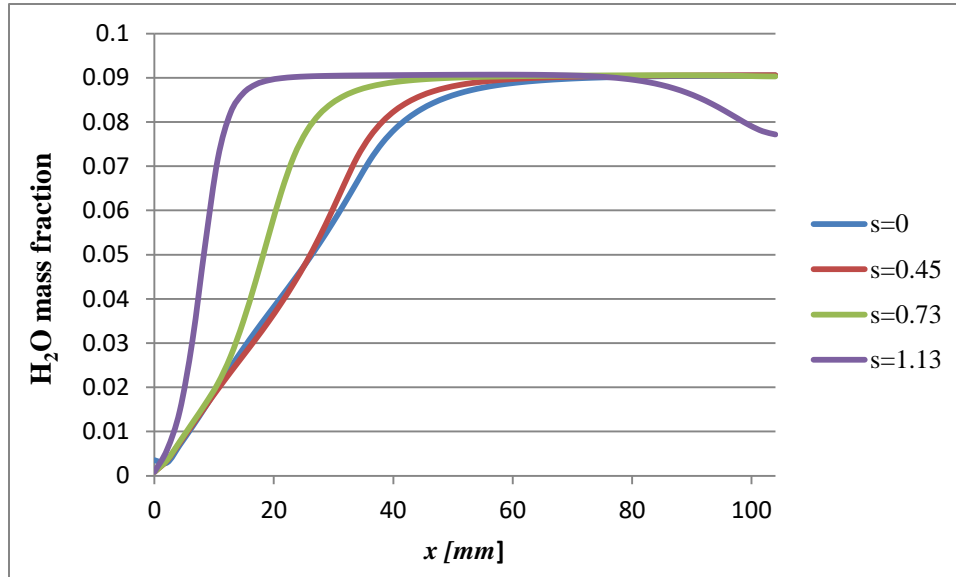


Figure 5-37 H₂O mass fraction along (x-x) line at $\phi=0.9$, $L/L_0 = 0$ and various swirl numbers.

The distributions of H₂O along (x-x) line at $\phi=0.7$, 0.8 and 0.9 are given for various swirl numbers in figures 5-35, 5-36 and 5-37, respectively. H₂O is the product of chemical combustion reaction, so the distribution H₂O of is directly related to the flame temperature gradient. As can be seen from these figures, the increase of swirl number leads to a faster consumption of oxygen. The results show that the increase of swirl number leads to decrease distance for production of H₂O to reach the maximum value. It is be clear from figure 5-32, 5-33 and 5-34, at equivalence ratio $\phi=0.7$, 0.8 and 0.9 respectively, the maximum values of H₂O fraction are located at around 80 mm, 70 mm, 57 mm and 25 mm for swirl number $s=0$, 0.45, 0.73 and 1.13, respectively. The maximum consumption values are 0.0714, 0.0806 and 0.0905 for equivalence ratio $\phi = 0.7$, 0.8 and 0.9 respectively.

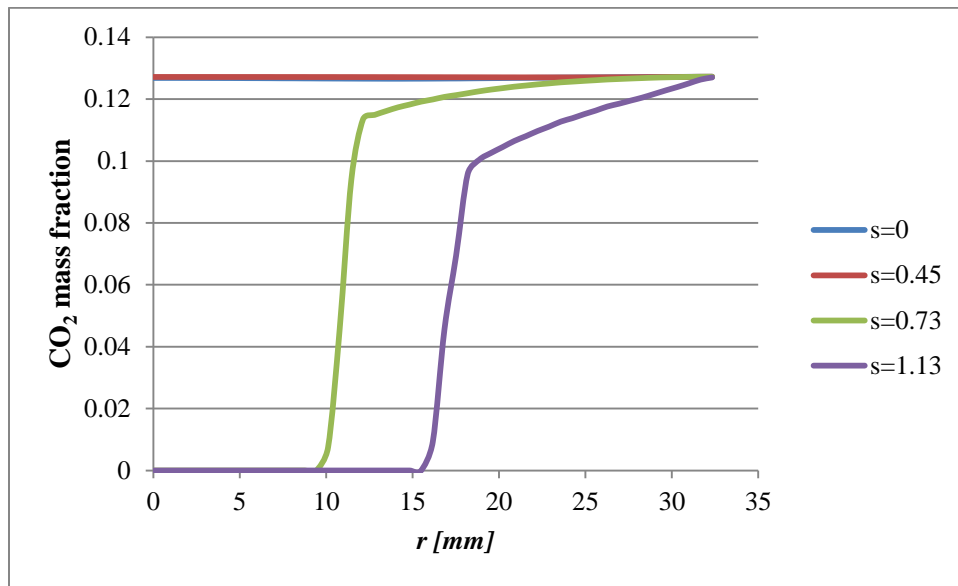


Figure 5-38 CO₂ mass fraction along radial line at outlet of combustor chamber for $\phi=0.7$, $L/L_0 = 0$ and various swirl numbers.

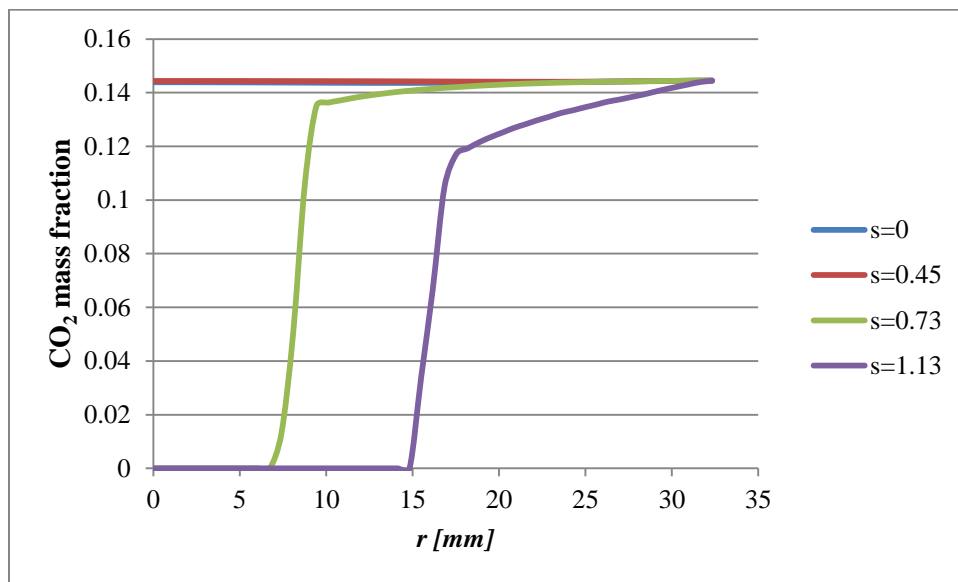


Figure 5-39 CO₂ mass fraction along radial line at outlet of combustor chamber for $\phi=0.8$, $L/L_0 = 0$ and various swirl numbers.

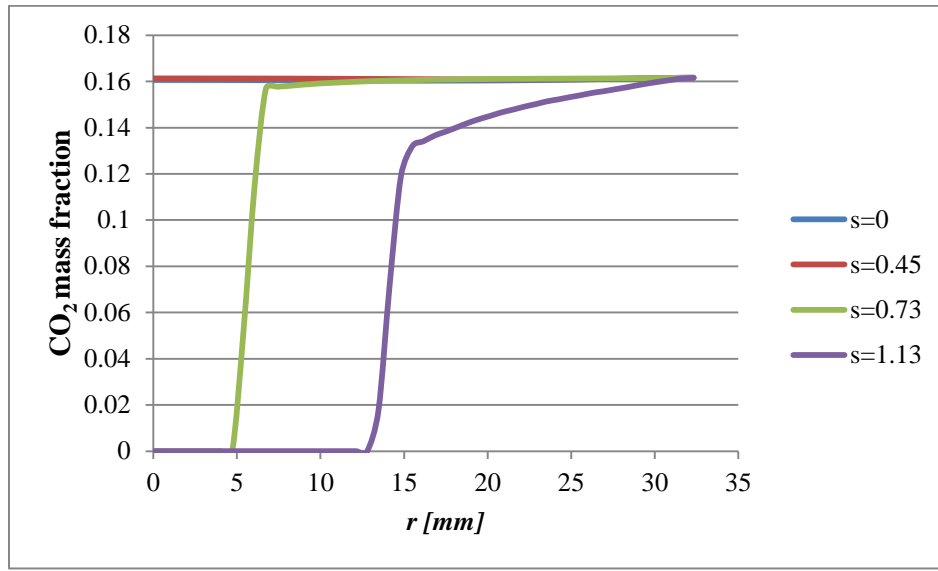


Figure 5-40 CO₂ mass fraction along radial line at outlet of combustor chamber for $\phi=0.9$, $L/L_0 = 0$ and various swirl numbers.

The distributions of CO₂ along the radial line at outlet of combustor chamber at $\phi=0.7$, 0.8 and 0.9 are given for various swirl numbers in figures 5-38, 5-39 and 5-40 respectively. CO₂ is the product of chemical combustion reaction. As can be seen from these figures, the distribution of mass fractions of CO₂ in cases of swirl numbers ($s = 0$ and $s = 0.45$) are almost the same. The CO₂ production values are 0.109, 0.126, 0.144 and 0.161 at equivalence ratios 0.6, 0.7, 0.8 and 0.9, respectively. The mass fraction distribution at lower swirl number ($s = 0$ and $s = 0.45$) cases are noticeably different from higher swirl numbers ($s = 0.73$ and $s = 1.13$). As shown in these figures, at equivalence ratio ($\phi=0.7$) there is CO₂ in range of $r \geq 10$ mm and $r \geq 16$ mm for $s = 0.45$ and $s = 1.13$ respectively, while at equivalence ratio ($\phi = 0.8$), the distribution of CO₂ appears in range of $r \geq 7.5$ mm and $r \geq 15$ mm for $s = 0.45$ and $s = 1.13$ respectively, also at equivalence ratio ($\phi = 0.9$), the CO₂ production concentrates in range of $r \geq 5.5$ mm and $r \geq 13.5$ mm for $s = 0.45$ and $s = 1.13$ respectively. To explain the effect of swirl number on CO₂ production, the average mass fraction of CO₂ has to be calculated at the outlet of combustor, so the figure 5-40 shows average mass fractions of CO₂ at the outlet, for different equivalence ratios and swirl numbers.

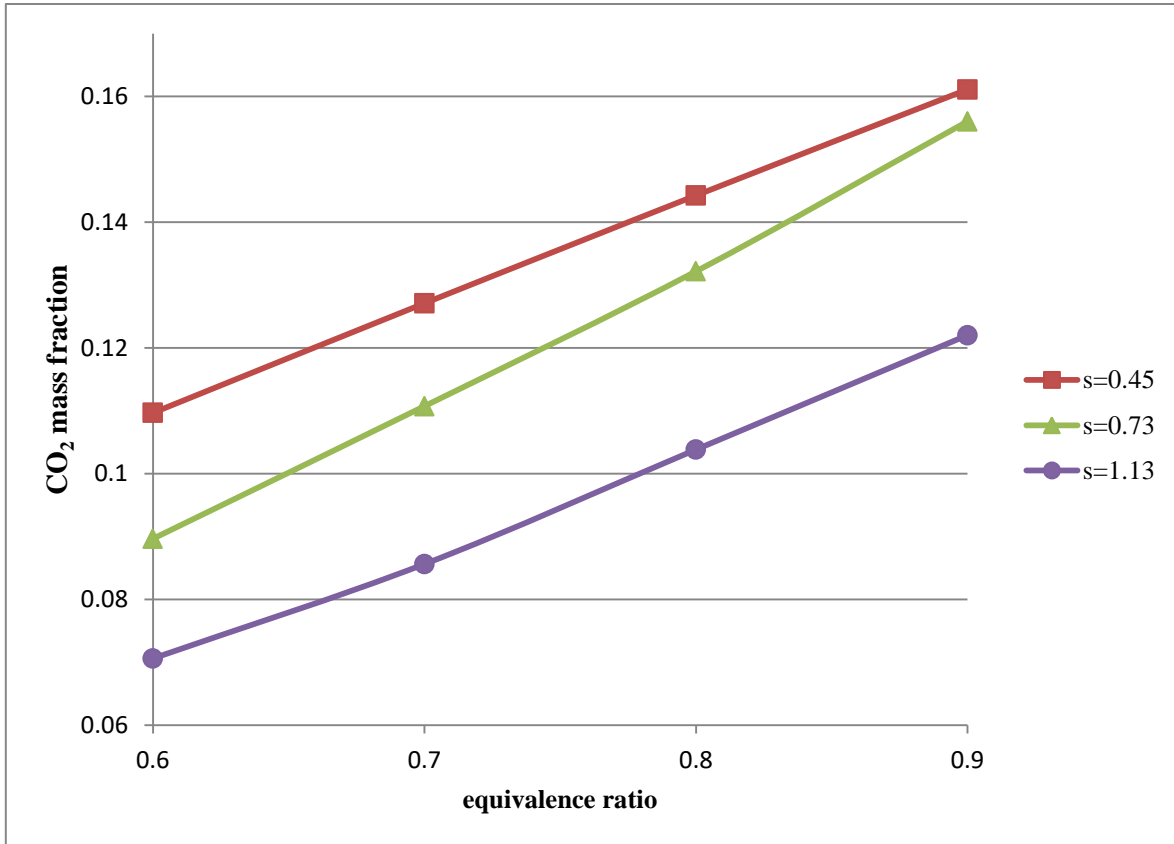


Figure 5-41 Average mass fractions of CO₂ at outlet for different equivalence ratios and swirl numbers of base fuel/hydrogen mixture ($L/L_0 = 0$).

As shown from figure 5-41, it can be clearly seen that the increase of swirl number leads to decreases the production of CO₂ at the outlet of the combustion chamber.

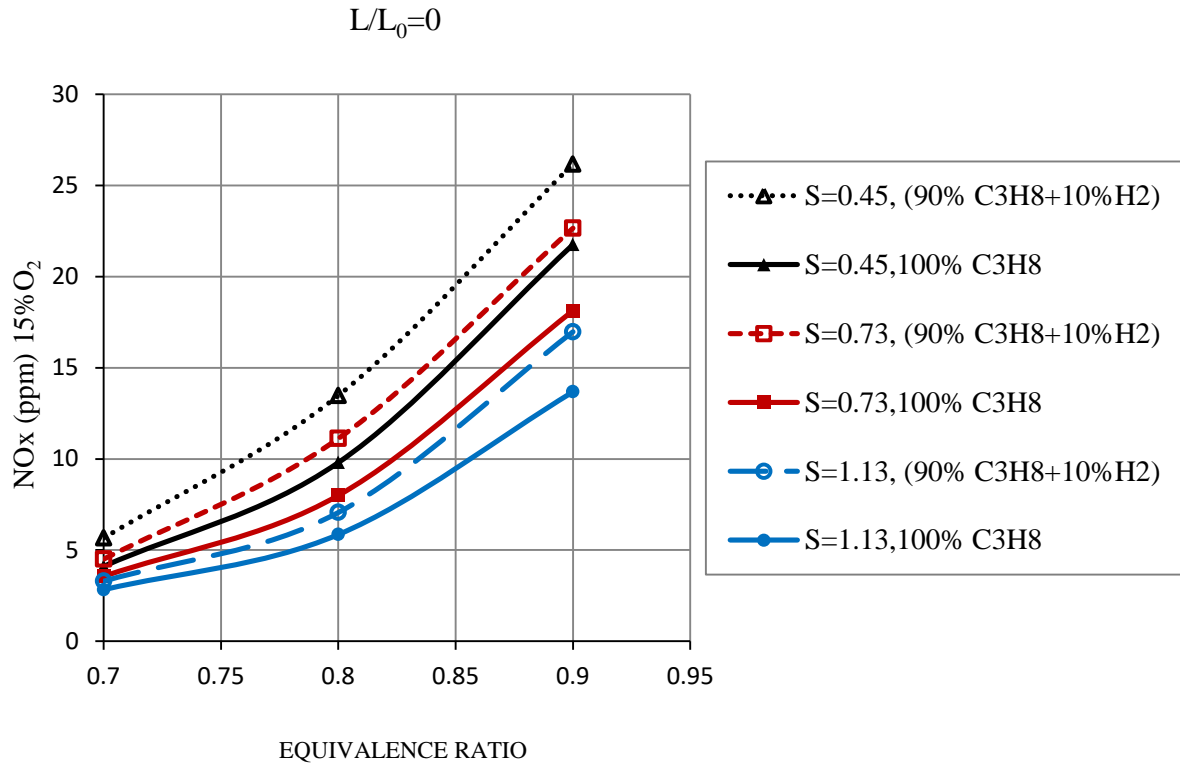


Figure 5-42 NOx emission for different equivalence ratios and swirl numbers of base fuel and b/hydrogen mixture.

Fig. 5-42 illustrates the variation of NOx emissions for different equivalence ratios and swirl numbers when using pure propane and mixture of propane and hydrogen (90% C₃H₈+10% H₂ vol.). The comparison of NOx emission without and with hydrogen addition, is based on experimental investigation data of the burner in question fueled with propane, [40]. It can be clearly seen that the addition of hydrogen to propane increases the NOx emissions. This effect is smaller at lower equivalence ratios and increases with the increase of equivalence ratio. The maximum increase of NOx takes place at equivalence ratio $\Phi = 0.9$ for all cases of swirl numbers.

5.2 Conclusion

A numerical analysis of combustion of premixed base fuel-air and base fuel/10%vol hydrogen-air mixture was conducted.

The thesis provides some new insights in lean premixed turbulent combustion of hydrocarbon fuel blends with hydrogen in a swirl combustor with and without center body.

The velocity field, temperature, reaction rates, species concentrations and NO_x emissions of base fuel and base fuel-10%vol hydrogen mixture were calculated over the range of equivalence ratios and swirl numbers for tubular and annular swirl combustors.

Numerical results show that combustion characteristics such as the radial temperature, axial temperature distributions, the gas concentrations including CH₄, H₂, C₃H₈, O₂, H₂O and CO₂ and other products are strongly affected by the swirl number and equivalence ratio.

The flow structure, central recirculation zone (CRZ) and wall recirculation zones (WRZ) for the two types of combustor were found to differ significantly.

For flows with no swirl the flame is elongated, narrow, and protrudes out of the combustor. The increase of swirl number moves flame closer to the combustor inlet. Flame becomes wider, shorter and completely inside the combustor, for both fuels due to the strong flow recirculation induced by increased swirl.

The most pronounced difference between flames of base fuel and base fuel/hydrogen mixture can be seen for the highest swirl, $S = 1.13$: The flame of fuel/hydrogen mixture is shorter and more compact than that of pure fuel. This can be attributed to the increase of flame speed of blended fuel.

The reaction rates of blended fuel increase with the increase of swirl number, with pronounced peak for highest swirl, $S = 1.13$. A noticeable difference between base fuel and the hydrogen enriched fuel is faster consumption of hydrogen.

Very good agreement between calculated and experimental NO_x emissions has been found. The addition of 10% vol of hydrogen into base fuel increases the NO_x emission by about 20% for equivalence ratio 0.9, and about 30% for equivalence ratio 0.9. The increase of swirl number from $S = 0.45$ to 1.13 lowers the NO_x emission between 30-40% for both fuels.

Possible problem of flame flashback in existing combustion devices is of minor importance because the increase of flame speed of methane to methane-10%vol hydrogen mixture is about 4 cm/s for the stoichiometric mixtures.

The results of the thesis can be useful to researchers, combustion equipment manufacturers and engineers, dealing with combustion devices such as burners, combustors, gas turbines and other combustion systems.

References

- [1] International energy agency (IEA), OECD/IEA, 2015. www.iea.org/t&c.
- [2] IPCC, "The IPCC Assessment Reports ", <http://www.ipcc.ch/>.
- [3] Wall, T. F., 2007, "Combustion processes for carbon capture," Proceedings of the Combustion Institute, 31(1), pp. 31-47.
- [4] Cho, H. M., and He, B. Q., 2007, "Spark ignition natural gas engines-A review," Energy Conversion and Management, 48(2007), pp. 608-618.
- [5] Shelil, N., 2007, "Boiler Types and Burner Systems," Cardiff University, Cardiff.
- [6] Wu L, Kobayashi N, Li Z, Hung H. Experimental study on the effect of hydrogen addition on the emission and heat transfer characteristic of laminar methane diffusion flames with oxygen-enriched air. Int J Hydrogen Energy 2016, 41:2023-2036
- [7] Point T, Veynante D. Theoretical and numerical combustion. Philadelphia, USA Edwards; 2005
- [8] Najjar, Yousef SH. "Gaseous pollutants formation and their harmful effects on health and environment." Innovative energy policies 1 (2011): 1-9.
- [9] Tang, Chenglong, Yingjia Zhang, and Zuohua Huang. "Progress in combustion investigations of hydrogen enriched hydrocarbons." Renewable and Sustainable Energy Reviews 30 (2014): 195-216.
- [10] Nanthagopal, Kasianantham, Rayapati Subbarao, Thangavelu Elango, Ponnusamy Baskar, and Kandasamy Annamalai. "Hydrogen enriched compressed natural gas (HCNG): A futuristic fuel for internal combustion engines." Thermal Science 15, no. 4 (2011): 1145-1154.
- [11] Ni, Meng, Michael KH Leung, K. Sumathy, and Dennis YC Leung. "Potential of renewable hydrogen production for energy supply in Hong Kong." International Journal of Hydrogen Energy 31, no. 10 (2006): 1401-1412.
- [12] Tabone, Michaelangelo D., Christoph Goebel, and Duncan S. Callaway. "The effect of PV siting on power system flexibility needs." Solar Energy 139 (2016): 776-786.

- [13] Riis, T., E. F. Hagen, G. Sandrock, P. J. S. Vie, and O. Ulleberg. "Hydrogen Production and Storage, International Energy Agency: Paris, 2006."
- [14] Chen, Haisheng, Thang Ngoc Cong, Wei Yang, Chunqing Tan, Yongliang Li, and Yulong Ding. "Progress in electrical energy storage system: A critical review." *Progress in Natural Science* 19, no. 3 (2009): 291-312.
- [15] Morales, Tania Carbonell, Victor Roca Oliva, and Leyat Fernández Velázquez. "Hydrogen from Renewable Energy in Cuba." *Energy Procedia* 57 (2014): 867-876.
- [16] Levene, Johanna Ivy, Margaret K. Mann, Robert M. Margolis, and Anelia Milbrandt. "An analysis of hydrogen production from renewable electricity sources." *Solar Energy* 81, no. 6 (2007): 773-780.
- [17] Melaina, M., and J. Eichman. *Hydrogen Energy Storage: Grid and Transportation Services*. Technical Report NREL/TP-5400-62518, www.nrel.gov/publications, February 2015.
- [18] Melaina, Marc W., Olga Antonia, and Mike Penev. "Blending hydrogen into natural gas pipeline networks: a review of key issues." Technical Report NREL/TP-5400-62518, www.nrel.gov/publications, March 2013
- [19] Altfeld, Klaus, and Dave Pinchbeck. "Admissible hydrogen concentrations in natural gas systems." *Gas for energy* 3 (2013): 2013, www.gas-for-energy.com
- [20] Dutka, Marcin, Mario Ditaranto, and Terese Løvås. "Emission characteristics of a novel low NO_x burner fueled by hydrogen-rich mixtures with methane." *Journal of Power Technologies* 95, no. 2 (2015): 105-111
- [21] Guo, Hongsheng, Gregory J. Smallwood, Fengshan Liu, Yiguang Ju, and Ömer L. Gülder. "The effect of hydrogen addition on flammability limit and NO_x emission in ultra-lean counterflow CH₄/air premixed flames." *Proceedings of the combustion institute* 30, no. 1 (2005): 303-311.
- [22] Therkelsen, Peter, Tavis Werts, Vincent McDonnell, and Scott Samuelson. "Analysis of NO_x formation in a hydrogen-fueled gas turbine engine." *Journal of Engineering for Gas Turbines and Power* 131, no. 3 (2009): 031507.
- [23] Choudhuri, A., and S. R. Gollahalli. "Combustion Characteristics of Hydrogen-Propane Mixture." *AIAA Journal of Propulsion and Power* 19 (2003): 107-112.

- [24] Syred N, Abdulsada M. Griffiths A. O'Doherty T. Bowen P. the effect of hydrogen containing fuel blends upon flashback in swirl burners. *Applied Energy* (2012)89:106-110
- [25] Kim HS. Rhode VK, Link MB, Gupta AK. hydrogen addition effects in confined swirl-stabilized methane-air flame. *Int J Hydrogen energy* 2009; 34:1054-1062
- [26] Roberto M. pollutant emission validation of a heavy-duty gas turbine burner by CFD modeling. *Machines* 2013, 1, 81-97
- [27] Launder BE, Spalding DB. *Lectures in mathematical models of turbulence*. London, UK; Academic press; 1972.
- [28] Sharif MAR, Wong YKE. Evaluation of the performance of three turbulence closure models in the prediction of confined swirling flows. *Comput. Fluids* 1995; 24:81-100
- [29] Shih TH, Liou WW, Shabbir A, Yang Z, Zhu J, A new k-eddy-viscosity model for high Reynolds number turbulent flows. *Comput. Fluids* 1995; 24:227-238
- [30] Adel Gayed HM , Abdelghaffar WA, El Shorbagy K. Main flow characteristics in a lean premixed swirl stabilized gas turbine combustor – numerical computation. *Am J Sci Ind Res* 2003;4:123-136
- [31] Zakaria M., Mokhtar A. Toufik b., numerical computation of premixed propane flame in a swirl-stabilized burner: effects of hydrogen enrichment, swirl number and equivalence ratio on flame characteristics
- [32] Weibo Chen and Guixiong Liu. Numerical Investigation on the Flow, Combustion and NOx Emission Characteristics in a 10 MW Premixed Gas Burner. *The Open Fuels & Energy Science Journal*, 2015, 8, 1-13
- [33] Magnussen BF, Hjertager BH. On mathematical modeling of turbulent combustion with special emphasis on soot formation and combustion. *Proc Combust Inst* 1977;16:719-729]
- [34] Ilker Yilmaz. Effect of swirl number on combustion characteristics in a natural gas diffusion flame. *Energy resources technology*. 2013;135: 042204-1
- [35] De. A, Oldenhof E, Sathiah P, Roekaerts D. numerical simulation of delft-jet in hot coflow flames using the eddy dissipation concept model for turbulence-chemistry interaction. *Flow Turb Combust* 2011;87:537-567]

- [36] Nogenmyr KJ, Furebyb C, Bai XS, Petersson P, Collin R, Linne M. large eddy simulation and laser diagnostic studies on a low swirl stratified premixed flame. *Combust Flame* 2009;156:25-36.
- [37] Li S, Zheng Y, Martinez DM, Zhua M, Jiang X. Large-eddy simulation of flow and combustion dynamics in a lean partially-premixed swirling combustion. *Energy Proc* 2015;66:333-336
- [38] Ilbas M. The effect of thermal radiation and radiation models on hydrogen-hydrocarbon combustion modeling. *Int J Hydrogen Energy* 2005;30:1113-1126
- [39] Yilmaz et al. [Yilmaz I, Tastan M, Ilbas M, Tarhan C. Effect of turbulence and radiation models on combustion characteristics in propane-hydrogen diffusion flames. *Energy Convers Manage* 2013;72:179-186
- [40] M. Adzic, V.F, A.M, M.Z, "Effect of a Microturbine Combustor Type on Emissions at Lean-Premixed Conditions," *Journal of propulsion and power*, Vol.26, No.5, September-October 2010, pp. 1135-1143.
- [41] www.ansys.com
- [42] Versteeg, H. K., and Malalasekera, W., 1995, *An Introduction to Computational Fluid Dynamics — The Finite Volume Method*, Longman Group Ltd.
- [43] Löhner, Rainald. *Applied computational fluid dynamics techniques: an introduction based on finite element methods*. John Wiley & Sons, 2008.
- [44] Versteeg, H. K., and Malalasekera, W., 1995, *An Introduction to Computational Fluid Dynamics — The Finite Volume Method*, Longman Group Ltd.
- [45] Sayma, A., 2009, *Computational Fluid Dynamics*, Ventus Publishing ApS.
- [46] Fluent, A. N. S. Y. S. "Theory guide." US: ANSYS Inc (2009).
- [47] "Finite volume method." [http://www.cfd-online.com/Wiki/Finite volume](http://www.cfd-online.com/Wiki/Finite_volume).

APPENDIX

Some results are given in the Appendix in order to get better insight of the effects of variables for the base fuel with 10% vol hydrogen.

Figs. A-1 to A-17 present detailed velocity field distributions. Figs. A-18 to A-21 present mass fraction of fuel and A-22 to A-24 mass fraction of hydrogen in flame. The figures clearly show that the rate of consumption of hydrogen is significantly higher than that of the

base fuel. Figs. A-25 to A-35 show mass fraction distribution of O_2 , H_2O and CO_2 .

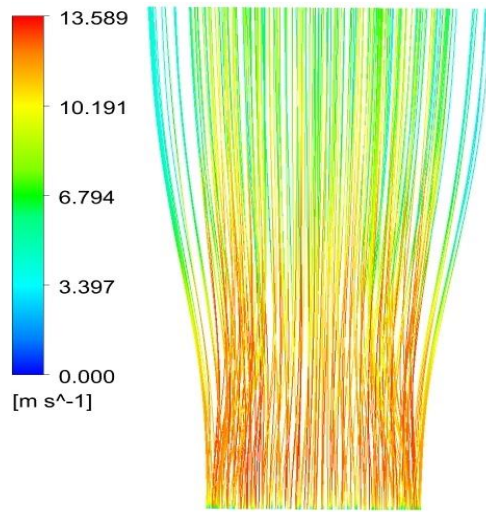


Fig. A-1 3D streamlines of combustion gases at $\phi=0.8$, $L/L_0=0$ and $s=0$.

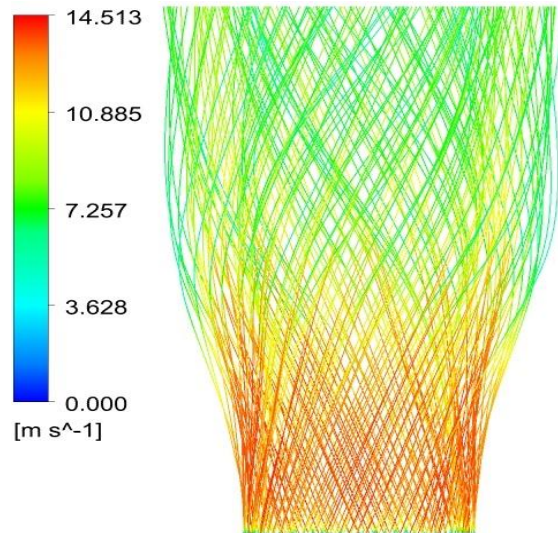


Fig. A-2 3D streamlines of combustion gases at $\phi=0.8$, $L/L_0=0$ and $s=0.45$.

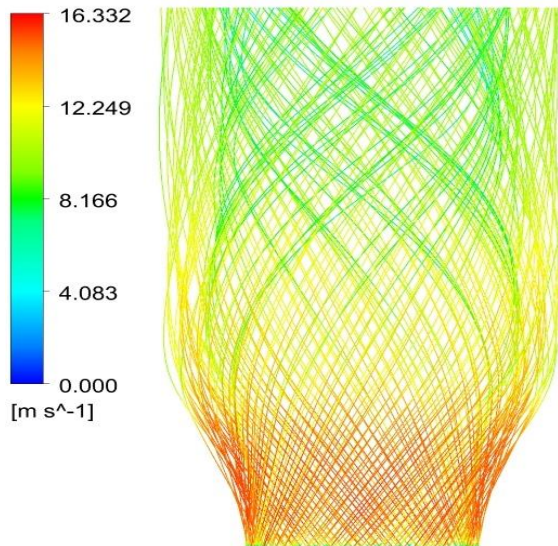


Fig. A-3 3D streamlines of the flow at $\phi=0.8$, $L/L_0=0$ and $s=0.73$.

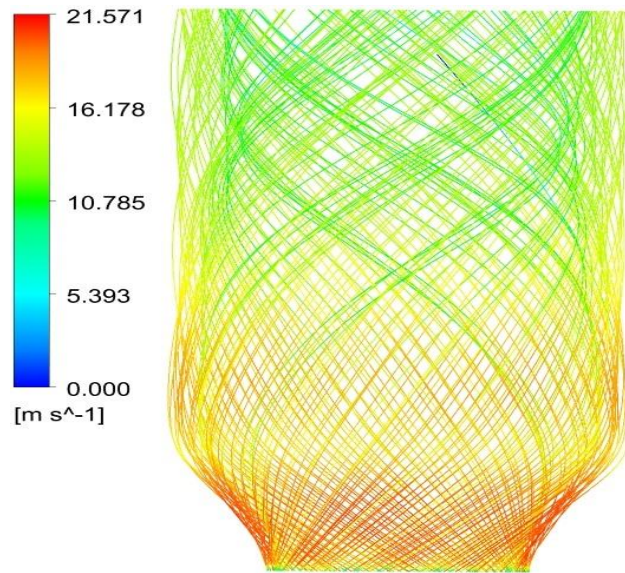


Fig. A-4 3D streamlines of the flow at $\phi=0.8$, $L/L_0=0$ and $s=1.13$.

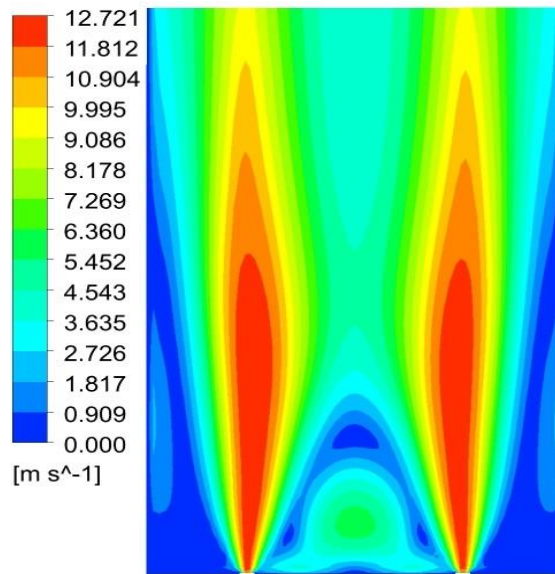


Fig. A-5 Contours of velocity distribution along the central plane for $\Phi = 0.8$, $L/L_0=0$ and $s=0$.

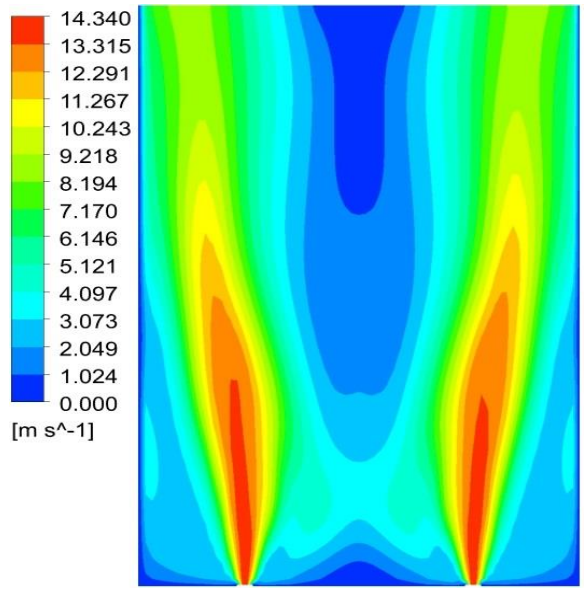


Fig. A-6 Contours of velocity distribution along the central plane for $\Phi = 0.8$, $L/L_0=0$ and $s=0.45$.

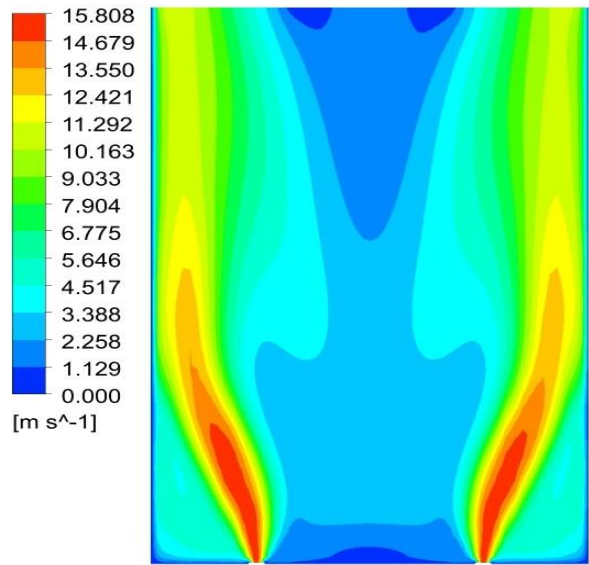


Fig. A-7 Contours of velocity distribution along the central plane for $\Phi = 0.8$, $L/L_0=0$ and $s=0.73$.

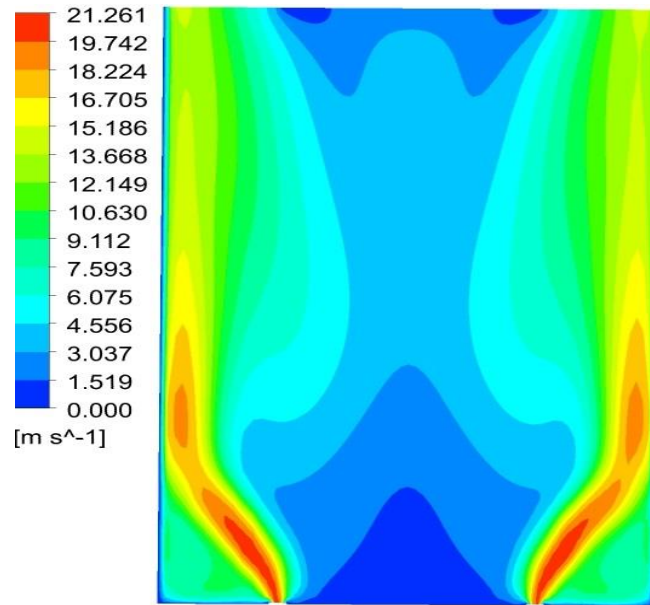


Fig. A-8 Contours of velocity distribution along the central plane for $\Phi = 0.8$, $L/L_0 = 0$ and $s = 1.13$.

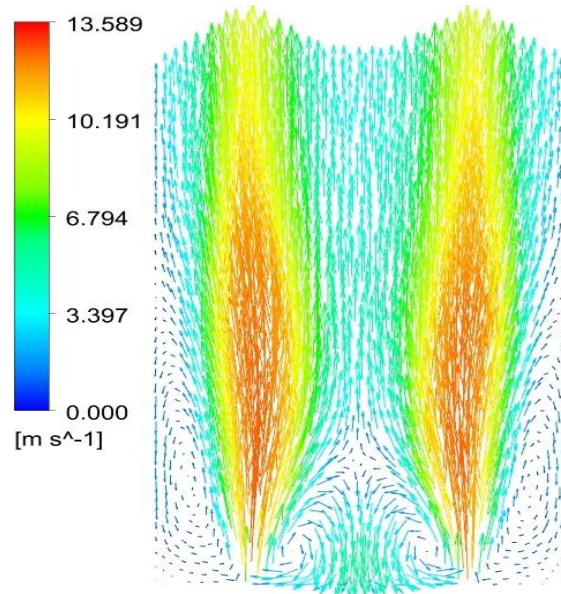


Fig. A-9 Contours of velocity vectors along the central plane for $\Phi = 0.8$, $L/L_0 = 0$ and $s = 0$.

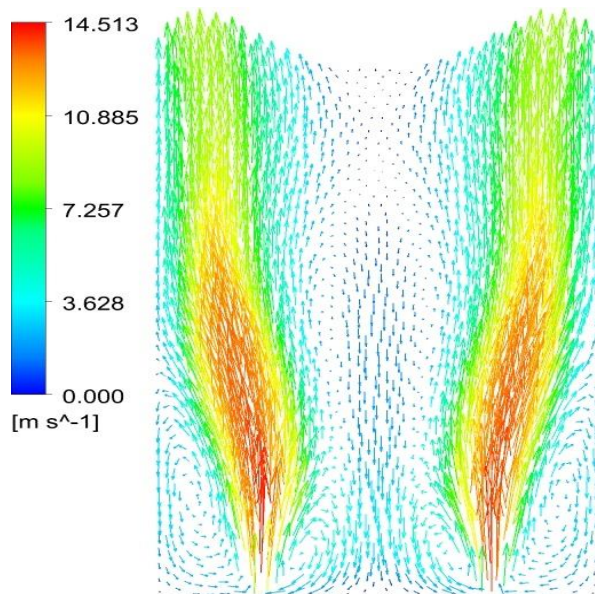


Fig. A-10 Contours of velocity vectors along the central plane for $\Phi = 0.8$, $L/L_0 = 0$ and $s = 0.45$.

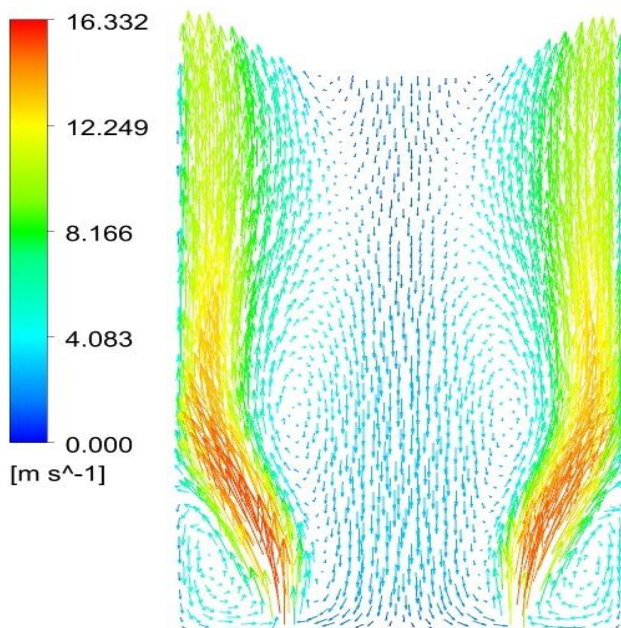


Fig. A-11 Contours of velocity vectors along the central plane for $\Phi = 0.8$, $L/L_0 = 0$ and $s = 0.73$.

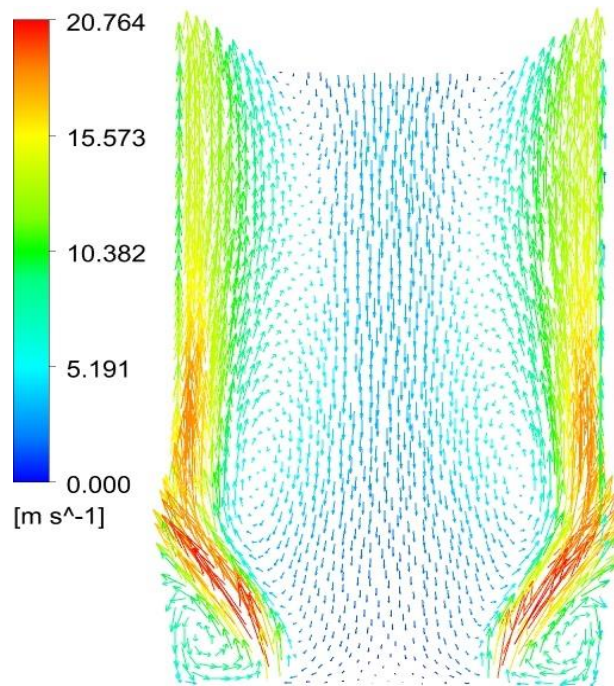


Fig. A-12 Contours of velocity vectors along the central plane for $\Phi = 0.8$, $L/L_0 = 0$ and $s = 1.13$.

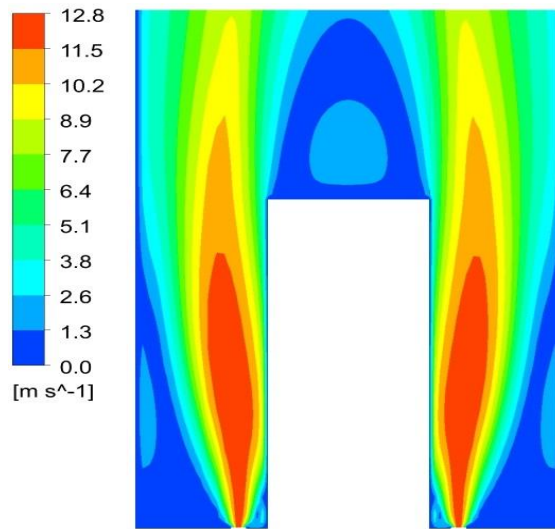


Fig. A-13 Contours of velocity along the central plane for $\Phi = 0.8$, $L/L_0 = 1$ and $s = 0$.

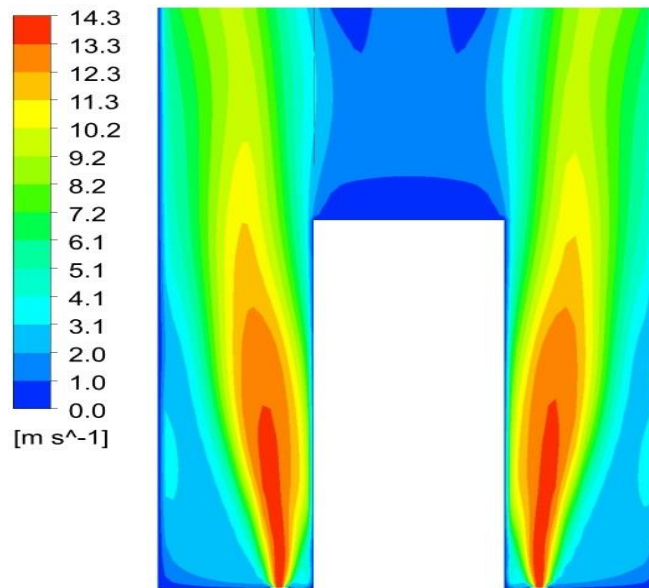


Fig. A-14 Contours of velocity along the central plane for $\Phi = 0.8$, $L/L_0 = 1$ and $s = 0.45$.

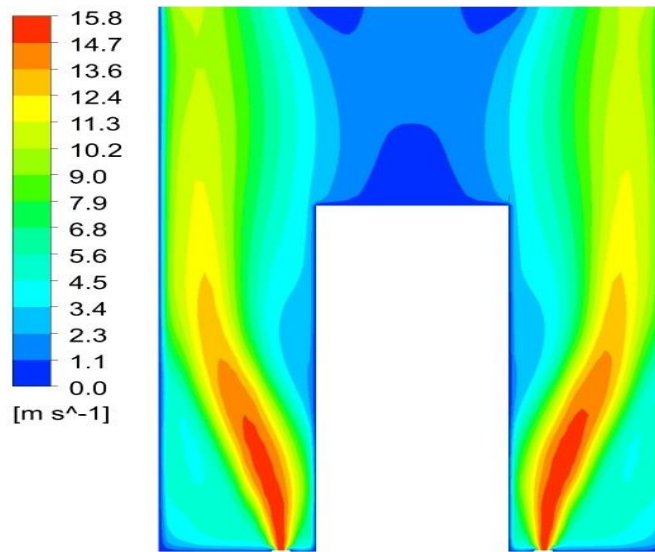


Fig. A-15 Contours of velocity distribution along the central plane for $\Phi = 0.8$, $L/L_0 = 1$ and $s = 0.73$.

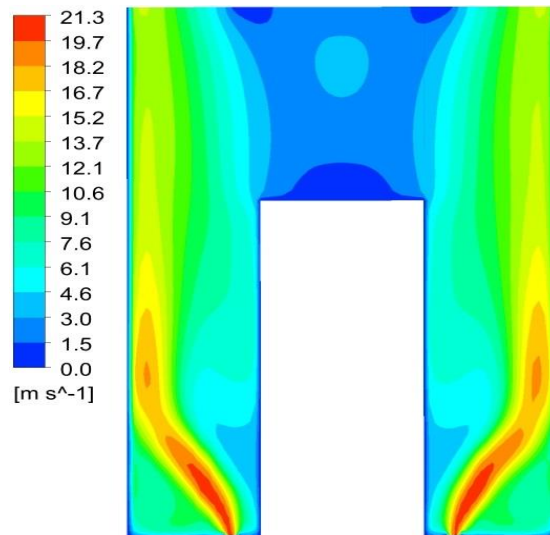


Fig. A-16 Contours of velocity distribution along the central plane for $\Phi = 0.8$, $L/L_0 = 1$ and $s = 1.13$.

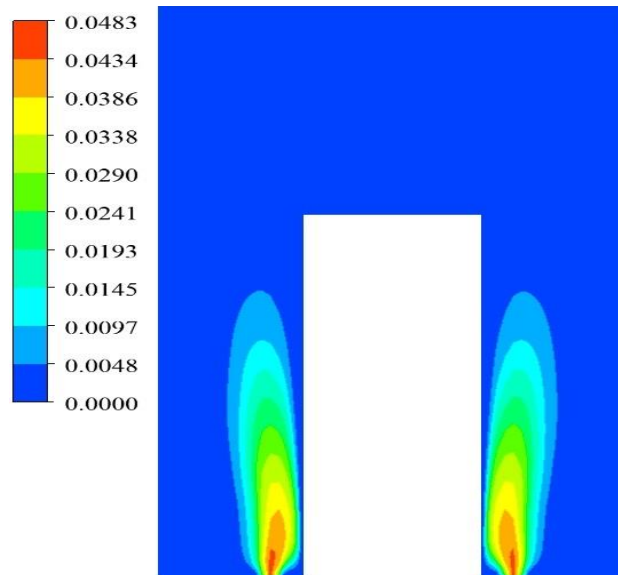


Fig. A-17 Contours of base fuel mass fraction along the central plane for $\Phi = 0.8$, $L/L_0 = 1$ and $s = 0$.

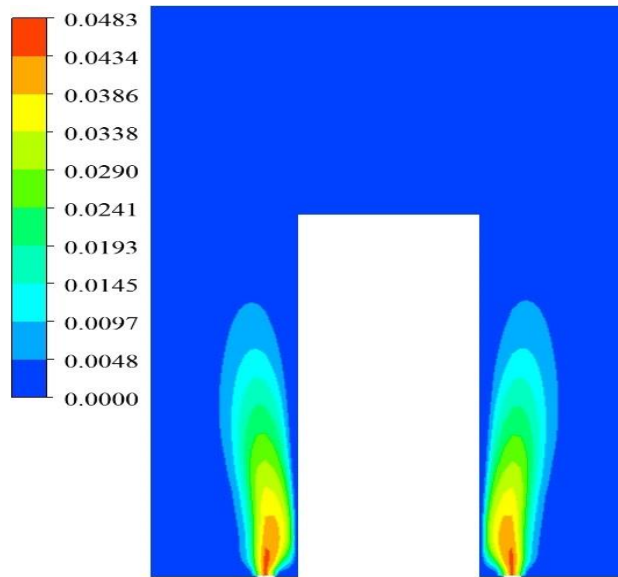


Fig. A-18 Contours of base fuel mass fraction along the central plane for $\Phi = 0.8$, $L/L_0=1$ and $s=0.45$.

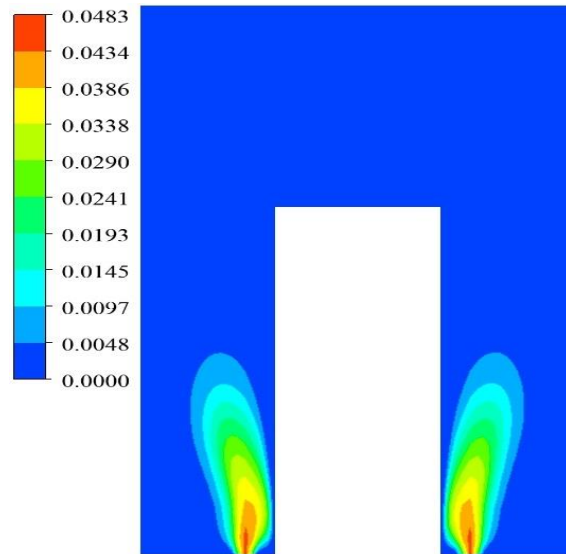


Fig. A-19 Contours of base fuel mass fraction along the central plane for $\Phi = 0.8$, $L/L_0=1$ and $s=0.73$.

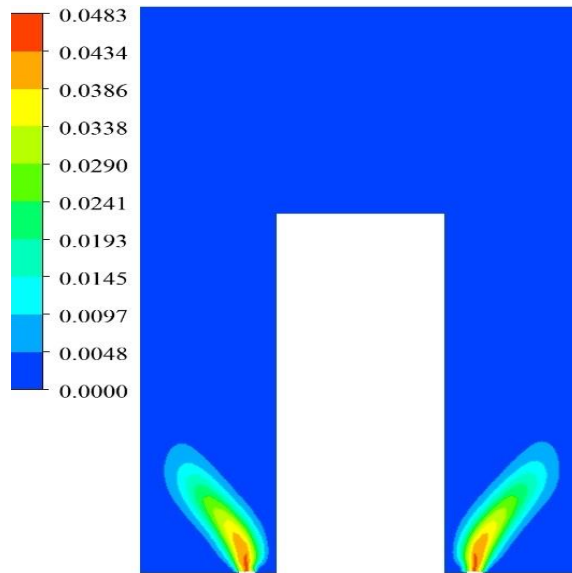


Fig. A-20 Contours of base fuel mass fraction along the central plane for $\Phi = 0.8$, $L/L_0 = 1$ and $s = 1.13$.

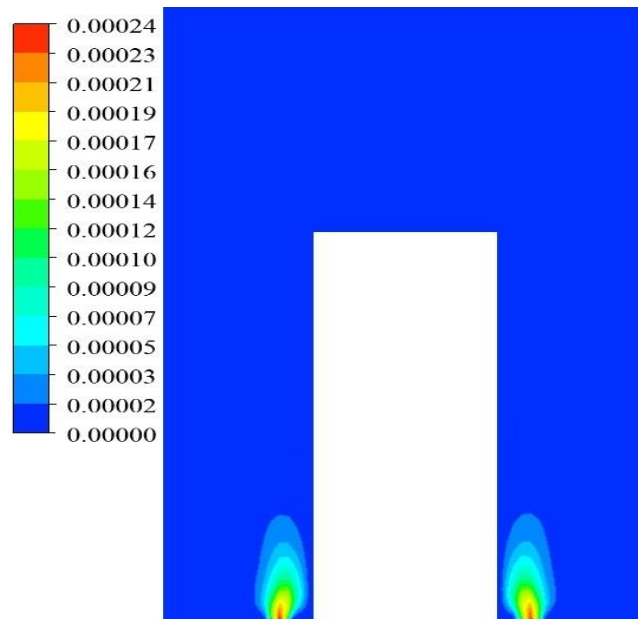


Fig. A-21 Contours of H₂ mass fraction along the central plane for $\Phi = 0.8$, $L/L_0 = 1$ and $s = 0$.

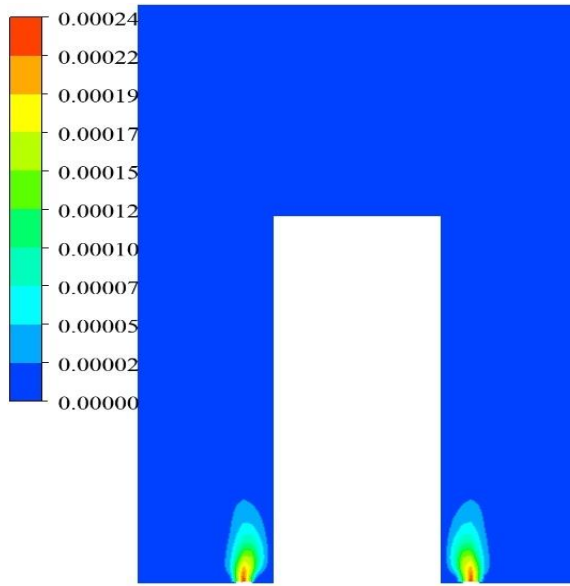


Fig. A-22 Contours of H₂ mass fraction along the central plane for $\Phi = 0.8$, $L/L_0=1$ and $s=0.45$.

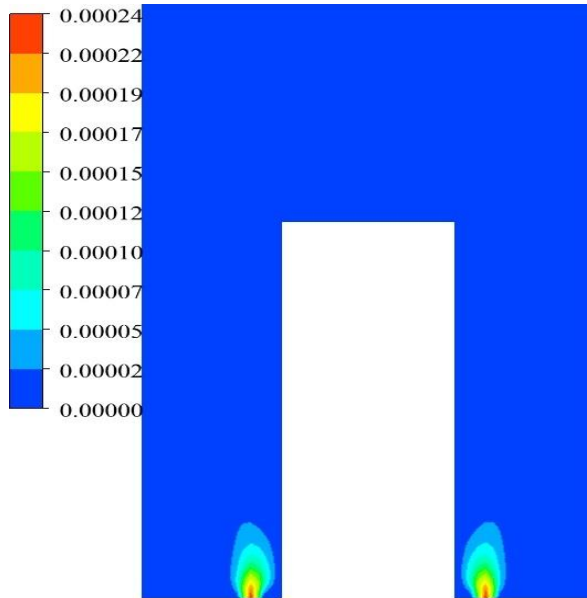


Fig. A-23 Contours of H₂ mass fraction along the central plane for $\Phi = 0.8$, $L/L_0=1$ and $s=0.73$.

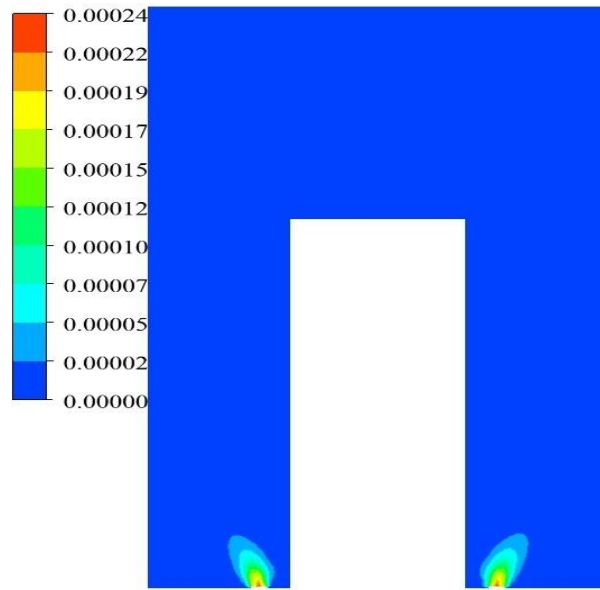


Fig. A-24 Contours of H₂ mass fraction along the central plane for $\Phi = 0.8$, $L/L_0 = 1$ and $s = 1.13$.

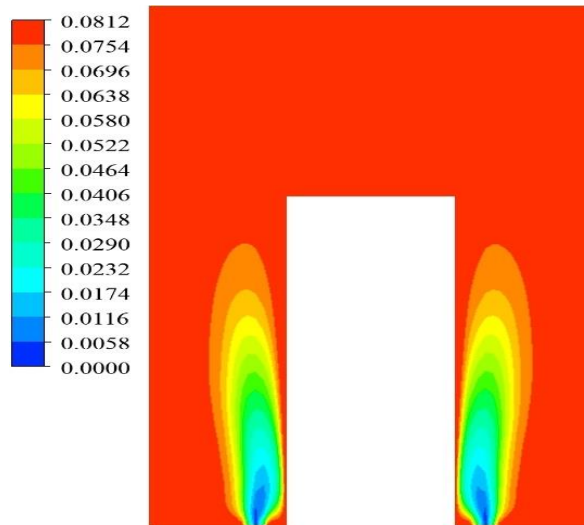


Fig. A-25 Contours of H₂O mass fraction along the central plane for $\Phi = 0.8$, $L/L_0 = 1$ and $s = 0$.

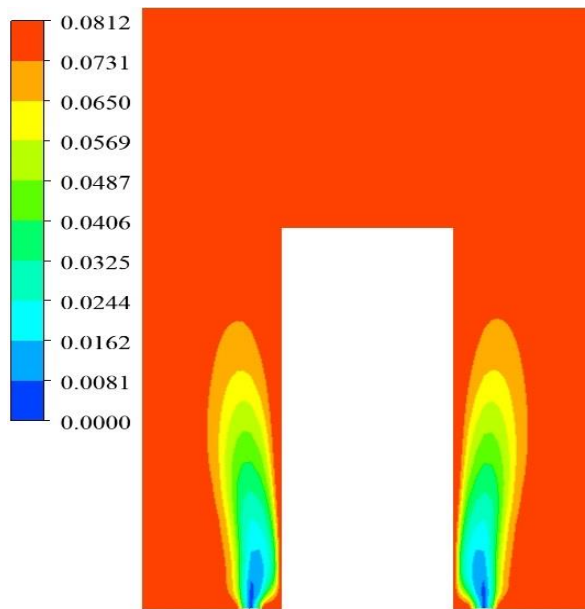


Fig. A-26 Contours of H₂O mass fraction along the central plane for $\Phi = 0.8$, $L/L_0=1$ and $s=0.45$.

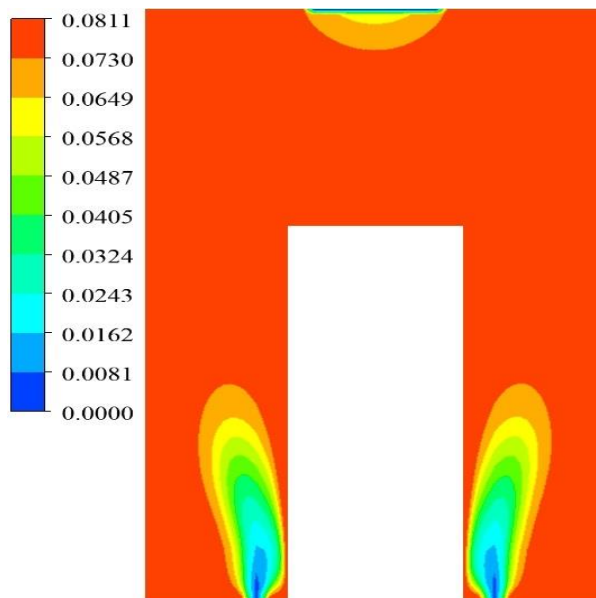


Fig. A-27 Contours of H₂O mass fraction along the central plane for $\Phi = 0.8$, $L/L_0=1$ and $s=0.73$.

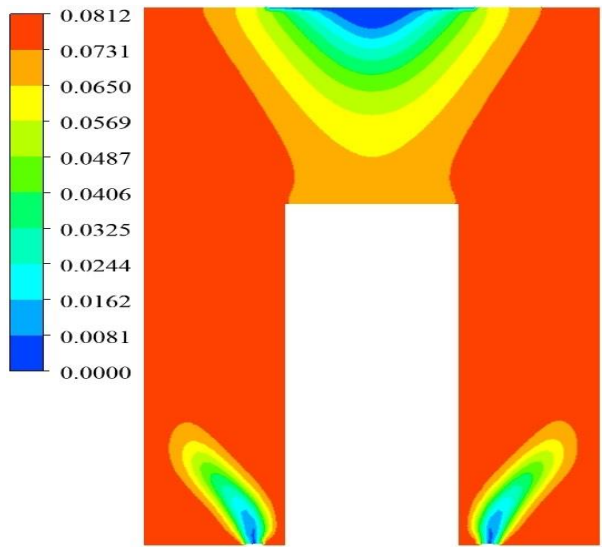


Fig. A-28 Contours of H₂O mass fraction along the central plane for $\Phi =0.8$, $L/L_0=1$ and $s=1.13$.

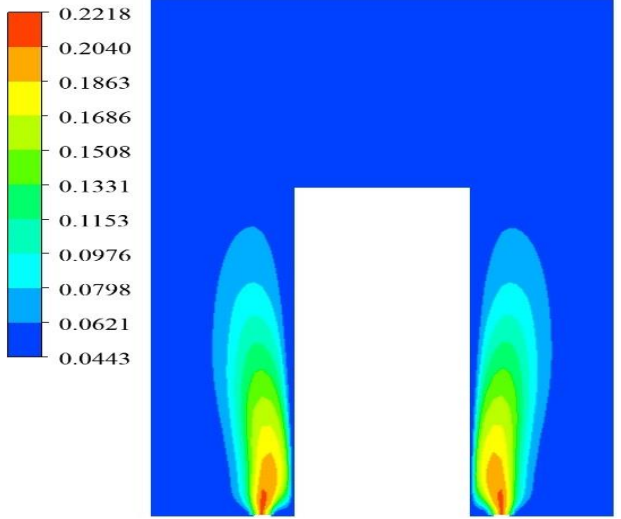


Fig. A-29 Contours of O₂ mass fraction along the central plane for $\Phi =0.8$, $L/L_0=1$ and $s=0$.

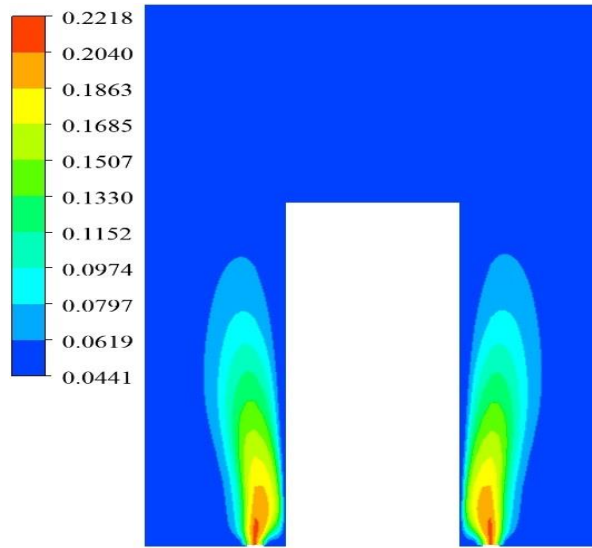


Fig. A-30 Contours of O₂ mass fraction along the central plane for $\Phi = 0.8$, $L/L_0 = 1$ and $s = 0.45$.

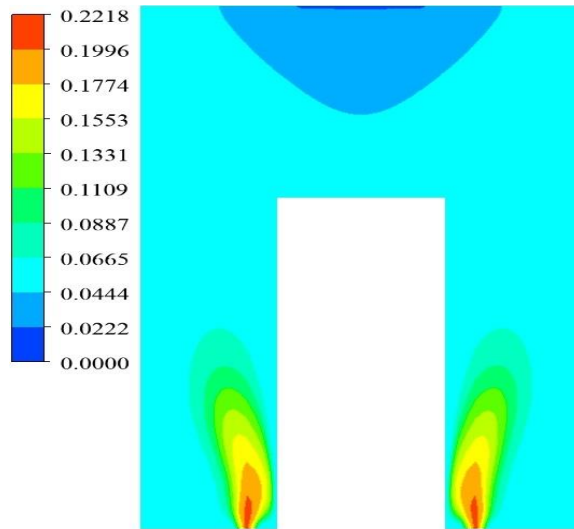


Fig. A-31 Contours of O₂ mass fraction along the central plane for $\Phi = 0.8$, $L/L_0 = 1$ and $s = 0.73$.

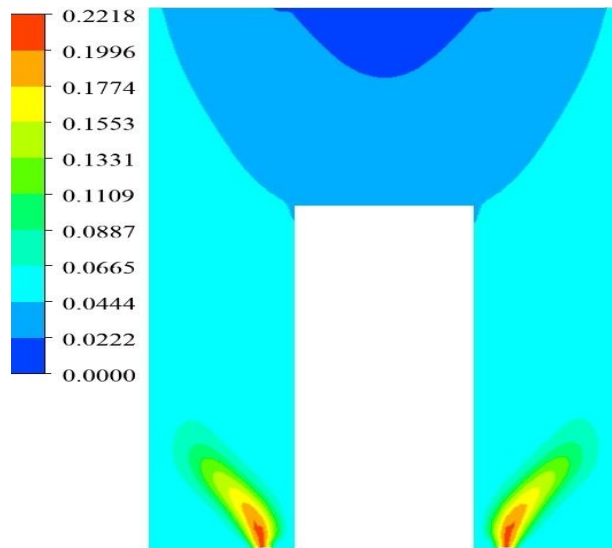


Fig. A-32 Contours of O_2 mass fraction along the central plane for $\Phi = 0.8$, $L/L_0 = 1$ and $s = 1.13$.

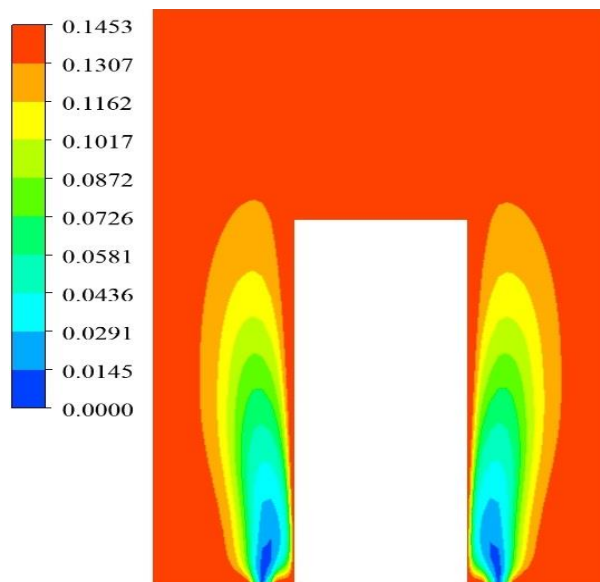


Fig. A-33 Contours of CO_2 mass fraction along the central plane for $\Phi = 0.8$, $L/L_0 = 1$ and $s = 0$.

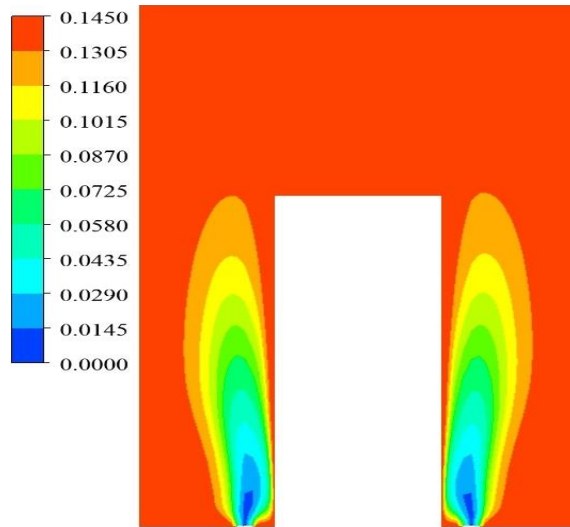


Fig. A-34 Contours of CO₂ mass fraction along the central plane for $\Phi = 0.8$, $L/L_0=1$ and $s=0.45$.

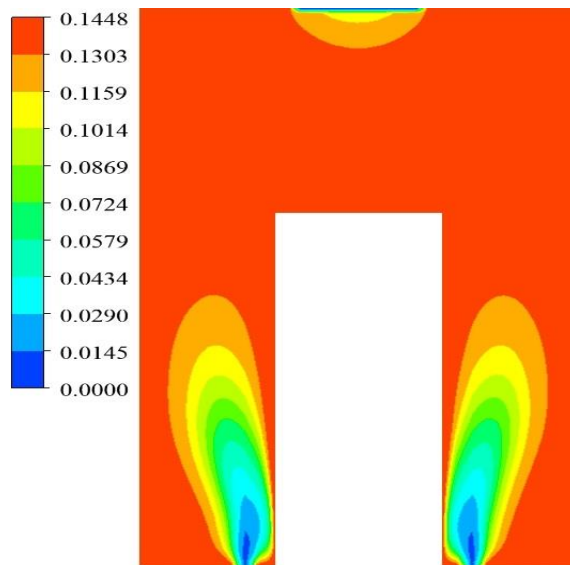


Fig. A-35 Contours of CO₂ mass fraction along the central plane for $\Phi = 0.8$, $L/L_0=1$ and $s=0.73$.

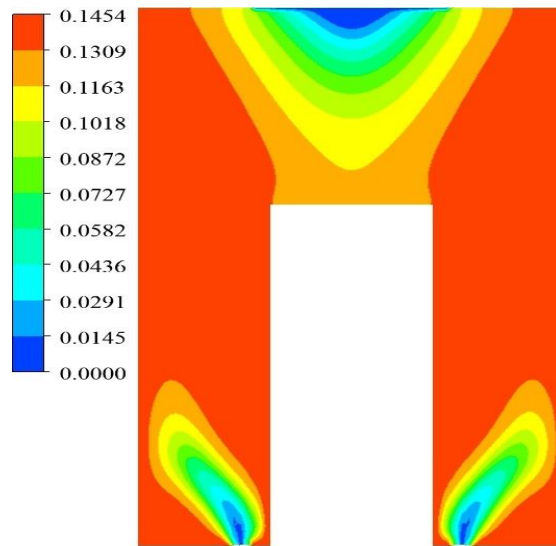


Fig. A-36 Contours of CO₂ mass fraction along the central plane for $\Phi = 0.8$, $L/L_0 = 1$ and $s = 1.13$.

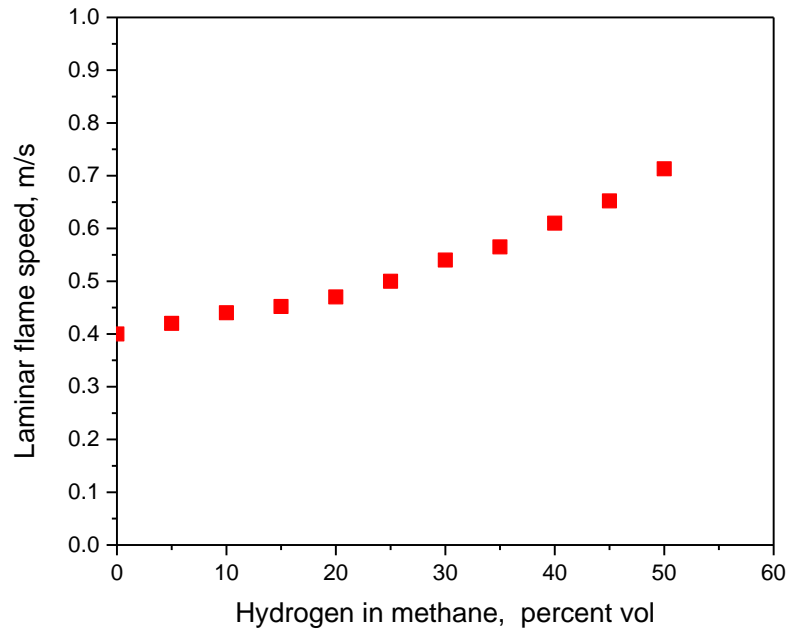


Fig. A-37 Laminar flame speed of methane/hydrogen mixtures
<https://hal.archives-ouvertes.fr/hal-00776646/document>

Мустафа Макхзоум Али Махјоуб **Биографски подаци**

Мустафа Макхзоум Али Махјоуб је рођен 28.08.1976 у Мисурати, Либија. Основно и средње образовање је стекао у Либији. 1992. године се уписује се на Универзитет у Триполију и студира машинство где 1999. стиче BSc диплому. Потом прелази 2004. године на Универзитет у Мисурати где 2009. године стиче MSc диплому машинског инжењера. Докторске студије на Машинском факултету у Београду уписује 2014. године и које успешно завршава са просечном оценом 9,89.

У периоду 2003 – 2009 Мустафа Макхзоум Али Махјоуб ради у Iron & Steel company Misurata у Либији као инжењер за одржавање постројења. 2009. године прелази на Универзитет у Мисурати где ради као доцент. У периоду од 2012-2013. године је шеф Одељења за високо образовање на Универзитету у Мисурати. За време рада на Универзитету у Мисурати Mustafa Makhzoum Ali Mahjoub објављује рад:

Mustafa Makhzoum Ali Mahjoub, Thermal Analysis of Combined cycle Power Plant with Desalination Unit, Scientific Net, Materials Science And Engineering, 2012.

Докторске студије на Машинском факултету Универзитета у Београду уписује школске 2013/2014. године где полаже све испите предвиђене Планом усавршавања.

Током докторских студија објављује рад:

Mustafa Makhzoum Ali Mahjoub, Aleksandar M. Milivojević, Vuk M. Adžić, Marija A. Živković, Vasko G. Fotev, Miroljub M. Adžić, Numerical Analysis of Lean Premixed Combustor Fueled by Propane-Hydrogen Mixture, Thermal Science, Year 2017, Vol. 21, No. 6A, pp. 2593-2602. Thermal Science је категорисан као међународни часопис M23.

Прилог 1.

Изјава о ауторству

Потписани **MUSTAFA MAKHZOUM MAHJOUR**

број индекса D43 / 2013

Изјављујем

да је докторска дисертација под насловом

THE EFFECT OF BLENDING HYDROGEN INTO NATURAL GAS ON COMBUSTION

UTICAJ UVOĐENJA VODONIKA U PRIRODNI GAS NA PROCES SAGOREVANJA

- резултат сопственог истраживачког рада,
- да предложена дисертација у целини ни у деловима није била предложена за добијање било које дипломе према студијским програмима других високошколских установа,
-
- да су резултати коректно наведени и
- да нисам кршио/ла ауторска права и користио интелектуалну својину других лица.

Потпис докторанда

У Београду, Април 2018

Прилог 2.

Изјава о истоветности штампане и електронске верзије докторског рада

Име и презиме аутора	MUSTAFA MAKHZOUM MANJOUR
Број индекса	D43 / 2013
Студијски програм	Машинско инжењерство
Наслов рада	УТИЦАЈ УВОЂЕЊА ВОДОНИКА У ПРИРОДНИ ГАС НА ПРОЦЕС САГОРЕВАЊА
Ментор	др. Мирољуб Ацић

Потписани/а MUSTAFA MAKHZOUM MANJOUR

Изјављујем да је штампана верзија мог докторског рада истоветна електронској верзији коју сам предао/ла за објављивање на порталу **Дигиталног репозиторијума Универзитета у Београду**.

Дозвољавам да се објаве моји лични подаци везани за добијање академског звања доктора наука, као што су име и презиме, година и место рођења и датум одбране рада.

Ови лични подаци могу се објавити на мрежним страницама дигиталне библиотеке, у електронском каталогу и у публикацијама Универзитета у Београду.

Потпис докторанда

У Београду, Април 2018

Прилог 3.

6 Изјава о коришћењу

Овлашћујем Универзитетску библиотеку „Светозар Марковић“ да у Дигитални репозиторијум Универзитета у Београду унесе моју докторску дисертацију под насловом:

THE EFFECT OF BLENDING HYDROGEN INTO NATURAL GAS ON COMBUSTION

UTICAJ UVOĐENJA VODONIKA U PRIRODNI GAS NA PROCES SAGOREVANJA

која је моје ауторско дело.

Дисертацију са свим прилозима предао/ла сам у електронском формату погодном за трајно архивирање.

Моју докторску дисертацију похрањену у Дигитални репозиторијум Универзитета у Београду могу да користе сви који поштују одредбе садржане у одабраном типу лиценце Креативне заједнице (Creative Commons) за коју сам се одлучио/ла.

1. Ауторство
2. Ауторство - некомерцијално
3. Ауторство – некомерцијално – без прераде
4. Ауторство – некомерцијално – делити под истим условима
5. Ауторство – без прераде
6. Ауторство – делити под истим условима

(Молимо да заокружите само једну од шест понуђених лиценци, кратак опис лиценци дат је на полеђини листа).

Потпис докторанда

У Београду, _____

1. Ауторство - Дозвољаваате умножавање, дистрибуцију и јавно саопштавање дела, и прераде, ако се наведе име аутора на начин одређен од стране аутора или даваоца лиценце, чак и у комерцијалне сврхе. Ово је најслободнија од свих лиценци.
2. Ауторство – некомерцијално. Дозвољаваате умножавање, дистрибуцију и јавно саопштавање дела, и прераде, ако се наведе име аутора на начин одређен од стране аутора или даваоца лиценце. Ова лиценца не дозвољава комерцијалну употребу дела.
3. Ауторство - некомерцијално – без прераде. Дозвољаваате умножавање, дистрибуцију и јавно саопштавање дела, без промена, преобликовања или употребе дела у свом делу, ако се наведе име аутора на начин одређен од стране аутора или даваоца лиценце. Ова лиценца не дозвољава комерцијалну употребу дела. У односу на све остале лиценце, овом лиценцом се ограничава највећи обим права коришћења дела.
4. Ауторство - некомерцијално – делити под истим условима. Дозвољаваате умножавање, дистрибуцију и јавно саопштавање дела, и прераде, ако се наведе име аутора на начин одређен од стране аутора или даваоца лиценце и ако се прерада дистрибуира под истом или сличном лиценцом. Ова лиценца не дозвољава комерцијалну употребу дела и прерада.
5. Ауторство – без прераде. Дозвољаваате умножавање, дистрибуцију и јавно саопштавање дела, без промена, преобликовања или употребе дела у свом делу, ако се наведе име аутора на начин одређен од стране аутора или даваоца лиценце. Ова лиценца дозвољава комерцијалну употребу дела.
6. Ауторство - делити под истим условима. Дозвољаваате умножавање, дистрибуцију и јавно саопштавање дела, и прераде, ако се наведе име аутора на начин одређен од стране аутора или даваоца лиценце и ако се прерада дистрибуира под истом или сличном лиценцом. Ова лиценца дозвољава комерцијалну употребу дела и прерада. Слична је софтверским лиценцама, односно лиценцама отвореног кода.